Dissertation zur Erlangung des Doktorgrades
der Fakultät für Chemie
der Ludwig-Maximilians-Universität München

Opto-electronic characterization of charge transport in hybrid perovskite thin film systems for photovoltaic applications

von
Irene Grill

aus
Reşiţa (Rumänien)

2018

Erklärung

Diese Dissertation wurde im Sinne von § 7 der Promotionsordnung vom 28. November 2011 von Herrn Prof. Dr. Achim Hartschuh betreut.

Eidesstattliche Versicherung

Diese Dissertation wurde eigenständig und ohne unerlaubte Hilfe erarbeitet.

München, 08. Februar 2018

.....
Irene Grill

Dissertation eingereicht am	09. Februar 2018
Erstgutachter:	Prof. Dr. Achim Hartschuh
Zweitgutachter:	Dr. Pablo Docampo
Mündliche Prüfung am	22. März 2018

Abstract

The steadily rising global energy demand has triggered a rapid evolution of thin film photovoltaics. Novel materials and device architectures have been developed during the last decades, whereas none of them captures a substantial fraction of the photovoltaic market due to poor charge transport or higher production costs as compared to silicon. Recently, organolead halide perovskite thin films have been demonstrated as highly suitable absorber and transport layers for photovoltaics showing excellent photo-physical properties combined with easy and cheap processing. Despite power conversion efficiencies surpassing 22%, hybrid perovskites are yet in a very early stage of development since many fundamental questions regarding the charge transport mechanism and limitations remain open. This thesis focuses on the experimental determination of the charge carrier mobility and lifetime, the key quantities of charge carrier transport, in the archetypical perovskite compound $CH_3NH_3PbI_3$ (MAPI) in correlation with film morphology, power conversion efficiency and other characteristics. The sample materials studied in this thesis were provided by the group of Dr. Docampo, optical and opto-electronic characterization was done within the group of Prof. Hartschuh. Typically, solution-processed perovskites can be fabricated via a plethora of different approaches. Two-step sequential deposition crystallization on the one hand is based on the addition of the organic cation to a pre-crystallized lead halide film while one-step fast crystallization exploits the direct growth of the perovskite in the presence of a solvent. The systematic variation of their parameters is known to influence morphology and chemical composition. MAPI films derived from the two-step approach are found to show modest charge carrier mobilities in lateral dimensions, lifetimes and power conversion efficiencies, but can be significantly improved by the addition of a chloride precursor, enhancing the crystallinity of the film without being incorporated into the structure. Furthermore, one-step fabrication results in larger diffusion constants as well as enhanced mobility values and performance characteristics when compared to two-step films which is assigned to additional radiative transport and a reduced number of grain boundaries, respectively. The obtained results indicate that morphology is one key parameter for efficient charge transport in these films, whereas this interpretation is supported by additional time-resolved photocurrent measurements on millimeter-sized crystals with the same chemical composition. Finally, the charge transport with the focus on charge carrier mobility in working devices is investigated. The widely used architecture for lab-scale devices comprising the perovskite absorber being sandwiched between a hole and an electron extraction layer is found to translate into mobility values that are 3-4 orders of magnitude smaller than in the single perovskite film. Additional experiments identify the transport layers as one major factor limiting the overall transport in the solar cell stack.

Contents

1 Motivation **1**

2 Theory and state of the art **5**

2.1 Characteristics of solar cells 5

2.1.1 Structure and operation mechanism of solar cells 5

2.1.2 Types of photovoltaic devices 11

2.2 Organic-inorganic perovskite materials as new promising candidates for PV systems 14

3 Experimental details **19**

3.1 Time-of-flight setup 19

3.2 Time-resolved photoluminescence setup 22

3.3 Fabrication of laterally arranged in-plane gold contacts 24

3.4 Solar cell fabrication 27

4 Controlling crystal growth by chloride-assisted synthesis: Towards optimized charge transport in hybrid halide perovskites **29**

4.1 Motivation 29

4.2 Materials and methods 30

4.3 Results and discussion 31

4.4 Conclusion 38

5 Two-step vs. one-step deposition: Tuning the opto-electronic properties in perovskite solar cells **39**

5.1 Motivation 39

5.2 Materials and methods 40

5.3 Results and discussion 41

5.4 Conclusion 46

6 The impact of grain size on charge carrier mobility in MAPI systems **49**

6.1 Motivation 49

6.2 Materials and methods 50

6.3 Results and discussion 50

6.4 Conclusion 54

7 Control of perovskite crystal growth by methylammonium lead chloride templating **55**
7.1 Motivation . . . 55
7.2 Materials and methods . . . 56
7.3 Results and discussion . . . 56
7.4 Conclusion . . . 61

8 Charge transport limitations in perovskite solar cells: The effect of charge extraction layers **63**
8.1 Motivation . . . 63
8.2 Materials and methods . . . 64
8.3 Results and discussion . . . 66
8.4 Conclusion . . . 74

9 Summary and Outlook **75**
9.1 Summary . . . 75
9.2 Outlook . . . 77

Bibliography **78**

List of Abbreviations **95**

List of Figures **97**

List of Tables **99**

List of peer-reviewed publications **101**

Conference contributions **103**

Acknowledgments **105**

1 Motivation

One of the major challenges of the 21st century that mankind has to face is the sustainable management of the increasing global energy demand. Ideally, the solution addressing this problem meets several aspects simultaneously, such as environmental friendliness (especially reduction of CO_2 emissions), abundance of the source, renewability, cost-efficiency and simpleness in design in terms of stand-alone systems.

In one year, the earth's surface receives approximately $2.5 \cdot 10^{24}$ J from the sun [1] while the annual human energy consumption is predicted to exceed $6.5 \cdot 10^{20}$ J by the year 2030 [2]. Solar energy hence seems to be potentially capable to contribute significantly to a new era of clean energy production beyond fossil fuels or nuclear technology since solar radiation can be converted to heat and electric energy using various technologies [3,4]. Consequently, solar harvesting materials and systems have to be optimized in a continuous manner and new absorber materials have to be designed in order to benefit at most from the energy provided by the sun. The underlying fundamental mechanism of solar cell devices that ensures proper operation characteristics is the photovoltaic effect which was first discovered by Bequerel [5] and theoretically explained as the photoelectric effect by the Nobel laureate Einstein [6].

Up to date, three generations of photovoltaic (PV) technologies have been developed. The first generation comprises cost-intense single-junction solar cells made of single- or multicrystalline silicon and is widely established. Second generation PV technology consists of thin film absorber layers such as amorphous silicon, CIGS or CdTe deposited on low-cost substrates [4, 7, 8] while the third generation solar cells are in an early stage representing alternative approaches and did not enter the PV market yet. However, third generation PV probably have the most promising potential for commercial and long-term success since they are made of cheap and abundant materials, e.g. organic and polymer cells or dye sensitized solar cells [3, 8, 9].

A new player of these emerging third generation technologies is the organolead halide perovskite-based solar cell that has recently entered the stage and seems to be a very appealing candidate for future incorporation in PV modules. Hybrid perovskite heterojunction structures are already approaching the efficiencies obtained by the widely established silicon or CIGS technology [10] and have experienced tremendous and to date unbowed scientific interest since the first demonstration of a working lab-scale solar cell device in 2009 [11]. Not only the unprecedented boost of observed efficiencies from 3.8% [11]

to currently surpassing 22% [12] revealed by a low-cost solution-processed material gains much attention by the PV community, but also the excellent and by all means outstanding photo-physical properties surprise. Hybrid perovskites feature a high absorption coefficient ($\alpha \sim 10^5 \mathrm{cm}^{-1}$) [13], band-gap tunability by compositional control [14] and long-ranged diffusive transport in the micrometer range [15] together with high charge carrier mobilities (1-100 $\mathrm{cm}^2/\mathrm{Vs}$) [16]. The combination of all these advantageous properties results in very efficient and cheap devices. The most probable way for perovskites to enter the PV market is via multijunction tandem devices consisting of a low band-gap material such as Si or CIGS as bottom cell and an organolead halide perovskite serving as top cell due to its band-gap around 1.6 eV [14] where the efficiency could potentially be pushed even farther.

Despite the well-suited properties of perovskites for PV applications, many questions regarding the photo-physics in this material remain open. Detailed knowledge, especially of charge transport and dynamics in the material itself but also in combination with adjacent layers and interfaces, however is crucial for further optimization of solar cell devices. To date, only little information on mechanisms and bottlenecks limiting charge transport, especially mobility, is available and an overall model properly describing charge transport is still lacking. Research groups from all over the world are currently addressing these topics, demonstrating that fundamental understanding of the photo-physical properties is an essential step towards fast commercialization of the material. Importantly, intrinsic effects have to be clearly distinguished from extrinsic ones. While intrinsic mechanisms result from carrier-lattice interactions, which are preexisting and cannot be eliminated, extrinsic effects are induced by the material itself in terms of grain boundaries, disorder of the energetic landscape and impurities. Consequently, these effects can and should be minimized by adapting the employed processing technique. Intrinsic effects on the other hand have to be investigated in detail to estimate what potentially can be achieved in the material. The results illustrated in this work are exclusively focusing on the control of extrinsic factors influencing charge transport and dynamics in both hybrid perovskites and derived solar cells and their correlation to solar cell performance.

The here presented thesis firstly introduces the reader to the theoretical (Chap. 2) and experimental (Chap. 3) background of the investigations performed herein and can be seen as a brief overview of the current state of knowledge.
The experimental work described in this thesis was done in close collaboration between the groups of Dr. Docampo (fabrication of the samples and SEM/XRD/PCE analysis) and Prof. Hartschuh (opto-electronic and optical investigation of the samples) and is essentially grouped into two major parts, each addressing certain scientific questions regarding the photo-physical properties of perovskite-based solar cells. The first experimental part is focusing on the impact of different synthesis protocols used for fabrication of the archetypical hybrid perovskite compound $CH_3NH_3PbI_3$ (methylammonium lead triiodide,

MAPI) on charge transport in lateral dimensions, probed by time-of-flight photocurrent and photoluminescence measurements.

Chap. 4 reports on the investigation of two MAPI films both deposited by a two-step sequential deposition protocol and only differing in the optional addition of a chloride containing salt to the precursor solution. Although being virtually identical from a chemical and structural point of view (confirmed by XRD and SEM measurements), these films show substantial differences in their optoelectronic characteristics in terms of charge carrier mobility, photoluminescence lifetimes and solar cell performance. In-situ photoluminescence lifetime measurements during the crystallization of the thin films unveil that the chloride addition during film deposition results in slower crystal growth, leading to fewer defects and higher crystalline order which directly reflects improved optoelectronic properties.

Aside from sequential deposition, a one-step crystallization technique has emerged for hybrid perovskites. A direct comparison of one-step versus two-step deposition is described in Chap. 5 resulting in a higher charge diffusion constant, mobility and solar cell performance in case of the one-step fast-crystallization deposition procedure. The improved optoelectronic performance in these films is most likely due to the film morphology containing larger crystallites and thus fewer grain boundaries as compared to films derived from the two-step protocol.

Chap. 6 investigates the effect of substantial enlargement of crystallites in MAPI thin films, induced by adapting of the fabrication technique. Film quality in terms of morphology and crystallinity are crucial parameters determining efficient charge transport. Additional comparison of the mobility values in these films with photocurrent measurements on perovskite crystals in millimeter dimensions provides results in differences of up to two orders of magnitude and potentially provides an upper mobility limit range in the material that can be reached when extrinsic effects affecting charge transport are minimized.

The second part of this thesis on the other hand studies the altered charge transport in vertically stacked perovskite-based solar cells. In the respective photovoltaic devices, charge carriers are less prone to grain boundaries due to film thicknesses of around 300 nm, but can easily be scattered at the interfaces of adjacent layers sandwiching the photoabsorber.

Chap. 7 analyzes the influence of temperature-controlled and chloride-based precursor-derived perovskite film morphology on photovoltaic performance and charge carrier mobility in the respective devices. In-situ X-ray diffraction is used to monitor the crystallization of the film under different temperature conditions starting from a template compound. In this manner, films of different quality in terms of grain size and the presence of pinholes can be achieved. Incorporation of these films in respective n-i-p solar cell devices results in

both improved photovoltaic performance and charge carrier mobilities in vertical direction for large crystal films due to a reduced number of pinholes when maintaining the device architecture and thickness.

In Chap. 8 the influence of the charge extraction layers on charge carrier mobility is studied. Because mobilities obtained for devices in Chap. 7 are three orders of magnitude smaller than expected for materials like hybrid perovskites with excellent optoelectronic properties, the effect of charge extraction layer thickness variation is investigated via time-of-flight experiments. From these experiments it becomes clear that mainly the hole transport layer (and to a lesser extent the electron transport layer) and the associated interfaces rather than the perovskite material itself can be identified as the major limiting factors of the charge carrier transport time in working devices.

2 Theory and state of the art

The following chapter introduces the fundamental concept of solar cells and its ongoing improvement towards low-cost and high-efficiency devices. It provides a summary of the required basic principles for the understanding of the experiments performed within this work in terms of physical processes as well as developments in solar cell design during the last decades.

2.1 Characteristics of solar cells

2.1.1 Structure and operation mechanism of solar cells

The discovery of the photovoltaic effect by Becquerel in 1839 [5] was the first milestone in the history of photovoltaics. With the theoretical model on a quantum basis, described as the photoelectric effect and provided in 1905 by Einstein [6], the way was finally paved towards modern photovoltaic technologies. In 1954, Chapin and co-workers [17] from the Bell Labs presented the first high-power p-n junction silicon solar cell (homojunction). The concept of the p-n junction is nowadays very well understood and the most commonly used basic principle for the design of new photovoltaic systems.
The p-n junction represents the interface between a p-doped (p-type) and an n-doped (n-type) semiconductor. When bringing these semiconductors together, the electrons from the area with a high electron concentration (n-doped side) will diffuse to the area with low electron concentration (p-doped side), pushed by the different chemical potentials and leaving behind fixed and positively charged ions. The holes on the other hand diffuse in the opposite direction creating a diffusion current as well and leaving behind negatively charged ions. Hence, a positive charge is built up in the n-type semiconductor and a negative charge in the p-type region (see Fig. 2.1). These processes are maintained until equilibrium is reached, i.e. until the diffusion process is counterbalanced by the generated electric field of the depletion or space charge region. The barrier layer does no longer feature mobile charge carriers whereas a diffusion voltage V_D is created, leading to a potential difference [18, 19].
With the presence of the depletion region and the addition of metallic contacts, the p-n junction results in a diode that can be run efficiently when applying an external voltage in forward direction, i.e. connecting the negative terminal to the n-side and the positive one to the p-side. Consequently, the net electric field in the depletion region is reduced because of the opposite direction of the applied external voltage. This leads to a reduction of the height of the potential barrier ("built-in potential") which facilitates the motion of a significant number of majority carriers across the junction and generating a forward

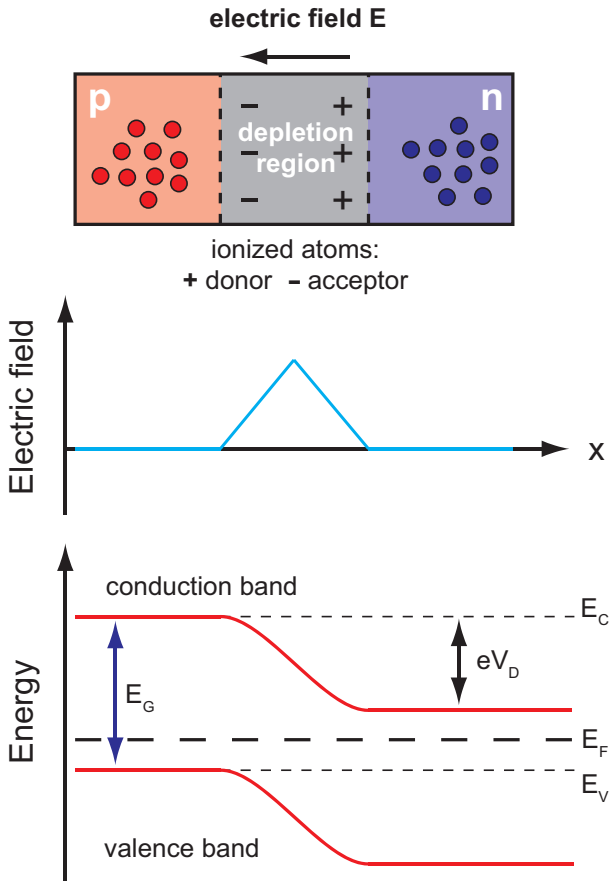

Fig. 2.1 Illustration of processes at a p-n junction without an external voltage source. Electrons diffuse from the n-doped side to the p-doped side while leaving behind positively charged donor atoms and vice versa for holes from the p-doped side. The space charges generate an electric field in the depletion region while a diffusion voltage $V_D = \int_{x_p}^{x_n} E(x)\,\mathrm{d}x$ is created due to the space charge region. Consequently, the energy bands in the p-zone are increased by eV_D (potential barrier). E_C is the minimum of the conduction band, E_V represents the maximum of the valence band, E_F labels the Fermi level and E_G is the band gap energy between E_V and E_C. Adapted from [19].

current flow also known as diode current. More precisely, electrons from the n-side and holes from the p-side penetrate the depletion region which allows for a substantial current flow that is conducted by the diode. Applying a reverse bias on the other hand leads to an increase of the potential barrier since more electrons from the n-side and holes from the p-side are extracted at the metallic contacts, thus extending the space charge region. As a consequence, the potential barrier increases and only a very small current flow, induced by thermally generated minority carriers (holes from the n-side and electrons from the p-side) that are able to penetrate the barrier, can be observed [19, 20]. Hence, the diode acts as a barrier. With respect to solar cells, this leads to an efficient separation of charges [18]. The expression describing theses processes in a diode, i.e. the evolution of the generated current I_D on the external voltage V in the dark in forward direction, is approximated by:

$$I_D = I_S(\mathrm{e}^{eV/nkT} - 1) \tag{2.1}$$

where I_S is the saturation current (idealized inverse current), e the elementary charge, n is the ideality factor (measures of the type of recombination in the cell), k is Boltzmann's constant and T the temperature. For the reverse direction, Eqn. 2.1 does not consider breakdown of the diode at very high voltages, additionally the inverse current does not saturate at small current values as described by the equation.

A typical mono- or polycrystalline silicon solar cell is nothing other than a large-sized diode exposed to solar irradiation. Photons with energies larger than the band gap energy E_G are absorbed within the crystal (ideally within or close to the junction) and generate charge carriers in terms of electron-hole pairs due to the photoelectric effect. Because of the low exciton binding energy of approximately 15 meV in silicon [21], charge carriers are easily separated and diffuse through the material. When reaching the space charge region, they are swept across the junction. The minority carriers (electrons) in the p-region move opposite to the field direction across the junction and accumulate in the n-type semiconductor where they are seen to be majority carriers. Similarly, holes generated in the n-region move in field direction towards the p-type semiconductor.

At some point, charge generation and recombination will reach equilibrium, i.e. the current flow is suppressed and the solar cell reaches the open-circuit voltage (V_{OC}). In terms of an energy band picture, eV_{OC} represents the separation between the quasi-Fermi energies of the p and the n-side. On the other hand, when shorting the illuminated cell through a conductive connection without applying an external bias, carriers that have been created are instantaneously extracted so that the space charge region as well as the electric field remain unchanged. In this case, the maximum current of the cell can be measured and is defined as the short-circuit current I_{SC}, being proportional to the intensity of the radiation hitting the cell on a defined area and thus being proportional to the number of generated electron-hole pairs [19].

Because a solar cell is basically a diode, it can easily be described by an equivalent circuit. Fig. 2.2 a depicts the circuit of an source generating ideal current I_{PH} combined with a diode (I_D). Under illumination, this interplay is described by the superposition of the diode current and the photogenerated current:

$$I(V) = I_D - I_{PH} = I_S(\mathrm{e}^{eV/nkT} - 1) - I_{PH} \tag{2.2}$$

which determines the current-voltage characteristic (I vs. V) to be shifted to the fourth quadrant of the Cartesian plane, but is typically mirrored to the first quadrant (-I vs. V). From Eqn. 2.2 the open-circuit voltage can easily be derived for $I = 0$, assuming $I_{PH} \gg I_S$ [19, 20]:

$$V_{OC} = \frac{nkT}{e} \cdot \ln\left(\frac{I_{PH}}{I_S} + 1\right) \approx \frac{nkT}{e} \cdot \ln\left(\frac{I_{PH}}{I_S}\right). \tag{2.3}$$

Under real operating conditions resistive effects that reduce the efficiency have to be considered, usually in terms of series and/or shunt resistance (R_{SH} and R_S, see Fig. 2.2 b) that result from contact resistance between contact and absorber, resistance of top and

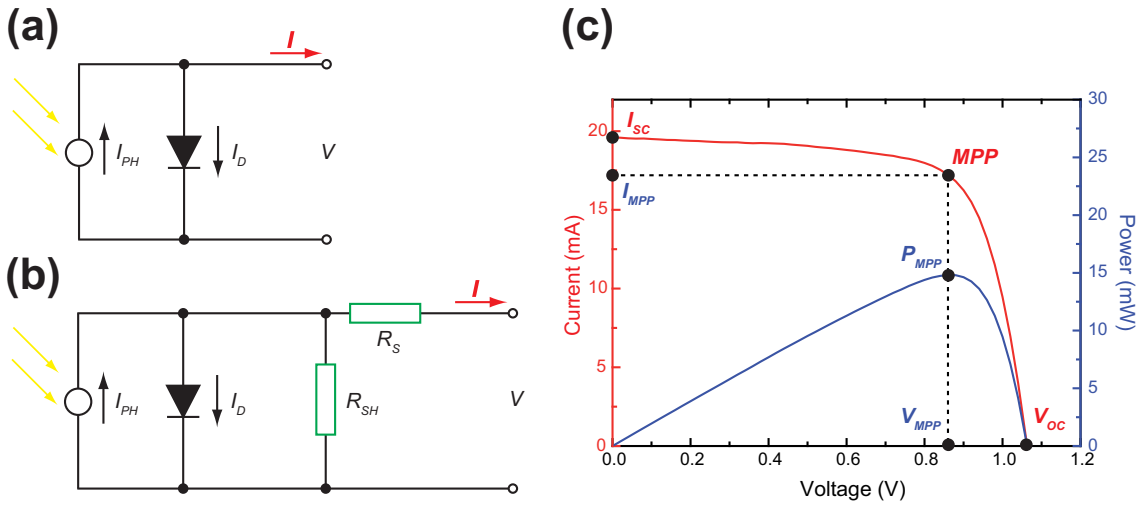

Fig. 2.2 Circuit of (a) an ideal solar cell and (b) a solar cell with parasitic shunt R_{SH} and series R_S resistances. In both cases, I_{PH} is the photocurrent when the diode is exposed to light and I_D is the current generated by the diode in the dark following Eqn. 2.1. (c) Current-voltage curve of a thin-film solar cell (red curve) and the respective calculated power profile (green curve). The curve has been mirrored to the first quadrant.

rear contacts or manufacturing defects. Eqn. 2.2 is then translated via iteration [19,22] to the generalized Shockley equation:

$$I(V) = I_S(\mathrm{e}^{e(V-I(V)R_S)/nkT} - 1) - I_{PH} - \frac{V - I(V)R_S}{R_{SH}}. \tag{2.4}$$

The measurement of current-voltage curves does not only allow to estimate open-circuit voltage and short-circuit current of the solar cell of interest at a certain level of irradiance and temperature, but also provides valuable information on the generated power when operated in the fourth quadrant (while consuming power when operated in the first and third quadrant) and the respective power conversion efficiency (Fig. 2.2 c).

Power is defined by the product of voltage and current, while the maximum power produced by the solar cell is at the maximum power point P_{MPP}. This point is necessary for the calculation of the fill factor being one of the key values of photovoltaic systems and measures the squareness of the I-V profile [20,22]. The fill factor is given by:

$$FF = \frac{P_{MPP}}{V_{OC} \cdot I_{SC}} = \frac{V_{MPP} \cdot I_{MPP}}{V_{OC} \cdot I_{SC}}. \tag{2.5}$$

An ideal solar cell would display a fill factor of unity, i.e. a constant current valuing the short-circuit current over the entire external voltage range and sharply dropping to zero at open-circuit voltage conditions. Real solar cells however show values below unity due to current losses within the device (e.g. due to parasitic resistance) since the power at the maximum power point is always smaller than the product of V_{OC} and I_{SC}, already indicated by the typical curved shape of solar cell I-V characteristics [20]. The value of the fill factor directly affects the power conversion efficiency (PCE) of a solar cell [18] as seen in Eqn. 2.6:

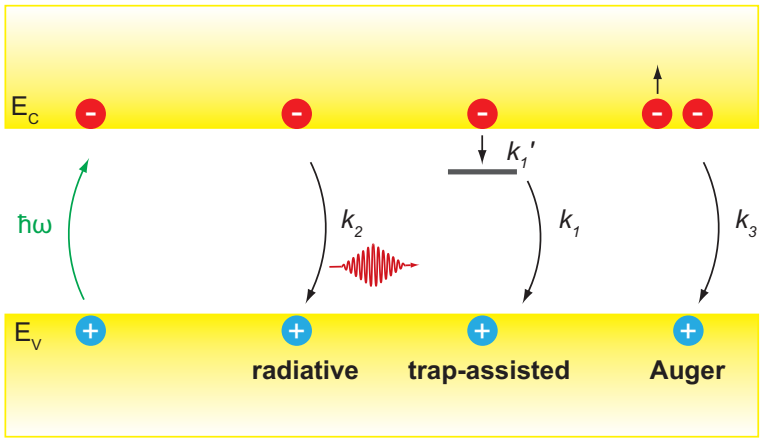

Fig. 2.3 Recombination mechanisms of photoinduced charge carriers. Upon absorption of photons, charges are generated and can recombine following three different processes. Radiative band-to-band recombination occurs with the rate constant k_2, whereas the non-radiative processes are either trap-assisted with the rate constants k_1 (detrapping) and k_1' (trapping) or of Auger type with the rate constant k_3. Based on [24].

$$PCE = \eta = \frac{P_{MPP}}{P_0} = \frac{V_{OC} \cdot I_{SC} \cdot FF}{P_0}. \tag{2.6}$$

To run a solar cell properly and as efficiently as possible, three fundamental processes are required to convert solar radiation into electrical power. First, photons with $E_{photon} \geq E_G$ have to be absorbed via the photoactive material to create charge carriers. Next, the charges have to be separated and finally, the mobile charges have to be collected and extracted at the corresponding selective electrodes [23]. The efficiency of operating solar cells is determined by limitations in all three steps. Because of the quantum mechanical photon energy requirement, not all photons are absorbed and not every photon immediately creates electron-hole pairs (conversion to heat). Furthermore, not all of the generated electron-hole pairs are separated and contribute to the current but recombination processes can occur, in the bulk as well as at the surface or at the contacts [20]. Recombination occurs due to an enhanced carrier concentration induced by photogeneration and exceeding the thermodynamic equilibrium between carrier generation, recombination and transport. The recombination rate equation can be written as:

$$\frac{\mathrm{d}n(t)}{\mathrm{d}t} = -k_1 n - k_2 n^2 - k_3 n^3 \tag{2.7}$$

where k is a rate constant associated to a certain recombination mechanism and n the carrier density, whereas the decay of the charge carrier density takes into account the initial carrier density n_0 and the carrier lifetime τ.

Effectively, charge transport in solar cells is determined by carrier lifetime and diffusion. The most important recombination mechanisms are the Shockley-Read-Hall and the Auger process, both being non-radiative, and the radiative process, which are covered by Eqn. 2.7 and depicted in Fig. 2.3.

Radiative recombination is a bimolecular ($\propto n^2$) band-to-band process reflecting electron-hole recombination causing emission of a photon. Shockley-Read-Hall recombination on the other hand is a trap-assisted monomolecular ($\propto n^1$) process that depends on one type of carrier that is being trapped in a state below the conduction band, introduced for example by charged dopants. Hence, trap-asssited recombination usually largely depends on the processing of the material of interest. Ultimately, Auger recombination, a three particle process ($\propto n^3$), is based on recombination of an electron with a hole while transferring energy to another carrier which can result in phonon absorption or emission. Additionally to carrier lifetime τ, carrier diffusion length L_D and mobility μ (drift of charges) are substantial as well and can directly affect solar cell performance [24, 25]. Due to collision processes in terms of scattering mechanisms, the motion of charge carriers is impeded leading to a reduced drift velocity and hence charge carrier mobility μ. Neutral impurity scattering is induced by crystallographic defects or impurities (substitutional or interstitial atoms) which introduce energy levels in the band-gap of the semiconductor. Ionized impurity scattering on the other hand is due to trajectory deviation of an electron approaching an ionized atom ($\mu \propto T^{3/2}$). Lattice scattering finally is due to vibrations of the lattice, either acoustical or optical phonons. The former interacting with electrons leads to changes in the distance between the lattice atoms from crystal site to site (coherent movement of lattice atoms) which produces a potential discontinuity (acoustic deformation potential scattering, $\mu \propto T^{-3/2}$), whereas the latter describes the interaction between electrons and the electric fields generated by polarization of the ionic lattice (out-of-phase movement of lattice atoms) [26]. Usually, more than one scattering mechanism is present. Assuming the simplified case that the mechanisms are independent, the Matthiessen rule can be applied to approximate μ:

$$\frac{1}{\mu} = \sum_i \frac{1}{\mu_i} \tag{2.8}$$

with μ_i being the mobility corresponding to a certain scattering mechanism. The most common mechanisms in solar cell materials are ionized impurity scattering and phonon scattering, explaining the commonly observed temperature dependence of mobility [27].
The fundamental optoelectronic parameters τ, L_D and μ describing charge transport in solar cell materials are connected via the diffusion constant D in the Einstein relation [28]:

$$D = {L_D}^2 \cdot R(n) = \frac{{L_D}^2}{\tau} = \frac{k_B T}{q} \cdot \mu. \tag{2.9}$$

Note that $R(n)$ is a measure for the total recombination rate and is obtained from the rate equation in Eqn. 2.7 multiplied by -1/n and q is the electrical charge. The Einstein relation assumes ambipolar transport (similar electron and hole mobilities), charge density populations at equilibrium, no rapid variation of composition or doping and small fields that do not disturb the thermodynamic equilibrium [29, 30]. Consequently, careful assessment is necessary to ensure that Eqn. 2.9 can be applied to a semiconducting material.
Besides recombination and scattering losses, Ohmic losses (R_S and R_{SH}) can occur as well

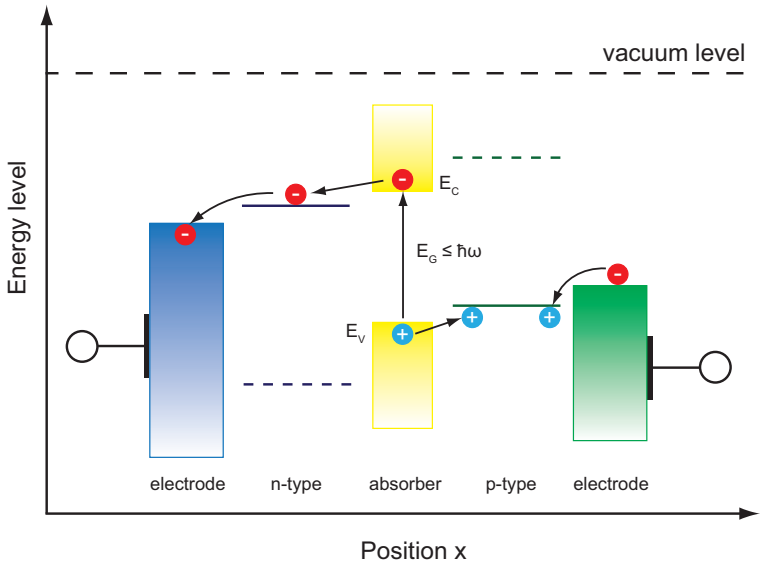

Fig. 2.4 Schematic energy diagram of a heterojunction solar cell. The absorber material is sandwiched between two electrodes with different work functions. Electrons in the conduction band will move to the contact with lower work function and are extracted. Holes from the valence band on the other hand move to the contact with higher work function where they recombine with an electron. Based on [14].

as optical losses in terms of reflection losses or shading of the front contact [20]. Shockley and Queisser [31] developed a model taking into account a large number of theoretical electrical energy losses in a single p-n junction solar cell and determining the upper efficiency limit as a function of band gap energy. At a temperature of 298 K and an irradiance of AM 1.5 (solar irradiance arriving on the earth's surface at mid-latitudes), the efficiency limit for silicon solar cells with a band gap energy of 1.1 eV is 32%, for GaAs (E_G = 1.4 eV) 33% and for the latest newcomer in the PV community, organolead halide perovskites, the limit is around 31% [32].

So far, the working principle of solar cells, which are based on the p-n junction, has been described using the example of crystalline silicon solar cells. However, the p-n junction alone is not only used in silicon solar cells. Modern solar cell design has to consider both efficiency and economical aspects and comprises a hetero-structure [18] where the absorber material is sandwiched between two different electrodes with different work functions ensuring efficient charge separation. In this architecture, electrons will move to the contact with lower work function and holes to the one with higher work function [23], as depicted in Fig. 2.4. To further push the efficiency limits, several approaches have been developed. The different types of solar cells are described in the following section.

2.1.2 Types of photovoltaic devices

The most common type of solar cells is crystalline silicon (c-Si) which is assigned to the first generation of solar cells. The architecture of c-Si cells has been improved and refined

substantially in the last decades so that to date it represents the working horse of all photovoltaic devices. The typical p-n junction basic structure is shown in Fig. 2.5 (top left), whereas the cell comprises the positive back contact, the thick p-type silicon layer, followed by the thin n-type layer which is covered by metallic fingers acting as the negative terminal of the device. Because of the higher surface quality of n-Si, the latter is chosen to be the front layer that is made very thin to ensure that a sufficient amount of light is absorbed to generate charge carriers within a diffusion length (typically 200 µm) away from the p-n junction. Consequently, the total thickness of typical silicon-based solar cells ranges between 150 and 300 µm [19]. Further improvement by the introduction of a thin anti-reflective coating (between contact fingers and n-layer), back surface fields (more heavily doped coating between p-layer and back contact) or texturisation of the top surface, to name just a few, gradually increased the efficiency of silicon solar cells. Fabrication of the wafers used in these solar cells is usually realized by the Czochralski method where the monocrystal is slowly pulled out of molten polycrystalline silicon upon the formation of a crystal nucleus. This process is very slow, expensive and consumes lots of energy which made industry focus more on polycrystalline (pc) solar cells whose working principle is identical with the one of c-Si. Polycrystalline silicon is made of pure silicon that has been molten and then casted in blocks, resulting in a multi-grain structure with crystals of different sizes and orientations. To reduce charge carrier recombination at the grain boundaries, the crystals are millimeter-sized in lateral dimension and match the wafer thickness in vertical direction. The majority of nowadays installed silicon photovoltaic modules is based on pc-Si [20].

To further reduce the manufacturing costs of solar cells, the concept of thin film solar cells on low-cost substrates such as glass or plastic has been introduced, requiring less material and less energy. To this end, materials are needed that can be fabricated as thin films while maintaining their functionality as photoabsorber, such as amorphous silicon (a-Si), GaAs, CdTe or Cu(In,Ga)Se_2 (CIGS), evaporated at low temperatures. Due to their small overall thickness of a few micrometers, thin film solar cells may also be fabricated as flexible devices when using a suitable substrate. One major drawback of thin film technology is the challenge introduced by the need of stable efficiency, which is mandatory to become competitive with crystalline silicon technology.

One very prominent example is amorphous silicon (a-Si). Thin film a-Si consists of randomly distributed Si atoms, resulting in different atom distances and angles. As a consequence, a large number of defects is present, introducing trap states and additional energy levels within the rather forbidden band gap and finally increasing the probability of charge recombination. This problem has been minimized by saturating a portion of dangling bonds with hydrogen. The same concept is being used to dope the amorphous silicon, making it either p- or n-type. Sandwiching the slightly n-doped intrinsic layer between an n-type and a p-type layer greatly reduces the second problem of a-Si, namely the poor charge carrier mobility, and resulting in a p-i-n structure. The intrinsic layer increases the size of the depletion region and consequently the respective electric field

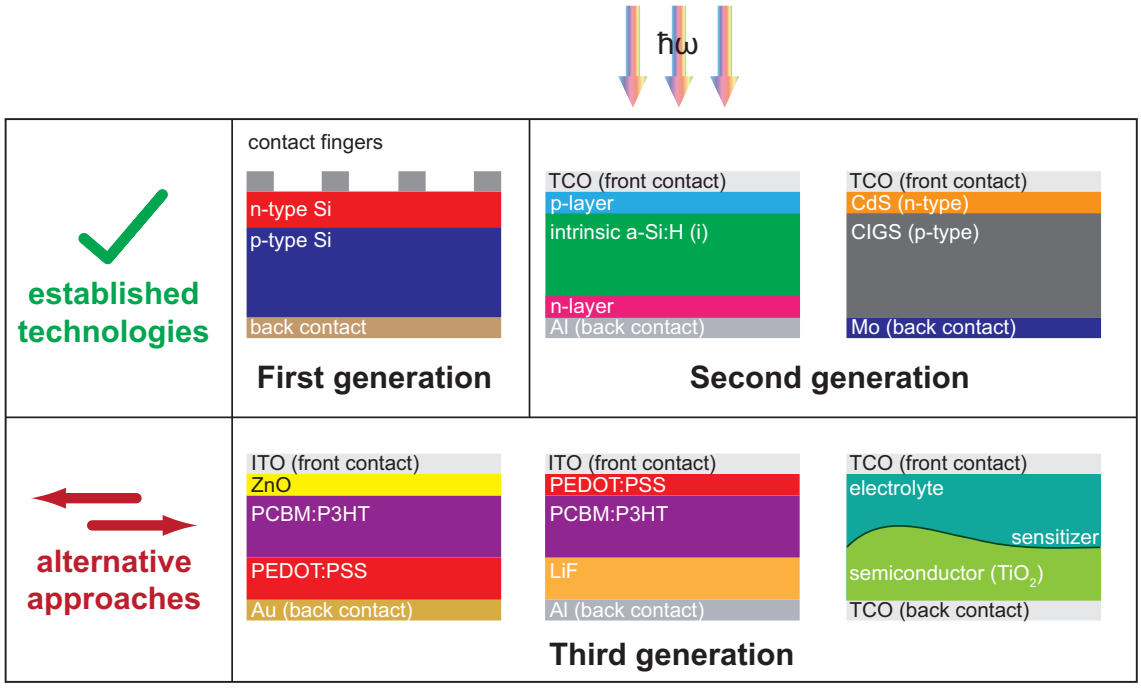

Fig. 2.5 Illustration of different cross-sectional device architectures from three solar cell generations. Crystalline silicon solar cells are part of the first generation (top left), while second generation comprises amongst others CIGS-based devices (top right). Third generation solar cells are also described as new emerging technologies and include architectures based on organic molecules and polymers (bottom left and center) or organic dyes as sensitizer (bottom right). Figure adapted from [20]

needed to sweep charge carriers across the junction. The maximum of the electric field is at the interface between the p-layer and the intrinsic layer, equivalent to a design that incorporates a thin p-layer to create charges near the top of the cell. A large disadvantage of a-Si solar cells is the breakup of Si-Si bonds upon illumination which introduces further recombination sites and lowers power conversion efficiency.

Another well-known example are CIGS absorber layers which are based on $CuInSe_2$ where up to 20% of In are replaced by Ga, leading to a band gap energy of 1.1 eV which is similiar to the one of crystalline silicon. Usually, a wide-band gap CIGS solar cell (shown in Fig. 2.5, top right) comprises a Mo layer, deposited onto the substrate via sputtering and serving as positive contact terminal, the co-evaporated photoactive CIGS layer, followed by a very thin CdS film and finally the aluminum-doped tinoxide top contact layer. Disadvantages of these solar cells are seen in the fabrication under vacuum conditions, the use of the expensive indium and the toxicity of the employed CdS film, whereas the latter has experienced a lot of efforts in terms of reduction or even elimination [19].

While second generation solar cells have already entered the PV market and are considered as established technologies, third generation photovoltaics represent alternative approaches and are yet to come. These emerging technologies pursue the concept of solar cells on cheap substrates and additionally employ cheap and abundant precursor materials for the fabrication of the layered thin film device structure, as shown in Fig. 2.5. One of

the best known examples is the dye-sensitized solar cell, sometimes referred to as photo-electrochemical solar cell and based on the absorption of photons in the dye layer acting as the sensitizer. An electron from these molecules is then transferred to the conduction band of titanium oxide. To avoid recombination, an electron from the liquid electrolyte (I_3^-/I^-) is transferred to the oxidized dye molecule, leading to a neutral state. The electrolyte on the other hand is set back to the original state by electron injection from the external load [19,33]. Because the presence of a liquid in the device raised serious concerns on possible leakage, the architecture of dye-sensitized cells has been improved by replacing the liquid electrolyte by a solid hole conductor, such as spiro-OMeTAD without modifying the basic concept and turning the solar cells into all-solid-state devices [34].
Despite the fact that third generation PV is a very promising technology with reasonable efficiencies on a lab scale, its long-term stability and practicability have to be demonstrated yet.

2.2 Organic-inorganic perovskite materials as new promising candidates for PV systems

In 2009, the suitability of organometal halide perovskites as absorber material has been demonstrated [11] and a new extremely promising representative of third generation PV has entered the scientific stage. Within less than a decade of research and development efforts, the efficiency of perovskite-based solar cells has been massively increased from 3.8% [11] to currently surpassing 22% [12] in lab scale devices. Hybrid perovskite materials are already awarded the fastest advancing solar technology the PV community has ever experienced and are seen as one of the biggest breakthroughs in science [35].
Perovskites are described by the formula ABX_3 and own a particular crystal structure as shown in Fig. 2.6 a and b. The large cation A occupies cuboctahedral sites, being surrounded by twelve X anions whereas the small cation B represents the center of octahedra formed by six X anions. All possible combinations resulting in the ABX_3 structure are limited by the tolerance factor:

$$t = \frac{R_A + R_X}{\sqrt{2}(R_B + R_X)} \tag{2.10}$$

with R_A, R_B and R_X are the radii of the ions incorporated in the perovskite structure. The value of the tolerance factor determines whether a certain ion can actually meet with the lattice structure and whether the material crystallizes in a cubic, tetragonal or orthorhombic structure. Transitions between these structures due to heating or cooling are well-known and very typical for the halide perovskites introduced below.
The most common perovskites are inorganic oxides which have been studied in detail because of their interesting ferroelectric [36] or superconductive properties [37] whereas hybrid halide perovskites were mainly disregarded until Mitzi and co-workers published their experimental results on conductivity in layered perovskites, already highlighting the

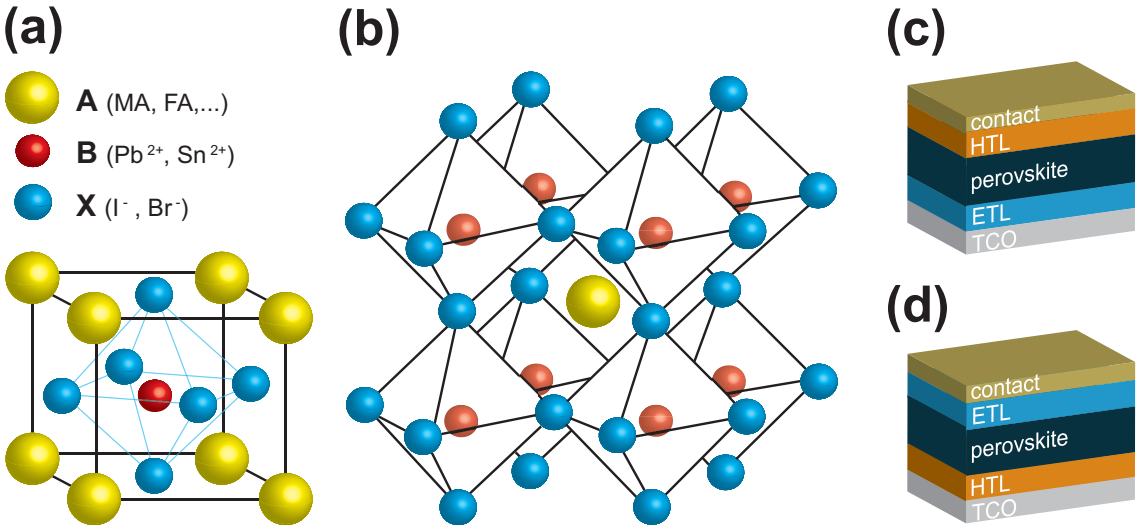

Fig. 2.6 Perovskite crystal structure and perovskite-based solar cell architectures. (a) Perovskite unit cell with cations A (methylammonium, formamidinium, Cs or Rb cations) occupying the lattice corners and metal cations B (lead or tin ions) occupying the octahedral voids formed by anions X (halide). (b) Alternative view of the perovskite lattice where B and X form BX_6 corner-sharing octahedra while A occupies the cuboctahedral voids (coordinated by twelve X anions). (c) Standard architecture of a planar perovskite-based solar cell where illumination occurs from the TCO (transparent conducting oxide) electrode (n-i-p structure). Typical materials used in this configuration are Au or Al (back contact), spiro-OMeTAD (HTM), TiO_x or SnO_x (ETL) and FTO or ITO (TCO). (d) Inverted architecture of a planar solar cell (p-i-n structure). Commonly employed materials are Ag or Al (back contact), PCBM or ZnO (ETL), PEDOT:PSS (HTM) and FTO or ITO (TCO).

properties of this material class as technologically interesting [38]. Expanding the structure to the third dimension, the resulting hybrid perovskite with the formula $CH_3NH_3PbX_3$ (X = Br or I) has been used for the first time in a solid-state sensitized solar cell-type [11]. Moving away from the dye-sensitized design to a mesoporous scaffold all-solid-state architecture [39, 40] and finally to a planar all-thin film stacking sequence [41] paved the way to the race on best efficiency values.

Numerous physical and economical properties render organolead halide perovskites very promising and competitive photovoltaic materials. High quality perovskite thin films can easily be fabricated from cheap and abundant precursor materials. Besides dual-source vapor deposition [41], solution processing at low temperatures is possible as well and very common in either a one-step (fast-crystallization deposition or anti-solvent method) [42,43] or a two-step fabrication technique (sequential deposition, either vapor or solution-assisted) [40, 44]. The effect of the two different solution-based techniques on the charge transport properties and the respective solar cells are studied in this work as well and the results can be found in Chap. 5.

Compositional and solvent engineering lead to a large variety of additional parameters that can be controlled during fabrication of the perovskite material and result in tunability of both microscopic and macroscopic physical properties of the film. Compositional variab-

ility of the anion enables the adaptability of the absorption range and band gap energy between 1.6 and 2.2 eV, hence a mixed perovskite with both iodide and bromide ions seems to be appropriate for application as top cell in tandem devices [14]. Adding a chloride salt to the perovskite during fabrication on the other hand does not lead to a shift of the band gap energy but improves the film quality [39, 44–46] together with the associated charge transport properties and is investigated in detail in Chap. 4 and Chap. 7. Besides anion exchange, partial replacement of the methylammonium cation by the larger sized formamidinium ($CH(NH_2)_2^+$) allows for an optimization of the band gap energy as well [47] while further addition of Cs^+ and Rb^+ in a quadruple configuration leads to enhanced reproducibility and a further boost of the power conversion efficiency [48, 49]. Certainly, the metal cation could similarly be substituted by Sn, however, these compounds show poor performance and only little stability [50].

Solvent engineering is, besides temperature conditions, another tool to effectively control film growth and quality (in terms of homogeneous morphology), both of fundamental importance since a reduced number of traps from pinholes, defects and grain boundaries is desired to ensure efficient charge transport. The goal is to stabilize the intermediate compound formed by the lead precursor salt (Lewis acid) and solvent molecules (Lewis base), such as DMSO, thiophene or pyridine [51, 52] which slows down the film formation and results in improved charge transport as well as enhanced power conversion efficiencies.

Generally, hybrid perovskites show continuous absorption over a broad range of visible light with a sharp edge and a steep onset and additionally an absorption coefficient of around 10^5 cm^{-1}, indicating that the number of optically detectable deep traps must be very small [13]. This property is highly advantageous since photon management in thin films is crucial and essentially means that a perovskite film thickness of approximately 500 nm is sufficient to absorb most of the incident photons with energies larger than the band gap energy. Furthermore, diffusion lengths L_D have been shown to be in the range of micrometers [15, 16, 53] which also indicates that the trap density is low and the nature of these defect states is shallow [54]. Monomolecular charge recombination is most likely assigned to processes related to ionized impurities [55, 56]. The presence of high diffusion lengths is beneficial for the fabrication of planar solar cell devices since L_D is much larger than the film thickness and the absorption depth in the absorber layer. Another outstanding physical property of perovskites is their charge carrier mobility which is, considering the fact that the material can be derived from solution processing, remarkably high and ranges between 1 and several tens of cm^2/Vs, depending on the fabrication protocol and the measurement technique used for the determination of μ [16, 57–62].

Incorporation of perovskite films in heterojunction devices is facile due to a large diversity of possible material combinations, all of them benefiting from the outstanding properties of the absorber layer and leading to good device performance. First investigations on perovskite solar cells were performed on mesoscopic structures where the perovskite acts as a sensitizer and is infiltrated in a scaffold such as TiO_2 [11] or Al_2O_3 [39]. The solar cells can also be fabricated without a mesoporous layer and are then referred to as planar

devices which are divided into n-i-p (standard, see Fig. 2.6 c) and p-i-n (inverted, see Fig. 2.6 d) architectures with respect to the layer that faces the incoming sunlight. A typical perovskite solar cell comprises a transparent conducting oxide, such as fluorine-doped tin oxide (FTO) or indium tin oxide (ITO) as substrate. In the n-i-p structure, the stacking sequence continues with TiO_x or SnO_x as the electron transport material, followed by the perovskite layer, the hole transport material (in most cases spiro-OMeTAD) and finally the back contact electrode which is usually gold or aluminum. Decent performance characteristics have also been demonstrated for HTL-free devices. For the p-i-n structure, the layer sequence is inverse, i.e. the hole transport material (typically PEDOT:PSS) is the first layer deposited on top of the front electrode. Next follows the absorber layer, top-coated with the electron transport material. Representative electron transport materials for this architecture are PCBM or ZnO on which the metallic contact (Ag or Al) is deposited. These stacking sequences ensure a well matched energy alignment between the conduction band of the absorber and the n-selective layer and accordingly between the valence band of the absorber and the p-selective layer, as already shown in the schematic in Fig. 2.4. This is, equal to the control of the perovskite film quality, a critical task when developing high-efficiency solar cells due to the importance of efficient charge separation and transport [63].

Despite the excellent physical properties of perovskite materials and all the related progress that has been made up to date, the way towards commercialization is still long and can only be speeded up when solutions to some serious issues are found. Organolead halide perovskites are sensitive to moisture, heating and UV illumination, i.e. they suffer heavily from degradation under realistic environmental conditions. Further intrinsic instabilities affecting the interfaces and the electrical field, mainly induced by the simultaneous motion of ionic species in the perovskite, have to be understood in detail. Understanding ion migration might be a key for solving the exceptionally pronounced current-voltage hysteresis and photoinduced phase separation [64–69]. Furthermore, the photophysical properties have to be investigated in-depth in order to clearly identify fundamental mechanisms in the films. Indeed, many experiments have already been performed to shed light on the variety of charge transport and dynamics in perovskites, however, a comprehensive model describing theses processes especially in the operational mode of solar cells is still lacking. The knowledge of these properties is beneficial for further boosting the efficiency to the Shockley-Queisser limit. Another challenge related to commercialization of perovskite-based PV is the development of large-area and stable modules [70–73]. To this end, the fabrication process as well as the stacking sequence must be adjusted to low-cost and large scale printing, preferably a roll-to-roll technique, without diminishing the efficiency in a substantial manner. Also, special attention has to be paid to environmental issues, more precisely the easy dissolvability of halide perovskites and thereby the toxicity of lead. Because tin-based solar cells do not seem to be suited for large-scale applications until now, a proper and safe encapsulation of lead perovskite-based devices is mandatory.

The long-term perspective of perovskite thin film technology is the integration into a tan-

dem photovoltaic device as a top cell. This will most likely happen with the PV working horse silicon [74, 75] since its technology is highly developed and the production has become in the meantime less expensive. However, a tandem structure with CIGS as the bottom cell is also possible and subject to intense studies [76, 77].

3 Experimental details

This chapter gives a full overview of the time-resolved measurement techniques employed for the characterization of the thin film systems, namely time-of-flight (ToF) and photoluminescence combined with time-resolved single photon counting (TCSPC). Each setup is depicted schematically including all major components necessary to perform the respective measurements whereas a detailed description of the techniques is provided as well. The protocols for the fabrication of the samples are also briefly described.

3.1 Time-of-flight setup

Charge carrier mobilities can be probed in different ways on either macroscopic or microscopic length scales, which renders the comparison of values obtained by varying techniques a challenging topic. Firstly, charges have to be generated. This can occur by applying an external field (FET), injection (SCLC), doping (CELIV) or illumination (ToF, photo-CELIV, TRMC,...) [78]. Because the operation of solar cells depends on the light-generated charges, the ToF technique is applied within this work to study the charge carrier mobilities in perovskite thin films.
The ToF transient photocurrent technique is based on the generation of charges in a photoactive layer upon pulsed light while a constant external DC bias is applied to the contacted sample. The created charges are thus separated and start moving towards the corresponding electrode which gives rise to a photocurrent, either dominated by holes or electrons, depending on the polarity of the DC field. Further detailed analysis of the obtained current-time profile provides information about hole and electron mobilities in the investigated material [78].
Fig. 3.1 shows the layout of the home-built time-of-flight setup used for charge carrier mobility studies. Pulsed light is provided by a laser system consisting of an optical parametric oscillator (OPO) pumped by a solid-state Nd:YAG laser (Spitlight 600, InnoLas) with a pulse length of 7 ns and a repetition rate of 20 Hz. While the wavelengths provided by the pump laser cannot be tuned in a continuous manner (fundamental wavelength at 1064 nm, 532 nm by second harmonic generation and 355 nm by third harmonic generation), the OPO allows for the generation of the wavelength needed to satisfy the absorption properties of the material of interest and hence the creation of a sufficient number of charges. The OPO can operate at signal wavelengths between 410 and 709 nm and idler wavelengths between 710 and 2630 nm. It can furthermore be used as a pump source for a frequency doubler which extends the excitation regime from the visible and infrared to the ultraviolet range of light between 206 and 410 nm.

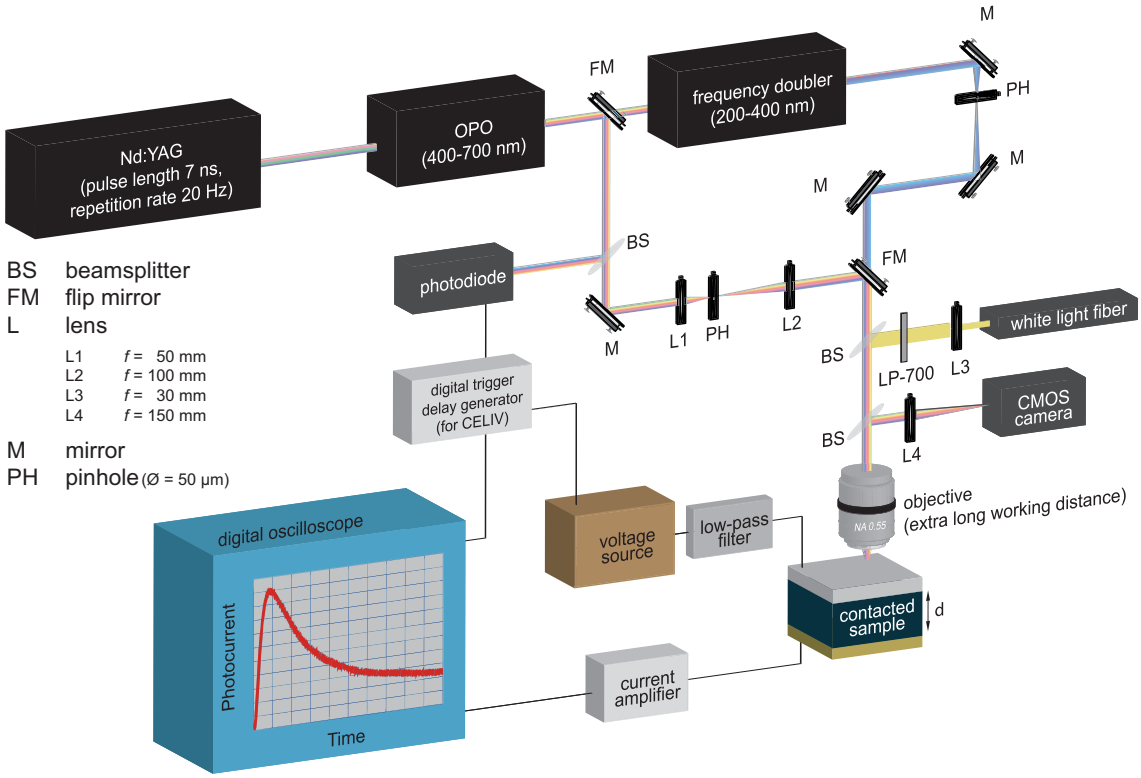

Fig. 3.1 Layout of the home-built experimental setup employed for time-resolved photocurrent studies via the ToF technique. Pulsed laser light is provided by a solid-state Nd:YAG laser. Due to a constant external bias, charge carriers generated in the photoactive layer are separated and move to the corresponding electrodes. The photocurrent is then visualized via a fast oscilloscope, allowing for further processing to obtain information on charge carrier mobilities in the respective investigated systems.

The investigated sample is illuminated from its semi-transparent side (usually glass/FTO or glass/gold) by focusing the light through an objective (Nikon; NA 0.55, spot diameter approximately 2 µm) with an extra long working distance. Additionally, the use of an objective permits the observation of the sample structure by focusing reflected white light from the illuminated surface onto a CMOS camera, which becomes crucial in the case of in-plane electrodes where the position of the laser's excitation spot on the film is of prime importance. An independent voltage source (Sourcemeter 2400, Keithley) is connected to one contact via the ohmic resistance of a low-pass filter (housed in a metallic case) while the generated photocurrent is extracted through the opposite contact and amplified (DHPCA-200, FEMTO). Simultaneously, the amplifier is connected to the capacitor of the low-pass filter. This guarantees a closed circuit (see Fig. 3.2), furthermore, only the use of the filter allows applying a voltage to the sample and eliminates noise phenomena occuring when connecting the voltage source directly with the sample. The photocurrent is also converted through the amplifier and finally directed to the fast digital oscilloscope where it is being recorded (Wavesurfer 452, LeCroy).

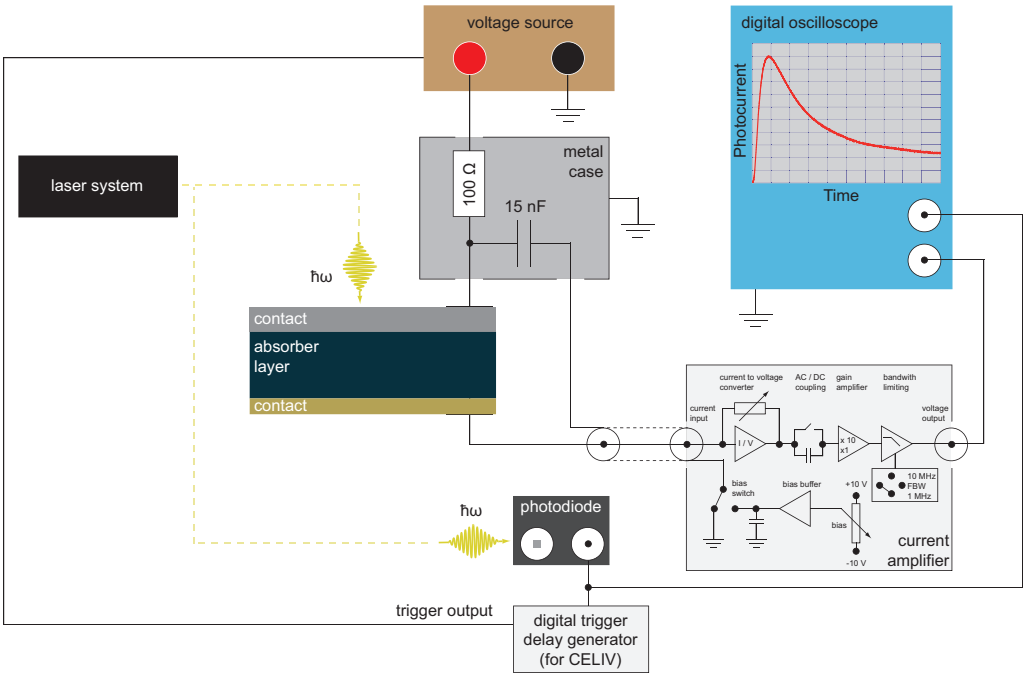

Fig. 3.2 Detailed representation of the circuit for time-resolved ToF experiments. One contact terminal of the sample of interest is connected to the external voltage source through the ohmic resistance of a low-pass filter which is housed in a metallic box. Illumination is provided via the laser system whereas the generated photocurrent is extracted via the second contact and directed to a current amplifier. The latter is connected to the capacitor of the low-pass filter and guarantees a closed circuit. The photocurrent is being converted to a voltage and guided to the digital oscilloscope. Triggering is done via a conventional photodiode using a small fraction of the laser pulses.

From the ToF transients the transit times of holes and electrons can be determined (see Chap. 4-Chap. 8), either directly when the materials shows non-dispersive transport or via a double-logarithmic plot in case of dispersive transport [78, 79]. When a photogenerated sheet of charge carriers, created upon pulsed excitation, starts to drift due to the external DC field, the photocurrent increases immediately resulting in a spike in the transient. While the carriers are traveling through the material, the current flows constantly (plateau) until charges arrive at the opposite electrode (drop in the transient) and leave the sample. Then the current declines quickly and the transient is said to be non-dispersive, as depicted in Fig. 3.3 such that the transit time of the charge carriers can easily be determined from the crossing point of the linear fits describing the plateau and the decay of the $j-t$ profile (black lines in Fig. 3.3 b). The experimentally measured current $j(t)$ is described by:

$$j(t) = \frac{1}{d}\int_0^d j_c(x,t)\,\mathrm{d}x \tag{3.1}$$

with j_c being the conduction current density. In case of dispersive transport, observed for example in amorphous silicon and many organic materials, the shape of the ToF transient does not any longer allow for the direct determination of the transit time from the linear plot since the necessary features plateau and kink are not clearly visible due to a smearing

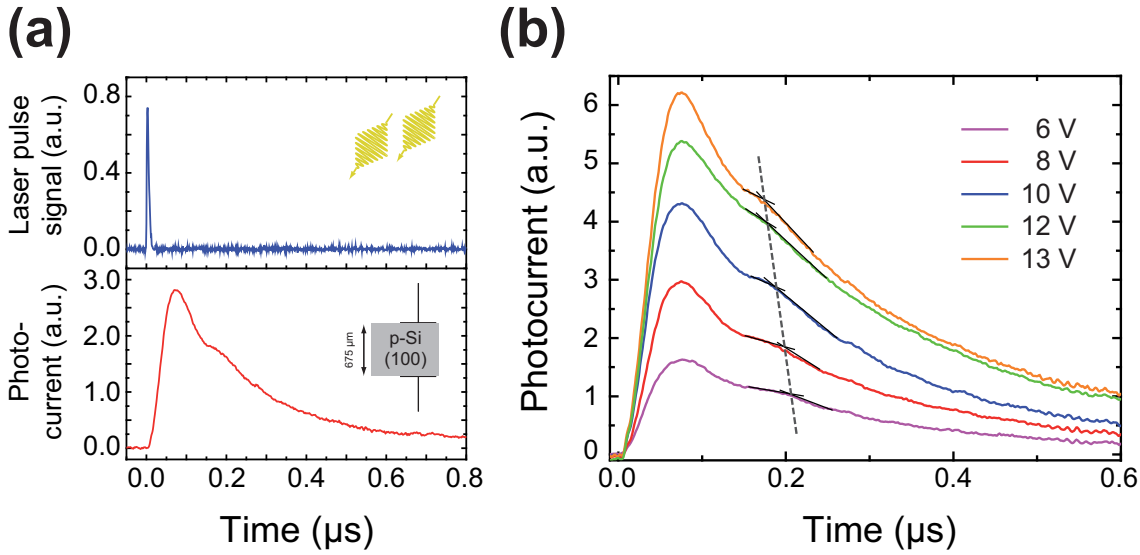

Fig. 3.3 Transients recorded for a p-doped (100) silicon wafer. The sample serves here as a reference system to ensure proper calibration of the ToF setup. (a) Laser pulse, visualized via a photodiode, and representative ToF trace for the reference system. (b) *j-t* profiles at different applied DC voltages. The current increases for increasing bias voltage, while simultaneously the kink of the transients moves to smaller transit times (grey dashed line).

of the transit edge. Instead, data analysis has to be performed in a log-log plot of the transient to make the kink visible while the transit time is defined by the intersection of the linear regression of pre- and posttransit regime. The origins of the featureless and continuously declining current are seen in the loss of carriers induced by deep trapping, sample inhomogeneities, local field variation because of trapped charges and spreading of the sheet of charges due to multiple trapping, hopping or dispersion of distances between neighboring sites [78, 79]. Further data analysis which is required for the extraction of charge carrier mobility is described in detail in the following chapters.

To ensure successful operation of the ToF setup, a commercially available p-doped silicon wafer was first examined before performing all following experiments presented within this work. Fig. 3.3 a shows the trigger signal from the laser system and the obtained transient upon pulsed excitation. Due to the voltage series performed in Fig. 3.3 b showing increasing current and decreasing transit times for increasing bias voltages as well as a mobility value of around 800 cm^2/Vs that is in agreement with reported values (400-1600 cm^2/Vs [80–84]), the measurement system is proven to work properly.

3.2 Time-resolved photoluminescence setup

Contactless experiments targeting on the optical properties including charge carrier transport and lifetimes in photoactive materials were performed on an experimental setup based on a confocal optical microscope (see Fig. 3.4). The setup is equipped with a closed-loop piezo scan stage which allows to raster-scan the sample through the focus of an objective

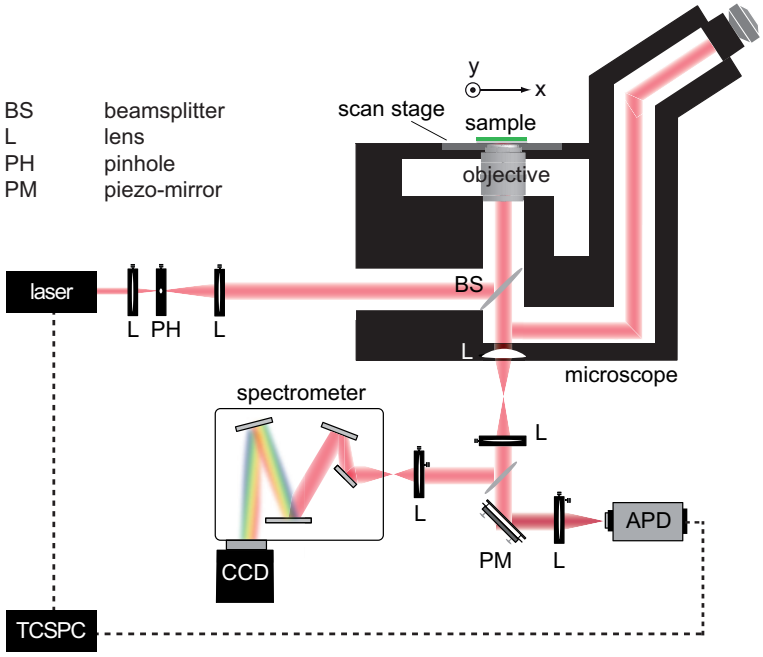

Fig. 3.4 Scheme of the confocal microscopy setup used for time-resolved photoluminescence experiments. The sample is positioned on a piezo-stage allowing for raster scanning while the photo-response upon pulsed excitation is collected in epi-detection. The signal can be detected by a spectrometer or an APD, whereas the latter is connected to TCSPC electronics. An additional piezo-mirror in the detection path enables remote detection of light with respect to the excitation position. Based on [85].

with NA = 1.4 (sample scan). Laser excitation is provided by a pulsed diode laser operating at a wavelength of 510 nm and a repetition rate of 1 MHz. The photoresponse of the material upon laser excitation is detected at wavelengths longer than 615 nm. The detection beam path is equipped with a spectrometer and an avalanche photodiode (APD) in combination with electronics for time-correlated single photon counting (TCSPC) which allows for a spatially and temporally resolved detection of the photoluminescence. An additional closed-loop piezo scan mirror in the detection beam path (detection scan) allows for remote detection of the generated PL signal with respect to the fixed excitation position. The focal length of the collimation optics was chosen to form a diffraction-limited detection spot with a diameter of approximately 300 nm which can be raster-scanned with respect to the excitation position.

As mentioned above, temporal resolution of the photoluminescence experiments is achieved by TCSPC, a highly sensitive technique allowing for the measurement of fluorescence lifetimes on a picosecond scale. This kind of experiments requires electronics that connect the measured signals to the periodicity of the laser operating at high repetition rates. The laser pulse triggers a measurement that determines the time between the release of the excitation pulse and the detection of a PL photon by the APD. Fig. 3.5 depicts the layout of the optical beam path employed for TCSPC experiments. From a conceptional point of view, the detection of a photon is a rare event resulting in a certain number of periods where no signal is detected while in some periods a single photon pulse is measured.

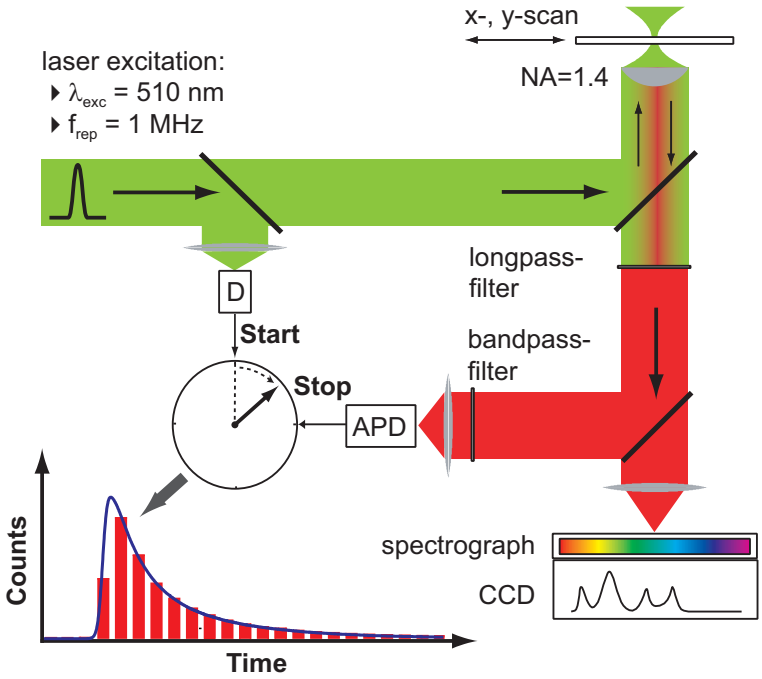

Fig. 3.5 Layout of the optical beam path and electronics employed for TCSPC measurements. A picosecond pulsed laser excites the sample while the photoresponse events are detected by the TCSPC electronics. Statistical processing allows for the measurement of the photon distribution as a function of time. Adapted from [85].

As soon as a photon is detected, its arrival time is measured by the electronics. After a large number of signal periods, the recorded photon emission events with the related arrival times are post-processed. The photon distribution over time is reproduced from the intensity and the time distribution of all photons emitted from the sample, resulting in a waveform-like shape that reflects the photon probability distribution histogram [86]. From these transients, valuable information can be extracted. The rise of the transient provides insights into the transport time of charge carriers for a given distance while the decay unveils the lifetime of charges, i.e. the time between generation and recombination of a hole and an electron.

3.3 Fabrication of laterally arranged in-plane gold contacts

To perform electrical measurements on pristine organolead-halide perovskites via ToF, an adapted contact pattern was designed which can easily be deposited on commercial glass substrates by a thermal evaporation process. In this manner, distance dependent lateral ToF measurements can be realized [87–91] which are not accessible in vertical dimensions due to thickness restrictions given by the corresponding thin film fabrication protocols and the resulting fast charge transport in thin films in vertical direction which cannot be resolved by the employed setup. Additionally, probing charge transport in lateral direction enables the measurement of photocurrent at different charge carrier travel distances and the investigation of the effect of crystallite size and grain boundaries on the mobility.

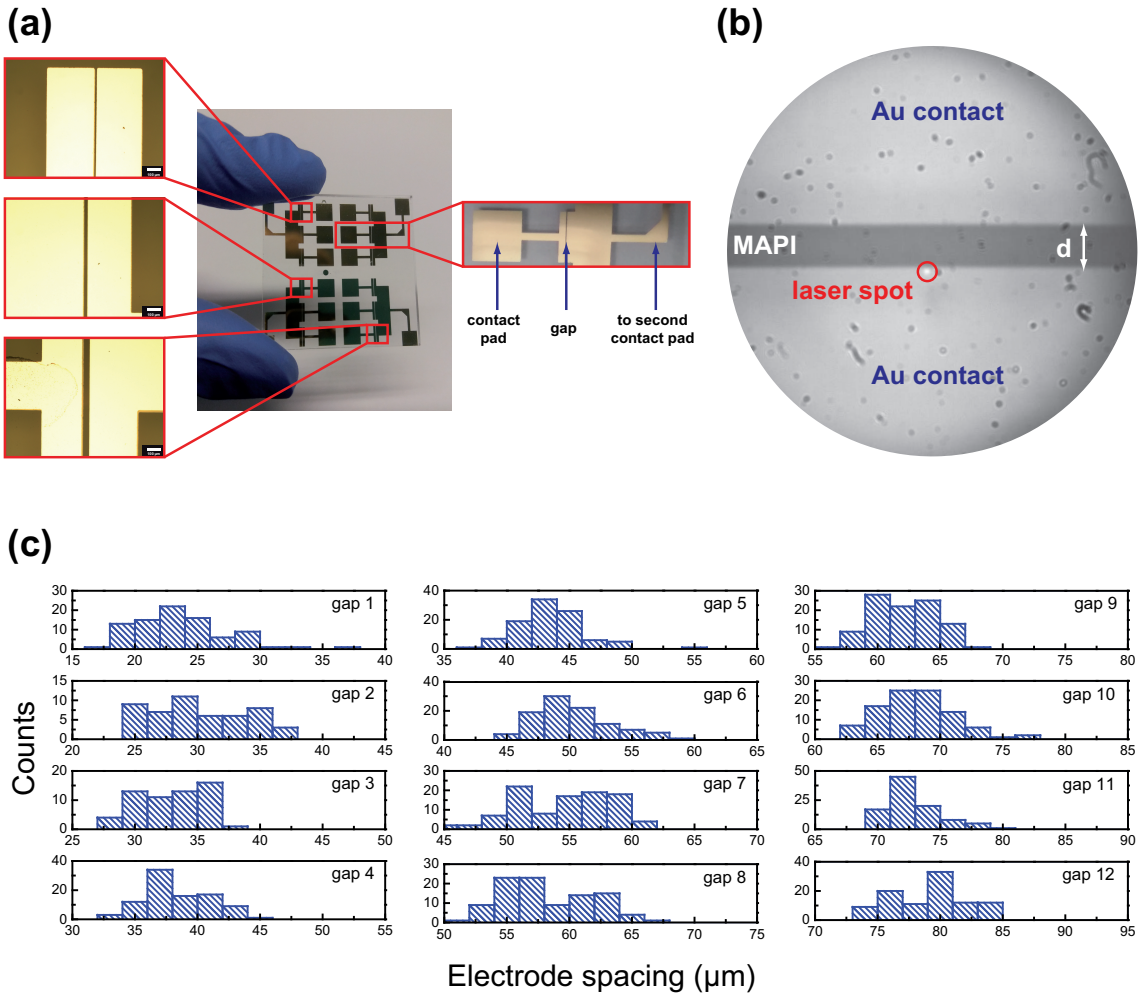

Fig. 3.6 Images of the lateral contact pattern and analysis of the gap sizes. (a) Photograph of a typical substrate with lateral contact pattern deposited on top and magnified representation as seen through a light microscope. (b) Top view of a laterally contacted perovskite film through the objective of the ToF setup. The gap filled with perovskite material is clearly visible while the contacts are separated by a defined distance d. Charges are generated in the spot created by the laser light. (c) Statistical evaluation of more than 100 electrode spacings in the lateral contact pattern fabricated via thermal evaporation of gold through a shadow mask.

Prior to all subsequent lithography steps, glass sheets were cleaned with a 2% Hellmanex solution and rinsed with deionized water. Afterwards the substrates were sonicated for 5 min in acetone and later with 2-propanol and exposed to oxygen plasma for 10 min to ensure the removal of surface residues and subsequent adhesion of the metallic contacts on glass. The structures were created via microstencil lithography by first depositing a 5 nm thick film of titanium as adhesion layer and then a 30 nm thick layer of gold through a microscale shadow mask via thermal evaporation under vacuum (10^{-7} mbar), resulting in contact patterns with inter-electrode distances between approximately 20 and 80 µm in steps of 5 µm. If necessary, the contacts were once again exposed to oxygen plasma for 1 min to improve the wetting properties of the precursor solution and thus to ensure a homogeneous growth of perovskite thin films, especially in the gaps between the

Tab. 3.1 Analysis of more than 100 electrode spacings in the lateral contact pattern. The obtained gap sizes fit well with the ones specified for the evaporation mask by the manufacturer.

Gap	Expected electrode spacing [µm]	Mean electrode spacing [µm]	Number of short circuits
1	20	22 ± 3	14
2	25	29 ± 4	49
3	30	33 ± 3	41
4	35	37 ± 2	7
5	40	42 ± 3	-
6	45	49 ± 3	-
7	50	53 ± 4	-
8	55	57 ± 3	-
9	60	62 ± 2	-
10	65	67 ± 3	2
11	70	72 ± 2	-
12	75	78 ± 3	-

contacts, on the rather smooth gold surface. Next, the sizes of the electrode spacings were determined with a conventional optical microscope (see Fig. 3.6 a). Fig. 3.6 b shows the top view of a typical substrate with in-plane contacts covered with perovskite material seen through the objective of the time-of-flight setup (see Fig. 3.1). The gold contacts are separated by a defined distance d in the micrometer range whereas the perovskite film between the gaps extends as well to the plane behind the image. Charge generation is supported by the focused laser spot (red circle) which is positioned on the margin of one electrode close to the perovskite film. Because charges are created locally at one electrode, one type of carriers is immediately extracted while the other type of charge carriers moves along d to the opposite electrode when applying a constant external field. Hence, by changing the polarity of the DC field the mobilities of electrons and holes can be determined separately.

The respective statistical evaluation of the gaps is shown in Fig. 3.6 c and Tab. 3.1. The variations in the measured sizes with respect to the spacings specified for the mask by the manufacturer and the different evaporation cycles in terms of batch-to-batch variations can be attributed to slightly varying positions of the evaporation mask holder above the gold boat in the vacuum chamber.

3.4 Solar cell fabrication

In order to analyze the effect of different perovskite materials in terms of synthesis protocol or composition on the performance of solar cell devices incorporating the perovskite as absorber layer, the respective photovoltaic devices were fabricated following a state-of-the-art procedure (in collaboration with the research group of Dr. Docampo, LMU Munich). For this purpose, fluorine doped tin oxide (FTO) coated glass substrates (7 Ω, Hartford Glass) were patterned using zinc powder and 3 M HCl. Then the sheets were successively cleaned with deionized water, 2% Hellmanex solution, then once again with deionized water, acetone and ethanol. Oxygen plasma treatment for 5 min before applying the blocking layer supported in the removal of organic residues on the surface.
The substrates were then covered with a sol-gel derived TiO_2 layer by spincoating the precursor solution and calcining at 500 °C in air [92]. For the sol-gel solution a 27.2 mM solution of hydrochloric acid in 2-propanol (typically 35 µL of 2 M HCl and 2.53 mL of isopropanol) was added dropwise to a 0.43 mM solution of titanium isopropoxide in anhydrous 2-propanol (369 µL titanium isopropoxide in 2.53 mL of 2-propanol) under vigorous stirring. During addition, the solution remained clear and transparent.
After deposition of the hybrid perovskite film following the respective synthesis procedure (described in detail in the following chapters), the stacked film architecture was spincoated at 1500 rpm for 45 s with a layer of spiro-OMeTAD serving as hole transporting layer within the photovoltaic device. For this purpose, 96 mg of spiro-OMeTAD in 1 mL of chlorobenzene were mixed with 10 µL 4-tert-butylpyridine (tBP) and 30 mL of a 170 mg/mL bis(trifluoromethane)sulfonamide lithium salt (LiTFSI) in acetonitrile as additives. Before depositing the 40 nm thick top gold electrodes by thermal evaporation of gold under vacuum (approximately 10^{-7} mbar), the sample was kept over night at room temperature and 30% relative humidity to allow oxidation of spiro-OMeTAD.

4 Controlling crystal growth by chloride-assisted synthesis: Towards optimized charge transport in hybrid halide perovskites

The following chapter is based on the publication **Controlling crystal growth by chloride-assisted synthesis: Towards optimized charge transport in hybrid halide perovskites** [93] and investigates two $CH_3NH_3PbI_3$ (MAPI) films both deposited by a two-step protocol and only differing in the optional addition of a chloride containing salt to the precursor solution.[1] Although being highly akin from a chemical and structural point of view, these films show substantial differences in their optoelectronic characteristics. For chloride-treated perovskite films, an enhanced average power conversion efficiency is found as compared to untreated MAPI films. Moreover, different light-soaking behavior and increased photoluminescence lifetimes in the case of chloride-treated MAPI were observed. In-situ photoluminescence lifetime measurements during the crystallization process lead to the conclusion that the chloride addition during film deposition results in slower crystal growth, leading to fewer defects and higher crystalline order which is beneficial for efficient charge transport.

4.1 Motivation

Organic-inorganic hybrid perovskites have experienced an unexpected scientific boost rendering them the fastest advancing solar technology the community has ever observed. [11, 94–96]. Highly advantageous physical properties such as tunable electronic properties [43, 97] or strong optical absorption over the visible regime of light [13, 96] are considered to be some of the key features for becoming competitive with the presently used commercial technologies such as silicon and CIGS [10, 98, 99] or Cu_2O which becomes as well more and more attractive [100]. A great effort has been spent to improve and optimize different synthesis approaches with cheap bulk materials [101–104], allowing for the substantial increase of power conversion efficiencies (PCE) in perovskite-based photovoltaic devices, ranging from 3.8% [11] to 6.5% [105] in 2009 to values currently exceeding 22% [10]. Several device engineering protocols are reported to optimize the respective material properties to boost device efficiencies. Amongst others the addition of chloride-containing compounds to the methylammonium iodide precursor solution for

[1] Thin film and solar cell preparation done by N. Giesbrecht and F. C. Hanusch (group of Dr. Docampo), PL experiments done by K. Handloser (group of Prof. Hartschuh), in-situ PL lifetime experiments done by F. C. Hanusch (group of Dr. Docampo).

the synthesis of methylammonium lead triiodide (MAPI) films in a two-step solution deposition route became very interesting due to the improved PCE values by this synthesis protocol [39, 44–46]. Although an incorporation of chloride ions into the final crystal structure has not been detected yet by any analytical procedure, the function of chloride for the control of the resulting optoelectronic properties seems to be crucial, but still remains unclear. In the following, the properties of chloride-treated MAPI thin films were investigated and compared to the results obtained for untreated MAPI films in order to provide an explanation for the effect of chloride addition during film synthesis. First, the morphology and crystalline structure of the materials were determined by means of scanning electron microscopy and X-ray diffraction together with the optoelectronic properties of the respective films. Then, the charge carrier mobility and dynamics in the two films were studied using the time-of-flight (ToF) technique and time-resolved photoluminescence (PL) , both ex-situ as well as in-situ during the crystallization processes. These in-situ photoluminescence lifetime measurements highlight that the chloride addition during film deposition results in slower crystal growth, leading to fewer defects and higher crystalline order.

4.2 Materials and methods

Preparation of the precursor solutions and perovskite thin film deposition was done following a previously published synthesis route [39, 44]. Briefly, 24 mL of a 33% methylamine solution in ethanol were diluted by using 100 mL of absolute ethanol. To this solution, 10 mL of an aqueous solution of hydroiodic acid (57 wt%) or 15 mL of concentrated hydrochloric acid (37% in water) were added under constant stirring. The reaction was continued for one hour at room temperature before removing the solvents by rotary evaporation. The so obtained white solid was washed with dry diethyl ether and recrystallized from ethanol. A thin layer (ca. 200 nm) of lead iodide was deposited on the corresponding substrate by dynamic spincoating at 3000 rpm for 15 s using 100 µL from a 0.85 M lead iodide solution in *N*,*N*-Dimethylformamide (DMF, Sigma), whereas lead iodide (99%, Sigma) as well as DMF were used as received. Importantly, both substrate and precursor solution have to be heated up to a temperature between 60 and 65 °C before starting the spincoater in order to confirm the formation of visually smooth films [44]. The immersion solutions were prepared by dissolving 9.5 mg/mL methylammonium iodide and 0.5 mg/mL methylammonium chloride in anhydrous isopropanol (Sigma) during heating to 60 °C. Accordingly, the immersion solution for the preparation of pure MAPI films was prepared by dissolving solely 10 mg/mL methylammonium iodide in dry isopropanol at 60 °C. The lead iodide containing films were immersed in 40 mL of the heated solutions for 5 min whereas the temperature of the solution was constantly kept at 60 °C. Once the conversion was finished, the MAPI films were washed with clean, anhydrous isopropanol and dried under a nitrogen stream. The obtained perovskite films revealed an average thickness between 400 and 450 nm, estimated via scanning electron microscopy cross-

sections. After finalizing the synthesis procedure, the films were coated with a thin layer of poly(methyl methacrylate) (PMMA) by spincoating 50 mg/mL PMMA in anhydrous chlorobenzene in order to avoid degradation through ambient moisture. Fabrication of the solar cell devices based on these films was done following the procedure presented in Chap. 3.

Laterally arranged gold contacts were fabricated in a cleanroom facility via optical lithography, as introduced in Chap. 3. Prior to all lithography steps, glass sheets were cleaned with a 2% Hellmanex solution and rinsed with deionized water and isopropanol. After sonication for 5 min in acetone and rinsing with 2-propanol, the substrates were exposed to oxygen plasma for 10 min to remove surface residuals and to facilitate adhesion of the metallic contacts on glass. Using a positive resist in combination with a bonding agent, the structures were created via UV-illumination and developed in an diluted aqueous solution of sodium hydroxide. Before depositing a 10 nm thick layer of TiO_2 and a 30 nm thick layer of gold via e-beam evaporation under vacuum (10^{-7} mbar), the samples were cleaned with deionized water and dried in a nitrogen flow. The lift-off of residual gold from the glass substrate was performed in anhydrous dimethyl sulfoxide at 80 °C. Finally, the coated glass sheets with inter-contact distances between 7 and 13 µm were cleaned with 2-propanol. Deposition of the perovskite thin films was done according to the fabrication protocol mentioned above.

4.3 Results and discussion

Methylammonium lead triiodide (MAPI) thin films investigated in this work were fabricated via a two-step solution deposition conversion protocol [39, 44], representing one of the state-of-the-art synthesis techniques. From this procedure, either MAPI films, in the following referred to as “pure MAPI”, or “chloride-treated MAPI” films are obtained. When comparing these films by different analytical techniques including scanning electron microscopy (SEM) (Fig. 4.1 a and b) and UV-Vis spectroscopy (Fig. 4.1 d), no significant differences could be observed. In particular, the X-ray diffraction (XRD) patterns obtained for the two materials (Fig. 4.1 c) are virtually identical indicating that the same crystal structure is formed and that the addition of the chloride salt during film synthesis does not lead to an incorporation of chloride anions into the final film structure. This is in agreement with previous experiments performed at the LMU [44] and experiments conducted by other groups suggesting that MACl sublimes in the course of the film fabrication [106]. Furthermore, a multitude of other analytical techniques, including energy dispersive x-ray spectroscopy (EDX) , electron diffraction and electron energy loss spectroscopy (EELS) , have been used before on the same sample materials confirming their very similar chemical and structural properties [44].
When incorporating these compounds in planar photovoltaic devices (see SEM cross sections shown in Fig. 4.1 a) substantial differences in their performance are observed

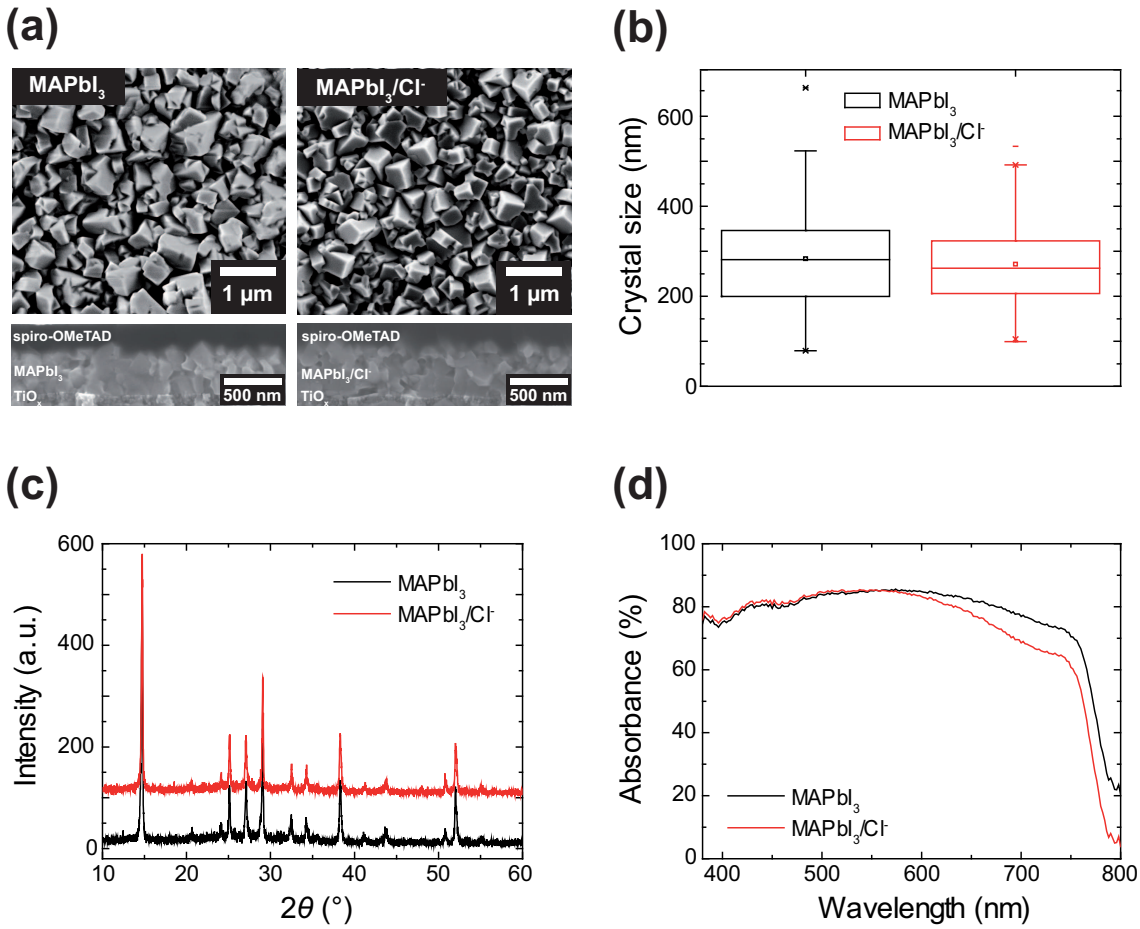

Fig. 4.1 Characterization of perovskite thin films fabricated via a two-step synthesis protocol [39, 44]. (a) Top view SEM micrographs depicting the crystallites within the two morphologically similar films and cross-sections of the solar cells comprising the corresponding films. (b) Size distribution of the crystallites obtained from (a) by visual investigation, resulting in comparable average sizes of 284 nm and 271 nm for pure and chloride-treated $MAPbI_3$, respectively. (c) Corresponding diffraction patterns from XRD measurements. (d) UV-Vis spectra of the two films showing very similar optical absorption behavior.

[39, 44–46]. Solar cells based on chloride-treated MAPI reveal a significantly improved power conversion efficiency (PCE) yielding 10.3% on average and a peak around 13% compared to the system comprising pure MAPI with an average PCE value of 5.3% and a maximum around 9%, similar to reports of other groups [39,44–46]. The corresponding *J-V* performance data (Fig. 4.2 a) and the extracted statistical distribution of the resulting PCE are shown in Fig. 4.2 b.

To gain further insights into these enhancement effects of chloride addition during synthesis on the resulting films' optoelectronic properties, time-of-flight (ToF) mobility studies (see also Chap. 3) on individual laterally contacted layers of the two films with inter-electrode distances ranging from 7 to 13 µm were carried out. A scheme of the employed sample layout and the principle of the transient photocurrent measurement is depicted in Fig. 4.3 a.

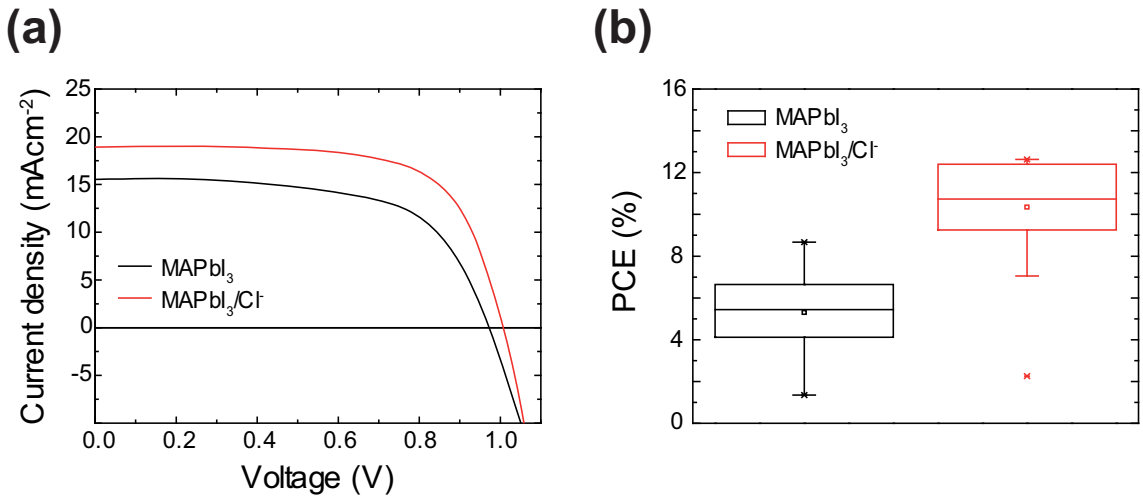

Fig. 4.2 Photovoltaic performance of the corresponding solar cells composed of the commonly used stack sequence FTO/TiO_2/perovskite/spiro-OMeTAD/gold. (a) *J-V* analysis of working devices comprising the two different $MAPbI_3$ films. (b) Statistical evaluation of power conversion efficiencies from more than 30 individual photovoltaic devices. Solar cells based on pure $MAPbI_3$ reveal a PCE of 5.3% on average, whereas chloride-treated films lead to an improved performance with average efficiencies of 10.3%.

The generated charge carriers are separated by applying a constant external DC field of approximately 7 kV/cm and thus start moving in lateral direction across the film towards the opposite electrode. Note that mobile ionic species strongly affect the material's properties and are discussed to be the origin of the anomalous hysteretic *J-V* behavior of perovskite-based solar cells [64–69]. To minimize the influence of ionic drift on the obtained ToF data, the DC electric field is switched on only during the measurement (for less than 1 s), since ion migration is known to occur on minute timescales [68, 107]. The obtained photocurrent transients for different electrode distances (Fig. 4.3 b) point out that larger distances between the lateral metallic contacts result in longer charge carrier transport times. The shape of these photocurrent transients indicates dispersive transport (see Chap. 3) that presumably results from spatially varying hopping rates due to energetic heterogeneities and electric field variations caused by trapped space charges [79].
The average hole mobility μ in pure and chloride-treated $CH_3NH_3PbI_3$ films can then be approximated by the following equation:

$$\mu = \frac{d}{E \cdot t_{tr}} \tag{4.1}$$

with d being the inter-electrode distance, $E = U_{bias}/d$ the constant applied electric field and t_{tr} the transit time charge carriers need to travel from the spot where they were generated to the opposite contact. The determination of t_{tr} follows a procedure adapted from literature [79] and was performed via linear fit functions (see Fig. 4.3 c). For higher reproducibility an automatic fit routine was programmed based on an iterative fitting of linear function modeling of the slope close to the point of interest of the measured photocurrent transient. Plotting the transient in a double logarithmic scale, the employed

algorithm identifies two linear fit functions for the plateau and the decay. Due to slight oscillations of the signal a linear fit is favorable over differentiating or integrating the respective data. The transit time t_{tr} is then equal to the time at which the two linear fits intersect (grey lines in Fig. 4.3 c). As shown in Fig. 4.3 d, chloride-treated MAPI films show decreased transit times compared to pure MAPI for the same electrode distances.

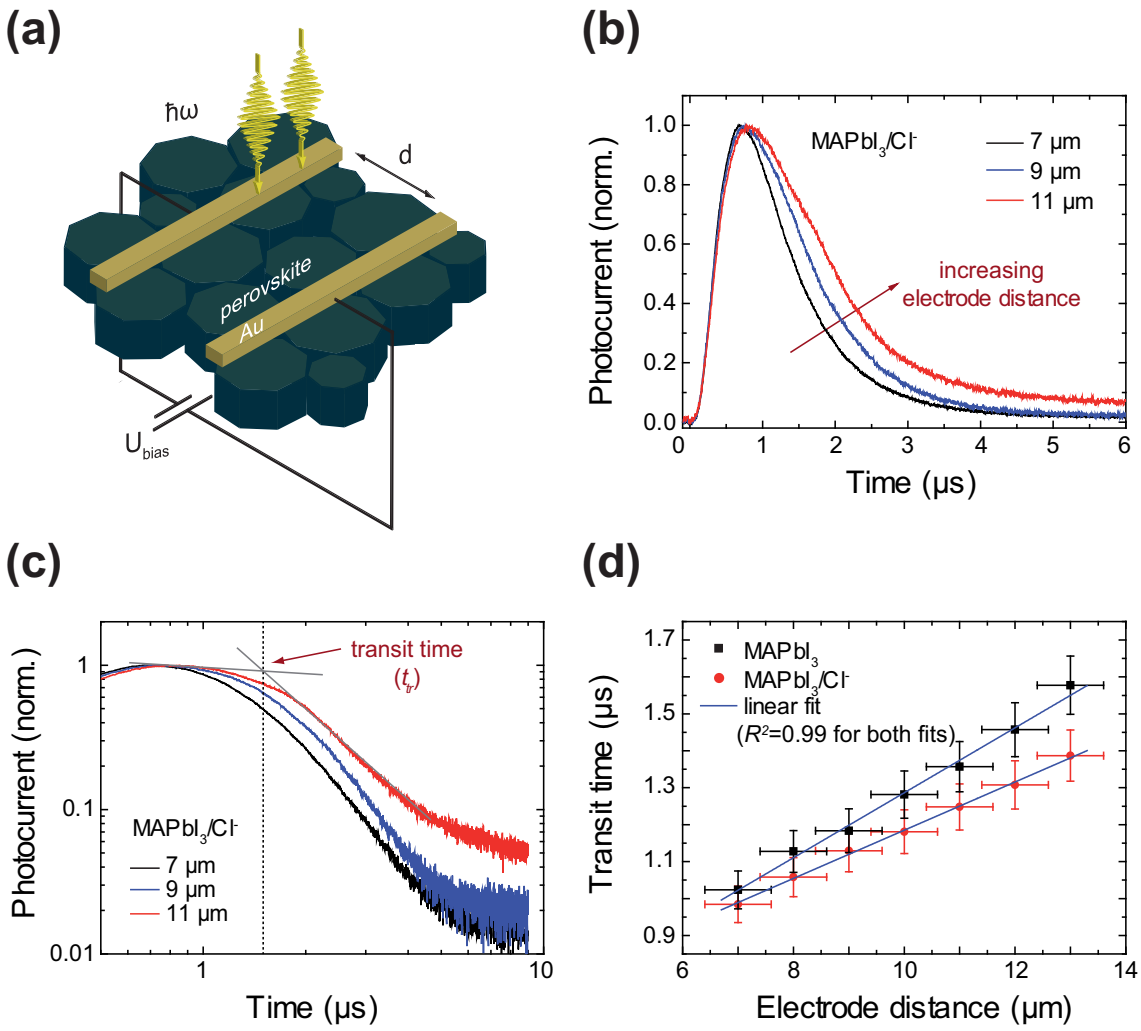

Fig. 4.3 Determination of charge carrier mobilities using time-of-flight measurements. (a) Schematic illustration of the employed sample layout. Laterally contacted perovskite films with varying distances d between the gold electrodes, ranging from 7 to 13 µm, are illuminated using pulsed laser excitation. Charge carriers are generated within the $MAPbI_3$ film and separated due to an applied electric field. (b) Representative photocurrent transients obtained after pulsed excitation and the simultaneously applied DC field. An increased gap size is reflected in larger transit times t_{tr}. (c) Fitting routine employed to extract t_{tr}, as described in the main text. (d) Extracted transit times (t_{tr}) as a function of electrode distance. From the slope of the linear fits the hole mobility μ can be derived yielding $\mu = 2.16$ cm^2/Vs for chloride-treated MAPI and $\mu = 1.62$ cm^2/Vs for pure MAPI, respectively.

In the present case of identical electrode spacings and applied DC field for both examined films, the slope of the linear regression in Fig. 4.3 d is a direct measure for the mobility

according to Equation Eqn. 4.1, i.e. a smaller slope reflects a higher mobility. For MAPI, this results in a value of $\mu = 1.62 \pm 0.11$ cm^2/Vs, whereas the hole mobility in chloride-treated MAPI is found to be significantly higher reaching $\mu = 2.16 \pm 0.15$ cm^2/Vs. Hence, the hole mobility is increased by approximately 34% due to chloride-assisted synthesis of MAPI. As noted above, the shape of the transients in Fig. 4.3 b reflects dispersive transport behavior, influenced by a distribution of energetic states and resulting in a dispersion of hopping rates [79].

The increased average charge carrier mobility in chloride-treated MAPI thus indicates a reduced energetic distribution and a lower concentration of trapping defect sites that could result from a more homogeneous crystal formation. This interpretation is supported further by the time-resolved PL studies reported below. In the literature different values for the effective mobility in solution-processed perovskite films, i.e. considering both electron and hole mobility, can be found. Note that mobilities probed with time-resolved transient THz spectroscopy range between 8 [16, 57] and 40 cm^2/Vs [108], whereas experiments employing time-resolved microwave photoconductance result in values ranging from 3 [57,109] up to 30 cm^2/Vs [54,58]. Compared to the reported moblities, these values represent a lower limit. This can be attributed to the formation of a built-in potential at the contact/perovskite interface as well as to the intrinsic contact resistance. Because measurements with this sample architecture include the influence and the effects of the metallic contact on the optoelectronic properties of the investigated perovskite material, it can be assumed that this measurement layout might resemble more closely the conditions in full solar cell devices compared to investigations of thin films in a contact-less method. Additionally, this experimental approach extracts hole mobility values in lateral dimensions, thus accumulating the influence of a high number of grain boundaries and defects as well, both representing possible trapping sites. ToF measurements in vertical direction on the other hand are difficult to implement due to film thickness being restricted by the synthesis route.

Next, time-resolved PL studies were conducted to gain further insight into the charge carrier dynamics of both films. In the experiment, a pulsed diode laser operating at 510 nm excites the sample and triggers a photoresponse from the perovskite films, which is recorded by a fast APD combined with TCSPC electronics (see Chap. 3). Previous studies [110–113] have shown that light soaking within these films significantly modifies their optical properties as well as the performance of respective solar cells [64]. For both films, the biexponential PL intensity decay [114] becomes slower when increasing the illumination duration as depicted in Fig. 4.4 a and b. Further comparison of the PL intensity obtained via temporal integration of the transients (Fig. 4.4 c) reveals that this increase in lifetime (Fig. 4.4 d) is connected to a strong increase of the PL intensity for both films following longer exposure times. For chloride-treated MAPI the PL intensity and lifetime is seen to rise for a longer time as compared to pure MAPI at the same excitation conditions. Apparently, the light soaking process is slower in the chloride treated perovskite film for the same excitation laser power and similar absorption strength (Fig. 4.1 d). The rise of

both PL intensity and lifetime can be assigned to the reduction of a non-radiative decay rate component $k_{nr,soak}$ due to the light-soaking. The PL lifetime τ can be expressed as the inverse of the sum of all decay rates following

$$\tau = \frac{1}{k_r + k_{nr} + k_{nr,soak}} \tag{4.2}$$

in which k_r and k_{nr} are the radiative and the non-radiative decay rates, respectively, that are not affected by the light soaking.

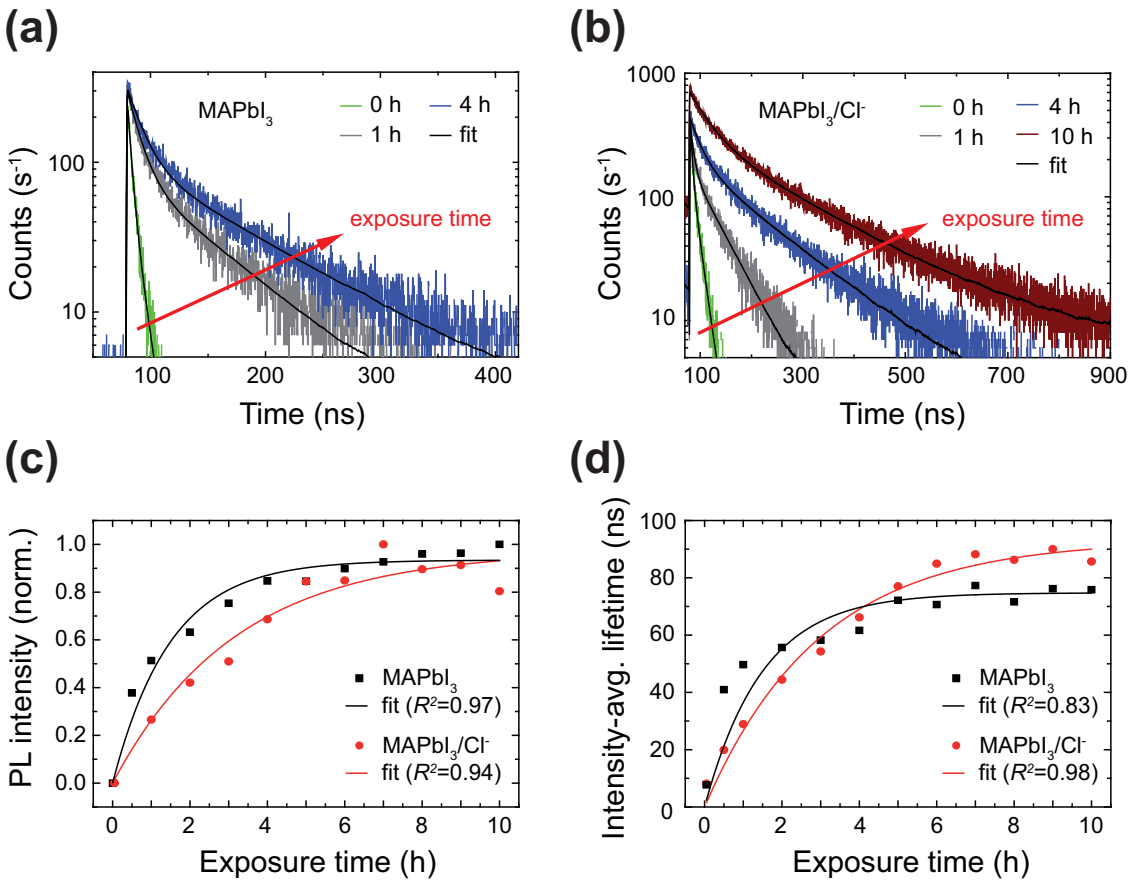

Fig. 4.4 Investigation of the optical response in the perovskite films via PL microscopy. (a) and (b) Time-resolved PL transients of a pure and a chloride-treated $MAPbI_3$ thin film, resectively, for extended exposure to pulsed laser light. In both cases, the PL decay slows down with increasing illumination time. (c) PL intensity obtained by temporal integration of the recorded PL decays. The PL intensity significantly increases with increasing exposure time and saturates within 5 hours for the pure and 10 hours for the chloride-treated film, respectively. (d) Extracted intensity-averaged PL lifetimes upon increasing exposure to light also showing slower light soaking for the chloride-treated MAPI film. Whereas pure $MAPbI_3$ exhibits an intensity-averaged lifetime of ∼70 ns for steady-state conditions, i.e. after full light-soaking, chloride-treated MAPI exhibits a lifetime of ∼100 ns. The solid lines in c and d are fits using the same exponential model function for a non-radiative rate component that is reduced by light soaking (see text).

Assuming first order reaction kinetics underlying the light soaking process [114], the non-radiative rate $k_{nr,soak}$ decays according to $k_{nr,soak}(0) \cdot exp(-t_{exposure}/\tau_{soak})$. Thus the

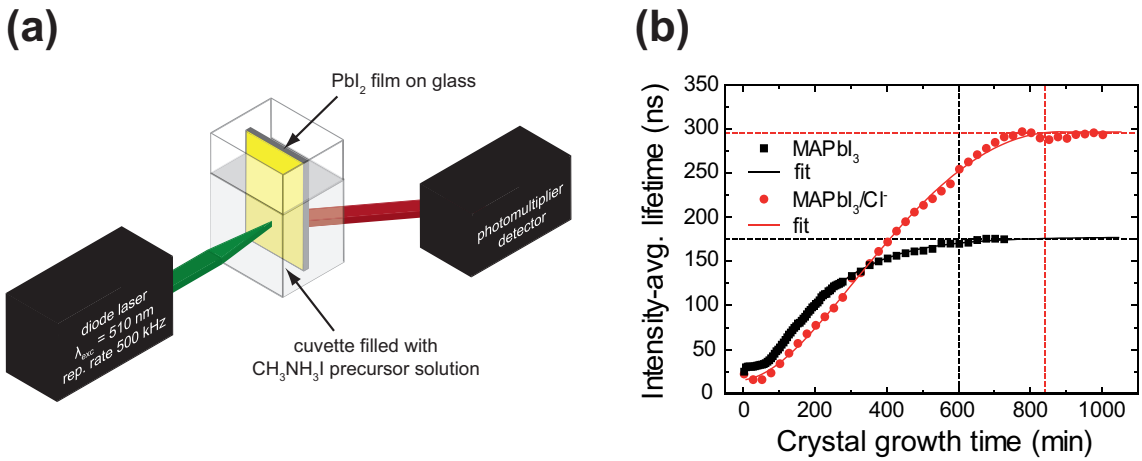

Fig. 4.5 In-situ photoluminescence studies of perovskite film formation at room temperature. (a) Schematic illustration of the setup used for the in-situ PL studies. While immersing a PbI_2 coated glass substrate into a methylammonium iodide or mixed methylammonium iodide/chloride solution, PL transients upon pulsed laser excitation are recorded over a time frame of 1000 min. (b) Intensity-averaged lifetimes during formation of pure and chloride-treated MAPI films. Stable lifetime values are obtained after 600 min for pure MAPI, revealing a lifetime of 175 ns, and after 840 min for chloride-treated MAPI with an intensity-averaged lifetime of 295 ns.

corresponding fit function $\propto 1/(k_r + k_{nr} + k_{nr,soak}(0) \cdot exp(-t_{exposure}/\tau_{soak}))$ was used, which is seen to reproduce the exposure time dependence $t_{exposure}$ of the PL lifetime very well (Fig. 4.4 d). Importantly, the same fit function with the same fit parameters can also be used to describe the exposure time dependence of the PL intensity in Fig. 4.4 c, which is porportional to $(k_r \cdot \tau)$. From the fits of the data shown in Fig. 4.4 c and d, the soaking time constant of $\tau_{soak} = 1.5$ h for the pure and of $\tau_{soak} = 3.0$ h for the chloride-treated film, respectively, were obtained, supporting the notion that light soaking is slower for the chloride-treated film. Furthermore, the PL intensity after light soaking is completed is higher for chloride-treated MAPI as compared to pure MAPI indicating a lower non-radiative recombination rate k_{nr} and thus a decreased number of traps since the intensity is proportional to $(k_r/(k_r + k_{nr}))$. The intensity-averaged lifetime amounts approximately 70 ns for pure MAPI and 100 ns for the chloride-treated film when reaching saturation. This observation can be as well assigned to a reduced number of quenching sites in the chloride-treated film caused by an optimized crystal growth. Furthermore, this could indicate a reduced crystallization speed [115] induced by the presence of chloride in the precursor solution.

The deposition technique and the crystallization dynamics are considered to be the most important factors influencing the thin film properties of the respective hybrid perovskite compound [39,40,43,51]. Previous investigations [116] suggest a crucial role of chloride in a templating process during crystallization in chloride-assisted fabrication protocols. Hence, to confirm assumptions on a slowed down crystal growth in chloride-treated MAPI, in-situ PL studies during film formation were performed. For this purpose, PL transients were acquired on a lead iodide coated glass substrate immersed in the respective precursor solu-

tion (see Fig. 4.5 a) at room temperature. In contrast to the typical growth temperatures chosen for MAPI films of 60 °C, at which growth is completed within few minutes, the experiment had to be performed at room temperature to be able to resolve the growth dynamics. The intensity-averaged lifetimes, derived from the PL transients being fitted with a biexponential decay function, are shown in Fig. 4.5 b. For both materials the lifetimes strongly increase during growth. This suggests that during growth a high density of quenching defect states is present at the crystal surface, which subsequently disappear upon crystal formation. For the pure precursor solution the growth is completed after about 600 min while for the chloride-containing precursor growth is slower, taking about 840 min. The final films show intensity-averaged lifetimes of 175 ns and 295 ns for pure and chloride-treated films, respectively. This confirms the trend seen in Fig. 4.4. This can be attributed to a lower defect density in chloride-treated MAPI, which is the origin of the longer lifetime, to slower crystal growth. Furthermore, in the typical growth procedure the films are removed from the growth solution before the maximum crystal size is reached. In the experiment shown in Fig. 4.5 there is no temporal limitation to the crystal growth since the PL measurement was performed over several hundreds of minutes which enables and facilitates the enhancement of the crystal size.

4.4 Conclusion

In this study, pure and chloride-treated methylammonium lead triiodide thin films, both very similar in morphology and other material characteristics [44], were investigated. Major differences were obtained for the charge carrier dynamics in chloride-treated MAPI, such as increased hole mobility and higher PL intensities and lifetimes, as well as improved solar cell performance. Based on the in-situ PL measurements, this enhancement of transport characteristics can be attributed to the slow-down of the crystallization speed during the growth of the film induced by the presence of chloride, thus leading to considerably fewer defects and quenching sites in the individual MAPI crystals. This mechanism could also be applicable to other hybrid halide perovskite materials and could help in optimizing the performance of future photovoltaic devices.

5 Two-step vs. one-step deposition: Tuning the opto-electronic properties in perovskite solar cells

In this chapter, the opto-electronic properties of $CH_3NH_3PbI_3$ thin films fabricated via two different preparation methods are studied: One-step fast-crystallization deposition (FDC) and two-step solution deposition conversion (SDC). Using time-resolved photoluminescence (PL) microscopy, a substantially higher charge carrier diffusion constant for two-step SDC derived MAPI thin films is found. Improved transport characteristics are also observed in time-of-flight measurements on laterally contacted MAPI thin films yielding 1.6 times higher charge carrier mobilities for FDC MAPI. When incorporated into devices, FDC MAPI based solar cells show a lower series resistance and consequently higher power conversion efficiencies on average as compared to two-step SDC MAPI.[2] The improved opto-electronic performance of FDC MAPI thin films can be attributed to their morphology with larger crystallites and fewer grain boundaries as compared to thin films deposited using the two-step SDC protocol.

5.1 Motivation

High power conversion efficiencies, facile solution processing and compatibility with current printing technology render metal halide perovskites a competitive class of materials for large-scale photovoltaic systems. [11, 43] The opto-electronic performance of these materials already matches up [13, 114] with industry staples including GaAs, CIGS and silicon [10,98,99]. The rapid improvement of device efficiencies surpassing 22% to date has been fuelled by the optimization of perovskite deposition methods with the crystallization dynamics appearing to be the key element [39, 40, 43, 51]. Two techniques that have attracted particular attention are the two-step solution deposition conversion (SDC) [40,44] and the fast crystallization-deposition (FDC) method [42, 43]. Both approaches result in highly uniform $CH_3NH_3PbI_3$ (MAPI) thin films with complete surface coverage. Yet, the efficiency of devices prepared by two-step SDC is limited to approximately 18% at present [117], while FDC yields the current record devices [43]. This is most likely related to the fundamentally different underlying crystallization processes. Two-step SDC relies on the infiltration of the organic cation through a pre-crystallized lead halide film [44,118,119]. FDC, on the other hand, exploits the direct nucleation and growth of the perovskite in the

[2] Thin film and solar cell fabrication done by N. Giesbrecht, spatio-temporal PL experiments done by K. Handloser.

presence of the solvent [42,43]. Clearly, a better understanding of the correlation between these crystallization processes and the resulting opto-electronic properties is important for further progress. Here, the opto-electronic properties of MAPI films fabricated via the FDC and the two-step SDC technique are investigated. First, the variation in film morphology and crystal size resulting from the two methods was confirmed using scanning electron microscopy (SEM). The transport properties of the two different stand-alone films were examined based on a time-resolved, contactless photoluminescence (PL) microscopy technique [114, 120]. Films derived from FDC show substantially increased upper values for the diffusion constants as compared to two-step SDC films. Additional analysis of the transport properties via time-of-flight (ToF) studies on individual laterally contacted films also reveal higher charge carrier mobilities for the FDC MAPI films.

5.2 Materials and methods

Methylammonium iodide was prepared following a previously published protocol [39,44]. In short, 24 mL of methylamine solution (33% in ethanol) was diluted using 100 mL of absolute ethanol. Under constant stirring, 10 mL of aqueous hydriodic acid (57 wt%) was added to this solution. After having reacted for one hour at room temperature, the solvents were removed by rotary evaporation. The obtained white solid was washed with dry diethyl ether and recrystallized from ethanol. Lead iodide (99% Sigma) and anhydrous N,N-dimethylformamide (DMF, Sigma) were used as received. A ∼200 nm thick layer of lead iodide was deposited via dynamic spincoating from a 0.85 M PbI_2 solution in DMF at 3000 rpm for 15 s on a standard glass cover substrate. When starting the spincoater, a temperature between 60 and 65 °C is required for both the substrate and the precursor solution [44] to achieve visually smooth films. The immersion solution was prepared by dissolving 9.5 mg/mL methylammonium iodide in anhydrous isopropanol (Sigma) through heating to 60 °C. The spincoated films were then immersed in the heated solution for 8 min while the temperature of the solution was monitored and kept at 60 ± 1 °C for the entire time. Once the conversion was finished, the perovskite films were washed with clean, anhydrous isopropanol (IPA) and dried under a nitrogen stream. The final perovskite film featured an average thickness of ∼325 nm, which was estimated via scanning electron microscopy cross sections. After synthesis, the films were covered with a poly(methyl methacrylate) (PMMA) layer to protect them from degradation through moisture. For this purpose, 50 mg/mL of PMMA in anhydrous chlorobenzene were spincoated at 1000 rpm.

The synthesis procedure for FDC MAPI followed a method published by Xiao and coworkers [42] A solution consisting of PbI_2 (1.25 M, Sigma 99%) and methylammonium iodide (1.25 M) in anhydrous DMF (Sigma) was spin-coated dynamically (at 5000 rpm, total 15 s) onto a glass substrate. Both the solution and the substrate were at room temperature. After 5 s, chlorobenzene (CB) was added on top of the spinning substrate; the film turns brown directly after the chlorobenzene addition and then turns transparent again.

Afterwards, the substrate was placed on a hotplate (100 °C for 10 min) resulting in a dark film that is shiny and reflecting. After the synthesis the films were covered with a PMMA layer to protect the films from degradation by moisture. For this purpose, 50 mg/mL of PMMA in anhydrous CB was spin-coated at 1000 rpm. The fabrication of the solar cell devices based on these films was done according to the procedure described in Chap. 3.

Laterally arranged gold contacts were fabricated in a cleanroom facility via optical lithography (see also Chap. 3). The glass substrates were cleaned with a 2% Hellmanex solution and rinsed with deionized water and isopropanol. After sonication for 5 min in acetone and rinsing with 2-propanol, the substrates were exposed to oxygen plasma for 10 min to remove surface residuals and to facilitate adhesion of the metallic contacts on glass. Using a positive resist in combination with a bonding agent, the structures were created via UV-illumination and developed in an diluted aqueous solution of sodium hydroxide. Before depositing a 10 nm thick layer of TiO_2 and 30 nm of gold via e-beam evaporation under vacuum (10^{-7} mbar), the samples were cleaned with deionized water and dried in a nitrogen flow. The lift-off of residual metal parts from the glass substrate was performed in anhydrous dimethyl sulfoxide (DMSO) at 80 °C. Finally, the coated glass sheets with in-plane distances between 7 and 13 µm were cleaned with 2-propanol. Deposition of the MAPI thin films was done according to the fabrication protocols mentioned above.

5.3 Results and discussion

Two different preparation techniques are used to fabricate the MAPI thin films studied within this work (Fig. 5.1). The first film is synthesized via a two-step deposition protocol [39, 44] starting from a spincoated PbI_2 film that is then immersed in a heated methylammonium iodide (CH_3NH_3I, MAI) solution (Fig. 5.1 a). The resulting MAPI films feature small, connected crystallites of varying size and orientation as can be seen in the SEM cross section in Fig. 5.1c. In the following, these films are referred to as "two-step SDC MAPI". The second type of MAPI films is prepared by a one-step, solvent-induced, fast crystallization-deposition (FDC) method. Here, a N,N-dimethylformamide (DMF) solution of $CH_3NH_3PbI_3$ is spin-coated onto a substrate, immediately followed by the addition of chlorobenzene (CB) [42] to induce crystallization and promote fast nucleation and growth of the crystals in the film (Fig. 5.1 b). As-prepared films (hereinafter termed "FDC MAPI") consist of significantly larger crystalline grain structures arranged in highly uniform layers and result in particularly smooth and continuous films (Fig. 5.1 d and Fig. 5.4 a).
Next, the individual layers of the two films were studied with an optical technique for contactless transport measurements [114]. Fig. 5.2 a shows a schematic illustration of the approach, which is based on time-resolved laser scanning confocal PL microscopy (scheme of the setup shown in Chap. 3). With the help of a piezo-electric mirror in the detection beam path, the detection volume can be raster-scanned relative to a fixed excitation

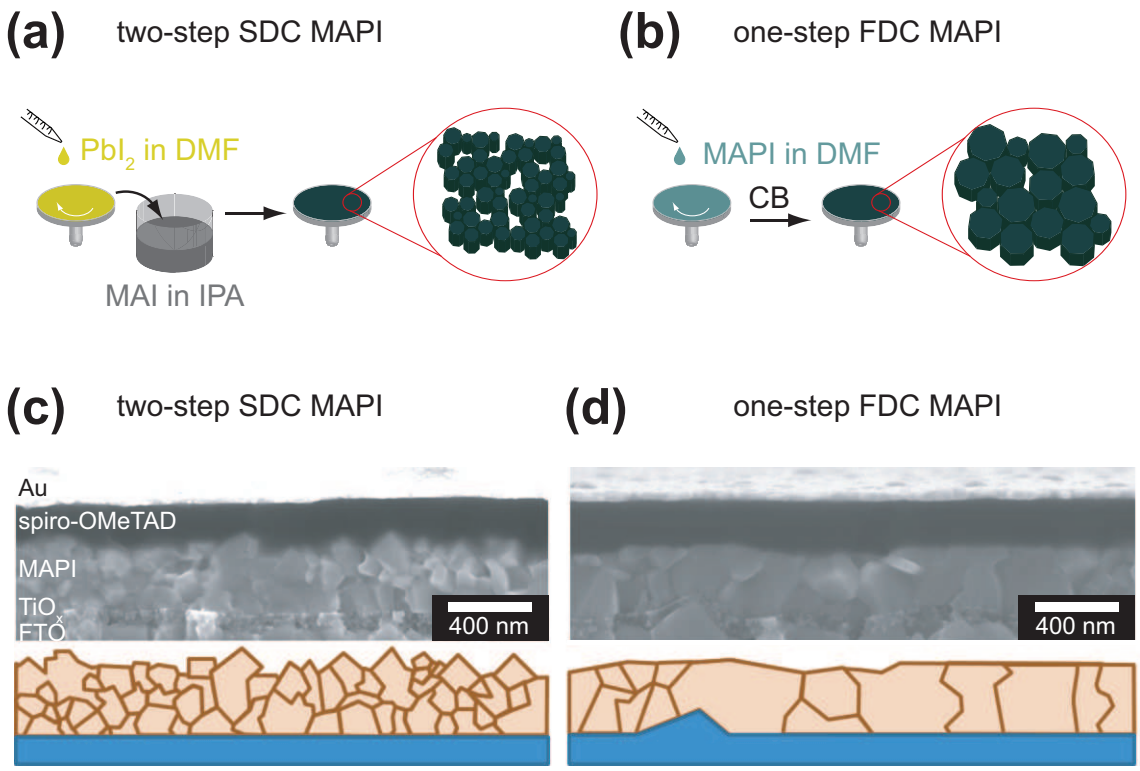

Fig. 5.1 Schematic representation of the fabrication protocols used for the synthesis of the two investigated films and corresponding SEM cross-sections. (a) Films based on the two-step technique start from a spincoated lead iodide film which is immersed into a methylammonium iodide solution. (b) One-step MAPI films are based on a spincoated methylammonium lead iodide solution whereas crystallization is finalized by addition of chlorobenzene. (c) MAPI thin film fabricated via the two-step SDC protocol [44]. The resulting morphology shows small, connected crystallites of varying size and orientation. (d) MAPI thin film synthesized by the FDC method [42]. The latter consists of significantly larger crystallites arranged in a highly uniform structure and result in particularly smooth and continuous films.

volume and sample position. The PL signal that arises from the recombination of photo-excited states is recorded as a measure for carrier density within the film. Charge carrier transport can be observed by exciting the sample at a fixed position (Fig. 5.2 a, green circle) and detecting the PL signal at remote locations (blue circle). With this experimental technique, time-correlated single photon counting (TCSPC) transients are recorded after pulsed excitation at $\lambda = 510$ nm at increasing excitation-detection distances. Because light soaking effects have been observed for perovskite thin films that significantly affect the material properties and characteristics [110–114], the investigated samples were completely pre-soaked prior to all measurements. An examination of the PL transient rise (Fig. 5.2 b) reveals a continuously growing shift of the signal rise to later times for larger separations between the excitation and the detection volume. Charge carrier transport times were extracted from the acquired transients at 50% of the normalized intensity (black dotted line in Fig. 5.2 b). Referencing the observed times for the individual detection positions to the center transient (brown line in Fig. 5.2 b) enables the spatio-temporal examination of

carrier transport within the film. The extracted transport times are displayed in Fig. 5.2 c as a function of transport distance and show significant differences for the two investigated MAPI films.

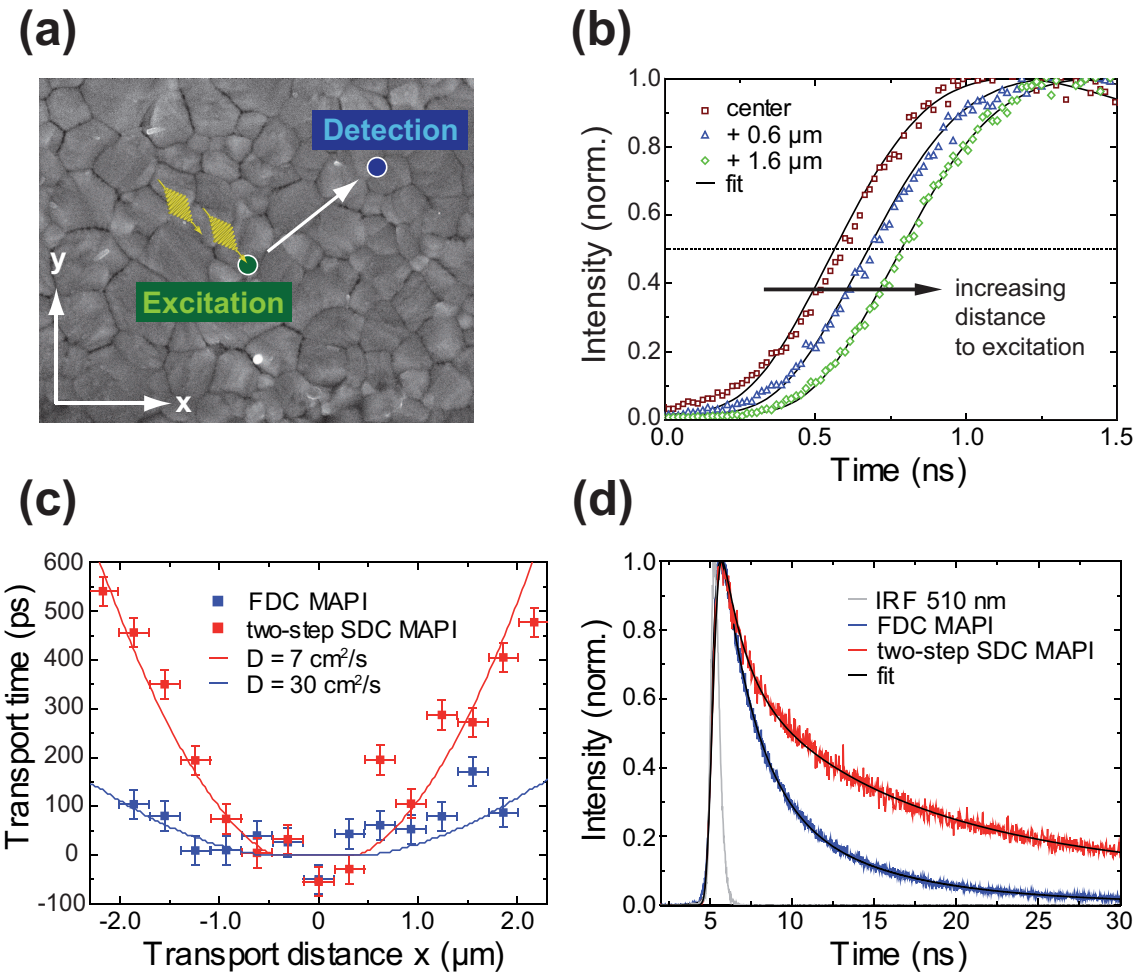

Fig. 5.2 Spatio-temporal investigation of transport via PL microscopy. (a) Schematic illustration of the experimental procedure for contactless transport measurements based on time-resolved remote detection of PL [114]. (b) PL transients recorded after pulsed excitation at $\lambda = 510$ nm at increasing excitation-detection distances. (c) Transport times for carrier transport extracted from the TCSPC transients at 50% rise of the normalized intensity (black dotted line in (b)) and referenced to the center transient (brown curve in (b)). The solid lines represent simulations of the 2D diffusion equation using two diffusion constants $D = 7 \pm 2$ and $D = 30 \pm 10$ cm^2/s for the two-step SDC and FDC MAPI films, respectively. The values are most likely influenced by radiative transport and represent an upper limit (see main text). (d) Acquired PL decays with their corresponding fits (black lines) for the two different MAPI thin films. Films synthesized via the FDC method (blue curve) show a significantly faster decay than the ones prepared by the two-step SDC route (red curve). The grey curve represents the instrument response function (IRF) of the system.

A considerably faster charge carrier transport time of about 25 ps for the first micrometer can be observed for the film that is synthesized via the FDC method, while about 100 ps are obtained for the two-step route. The obtained transport times were modeled by numerical simulation based on the 2D diffusion equation. Within the temporal and spatial

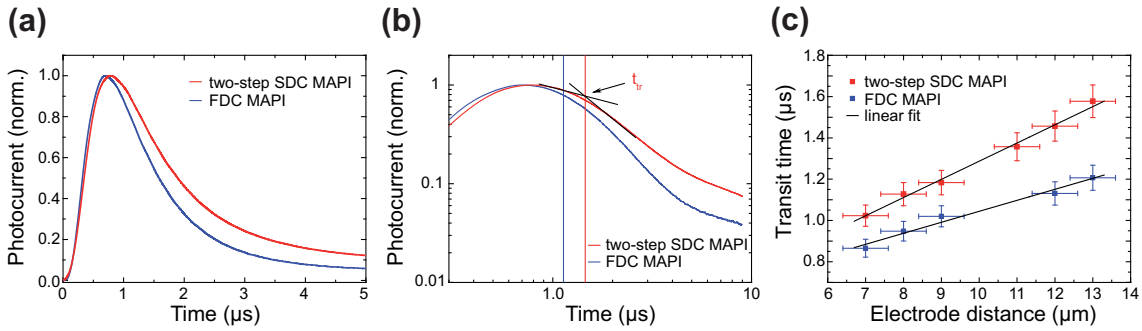

Fig. 5.3 ToF measurements of laterally contacted MAPI thin films with varying distances between the metal electrodes. (a) Example of photocurrent transients recorded for the two different MAPI thin films. (b) The plateau and the decay of the transients are fitted linearly in log-log plots, allowing for the extraction of the transit time t_{tr} from the lines' intersection. With the determined transit time the charge carrier mobility can be calculated as described in Eqn. 5.1. (c) Linear dependence of the extracted transit time on the different electrode distances. Charge carrier mobilities are determined via the slope of the linear fit, leading to a value of $\mu = 2.64 \pm 0.2$ cm^2/Vs for FDC MAPI and $\mu = 1.62 \pm 0.2$ cm^2/Vs for the two-step material.

measurement accuracy of about 30 ps and 0.15 µm (Fig. 5.2 d), the experimental values match the simulation results for a diffusion constant of $D = 30 \pm 10$ cm^2/s in the case of FDC and $D = 7 \pm 2$ cm^2/s for the two-step SDC MAPI film, respectively. Using the measured intensity-averaged PL lifetimes τ for the two MAPI films and the diffusion constants D derived from the transport measurements, the diffusion length can be estimated according to $L_D = \sqrt{D \cdot \tau}$. With the intensity averaged lifetimes $\tau = 15.7$ ns for FDC and $\tau = 38.1$ ns for two-step SDC MAPI films, both values derived from bi-exponential modeling of the transients (Fig. 5.2 d), $L_D = 6.9$ and 5.2 µm, respectively, are obtained. These diffusion lengths are one order of magnitude larger than the film thickness in a typical device, leading to the assumption that the charge carrier collection efficiencies approach unity in both cases.

At this point, it is important to note that radiative transport of PL in terms of waveguiding due to a high refractive index of the films [121–124] and scattering of photons towards the detector cannot be excluded. The here presented transport times and diffusion constants are most likely affected by these processes leading to two contributions (instantaneous signal due to radiative transport and delayed signal arising from diffusive transport) to the measured transients which cannot be resolved individually on the timescale and -length probed by the employed electronics and diffraction-limited microscope. This might also explain the observed shift of the rise of the transients with increasing excitation distance. The modeled diffusion constants hence represent upper value limits whereas the actual numbers are presumably lower and need further investigation and quantification. Furthermore, it is not clear why the intensity averaged lifetimes are higher in the case of SDC MAPI as compared to FDC MAPI. Nonetheless, transport in FDC MAPI could be more efficient than in SDC films because of the improved morphology in terms of a reduced number of recombination sites at grain boundaries.

To complement these findings, the charge carrier transport in individual in-plane contacted films was investigated by time-of-flight (ToF) measurements (description of the employed setup provided in Chap. 3). For these measurements gold contacts were fabricated on glass substrates via optical lithography with varying spacings followed by deposition of the perovskite films on top. The films were biased by a DC electric field and the photocurrent generated after nanosecond pulsed excitation at one of the contacts was measured as a function of time (Fig. 5.3 a). To extract the time the generated charges need to travel to the respective opposite electrode (transit time t_{tr}) from the transients, a fitting routine is employed [79]. In this routine the different slopes of the resulting photocurrent transients are fitted linearly in log-log plots (see Chap. 3) allowing for the extraction of t_{tr} from the lines' intersection (Fig. 5.3 b). Fig. 5.3 c shows the derived transit times t_{tr} at constant applied electrical field ($E = U_{bias}/d = 7$ kV/cm) for the two film types which are seen to linearly scale with the lateral electrode distance. The slope of the transit time ($1/(\mu \cdot E)$) for constant E is used to estimate the charge carrier mobility μ according to [79, 125]

$$\mu = \frac{d}{E \cdot t_{tr}}. \tag{5.1}$$

An enhanced mobility of $\mu = 2.6 \pm 0.2$ cm^2/Vs is obtained for the thin film based on the FDC route, while the two-step synthesis leads to a mobility of $\mu = 1.6 \pm 0.2$ cm^2/Vs.
Comparison of the obtained values to results reported in literature is challenging because most of the applied techniques are contactless and probe a rather local mobility (3 cm^2/Vs to several tens of cm^2/Vs, measured by using TRMC or THz spectroscopy [16, 57–59]). Contacted MAPI films on the other hand reveal values between 0.5 and 8 cm^2/Vs [60–62] when employing FET and Hall mobility measurements. The here described lateral (macroscopic) mobility values describing transport over several grain boundaries are however well within the range of these values.
In the following the two quantities describing the transport characteristics of the films derived from the presented time-resolved PL and ToF experiments are compared. For ambipolar transport ($n_e \approx n_h$) and similar electron and hole mobilities ($\mu_e \approx \mu_h$) the diffusion constant D is proportional to the mobility following the Einstein relation $D = \mu k_B T/q$ [28]. Using the diffusion constants derived above from PL exeriments yields $\mu_{PL} = 1160$ cm^2/Vs and $\mu_{PL} = 271$ cm^2/Vs for FDC and two-step MAPI films, respectively. These values are about up to three orders of magnitude higher than the values determined from the electrical measurements. This difference can probably be attributed to the different microscopic processes studied in the two experiments. The ToF results represent the mobility of charge carriers measured over an extended sample area (several microns) including the contacts at which different electron and hole densities (n_e, n_h) can be present which can influence carrier recombination [28]. The contactless PL experiments, on the other hand, probe the recombination from charge neutral excitons. The higher mobilities derived from the PL experiments could thus indicate a contribution from excitonic transport. Also, the diffusion constants most likely represent upper limits (as described above) which do not

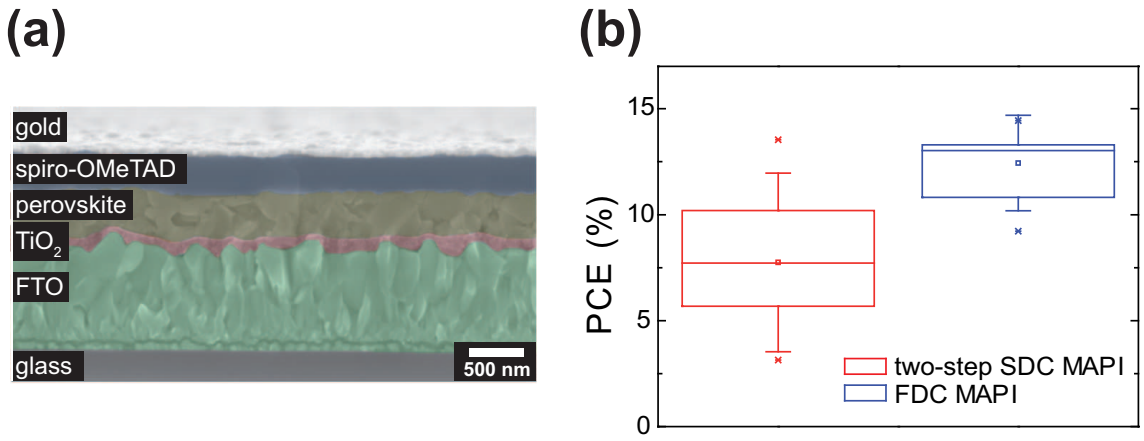

Fig. 5.4 SEM cross section and efficiency statistics for working photovoltaic devices incorporating the two investigated MAPI thin films. (a) SEM cross section of a working photovoltaic cell illustrating the sample architecture. Photovoltaic devices are prepared in a planar configuration using FTO-coated glass substrates (grey and green layer) that are covered with a TiO_2 layer (red), a perovskite thin film (brown), Spiro-OMeTAD (blue) and a gold electrode (white). Scale bar of the SEM image: 500 nm. (b) Power conversion efficiency statistics for MAPI films prepared via the FDC and the two-step deposition protocol considering 27 individual cells. Significantly higher values are obtained for the FDC films reaching an average PCE of 12.4%, while an average of 7.75% is determined for the two-step SDC route.

differentiate between radiative and diffusive transport. Consequently, the mobility values related to the Einstein equation can also be seen as upper limits.
Finally, the performance of devices (SEM cross-section shown in Fig. 5.4 a) fabricated from the two types of films was compared. The FDC derived MAPI films show a significantly improved average PCE of 12.4% as compared to 7.75% in the case of two-step SDC MAPI films (Fig. 5.4 b). From the slope of the J-V curves at open circuit condition the series resistance R_S of the photovoltaic devices can be estimated. For FDC-MAPI based cells the series resistance amounts $R_S = 5.2\ \Omega\text{cm}^2$ and $R_S = 8.4\ \Omega\text{cm}^2$ for cells comprising two-step SDC MAPI. Hence, solar cells incorporating FDC-MAPI with higher film mobility feature higher conductivity and thus lower resistance, which contributes to an increased fill factor and improved solar cell performance (Fig. 5.4 b). Similar observations have already been made in the field of organic photovoltaics where an increase of the mobility is correlated to an enhanced fill factor and PCE of the corresponding solar cell [126–130]. Furthermore, based on the SEM data in Fig. 5.1, the higher PCE and mobility values can be attributed to the optimized morphology with a reduced number of grain boundaries for films prepared via the FDC method.

5.4 Conclusion

In conclusion, the optoelectronic properties of MAPI thin films prepared via two state of the art deposition protocols were compared. Spatio-temporal PL investigations reveal a 3-4 times higher diffusion constant in the FDC derived MAPI films as compared to SDC

MAPI films whereas the obtained values are most likely affected by radiative transport and represent upper limits. In addition, increased charge carrier mobilities in lateral direction for the FDC MAPI thin film were observed which can be assigned to a decreased number of grain boundaries. The improved opto-electronic properties directly translate into the performance of solar cells as devices incorporating FDC derived MAPI feature a substantially higher power conversion efficiency. These results underline that PL lifetime measurements need to be complemented by both optical and optoelectronic transport measurements to foresee and understand the properties of perovskites and the performance characteristics in the corresponding devices.

6 The impact of grain size on charge carrier mobility in MAPI systems

6.1 Motivation

As seen in the previous chapters, the optoelectronic properties of hybrid perovskite thin films strongly depend on the fabrication technique and could thus be optimized further. Film quality in terms of morphology, crystallinity and energetic disorder are crucial parameters determining efficient charge transport. Extrinsic factors such as grain boundaries or impurities heavily affect charge carrier mobility in the films because they represent potential recombination sites [131] and have to be avoided as far as controllable via careful choice of the processing strategy.

Therefore, it is important to investigate charge carrier mobilities of perovskites in systems where the number of grain boundaries as extrinsic effect is expected to be reduced as it is the case for largely sized crystals. ToF measurements on perovskite crystals in the millimeter range should hence allow to estimate an upper mobility limit in the material that can be reached when extrinsic effects affecting charge transport are minimized.

By knowing this intrinsic mobility limit, an explanation to another striking question that is being intensely investigated might be found: diffusion constants D and diffusion lengths L_D obtained from numerous measurements [15, 47, 53, 114] in perovskite thin films do not result in the experimentally determined mobility values when applying Eqn. 2.9 (see Chap. 2), although in the case of MAPI the assumptions of the Einstein relation seem to be fulfilled (ambipolar mobility, presumably non-doped intrinsic semiconductor [132,133]). Nonetheless, the observed mobilities are up to two orders of magnitude lower as compared to the expected values. Furthermore, comparison with the typical direct inorganic semiconductor GaAs, similar with respect to bimolecular recombination rate and diffusion length of charge carriers [134, 135], also leads to some discrepancy since the latter reveals only slightly lower effective masses for electrons in the conduction band and holes in the valence band, but nonetheless significantly higher mobility values.

To this end, millimeter-sized MAPI crystals were investigated with respect to their hole and electron mobilities via the ToF technique. The direct comparison of the values obtained in the comparatively large crystal with experiments on laterally contacted MAPI thin films comprising different grain sizes underlines the substantial effect of grain size on charge carrier mobilities, resulting in differences of factor 10 to 100.

6.2 Materials and methods

Methylammonium lead iodide crystals in the size range of a few millimeters were grown in the group of Prof. Dyakonov (JMU Würzburg) via inverse temperature crystallization, following a previously published procedure [136]. The dark and shiny crystals were contacted via commercially available copper wires, fixed onto two parallel facets with carbon containing conductive wire glue. After waiting for 10 minutes, the contacted crystals were fixed on a glass slide to enhance mechanical stability of the investigated system and to avoid moisture-induced degradation. This was done by encapsulating the crystals with a few droplets of UV glue which was dried for 1-2 minutes under a UV lamp. A schematic of the respective sample layout is shown in Fig. 6.1 a. The samples were investigated using the ToF setup described in Chap. 3 by illuminating the crystal close to the contact through which the electric field was applied.

6.3 Results and discussion

Time-of-flight experiments upon pulsed laser excitation at 540 nm (see also Chap. 3) were performed at different external voltage values to identify charge carrier mobilities because thickness variation of the crystals is hard to achieve. The obtained photocurrent transients driven by locally photogenerated holes (electrons are immediately extracted at the front contact) are shown in Fig. 6.1 b and directly reflect the increased applied voltage. Switching the polarity of the DC field changes the type of charge carriers contributing to the recorded *j*-*t* profile, whereas a direct comparison of the two different types of charge carriers is shown in Fig. 6.1 c. Electrons hence seem to move slightly faster through the crystal under an external field due to narrowing of the observed current profile as compared to the transient obtained for holes.
Plotting the ToF transients in a double logarithmic scale enables the determination of the transit time t_{tr} from the point of intersection of two linear fits, as already shown in the previous chapters. Following the mobility equation

$$\mu = \frac{d^2}{U_{bias} \cdot t_{tr}} = \frac{1}{E} \cdot \frac{d}{t_{tr}} \tag{6.1}$$

the slope of the linear regression relating the transit times extracted from Fig. 6.1 b as a function of the reciprocal value of the electric field gives the mobility of the holes (Fig. 6.1 d, red squares). By performing the same voltage series as in Fig. 6.1 c under inverted polarity, a set of transients is obtained that allows for the determination of electron mobility (Fig. 6.1 d, blue squares). The mobility values are very similar, 119 ± 9 cm^2/Vs for holes and 130 ± 6 cm^2/Vs for electrons, suggesting comparatively balanced charge transport. Reports of other groups performing mobility measurements on single crystals comprise values between 24 (ToF) and 164 cm^2/Vs (space-charge limited current technique, SCLC) [137] for holes and from 67 cm^2/Vs (SCLC) [136] up to 115 cm^2/Vs (TRMC) for the sum of hole and electron [138]. In principle, the experimentally derived values from

ToF are well within this range, nonetheless, a comparison between these values should be treated with care since extrinsic factors such as contact material or the availability of probed carriers (photoinduced or injected) might contribute strongly to the observed experimental results. Furthermore, all available mobility techniques are sensitive on different length scales (microscopic vs. macroscopic) which renders direct comparison of the values challenging.

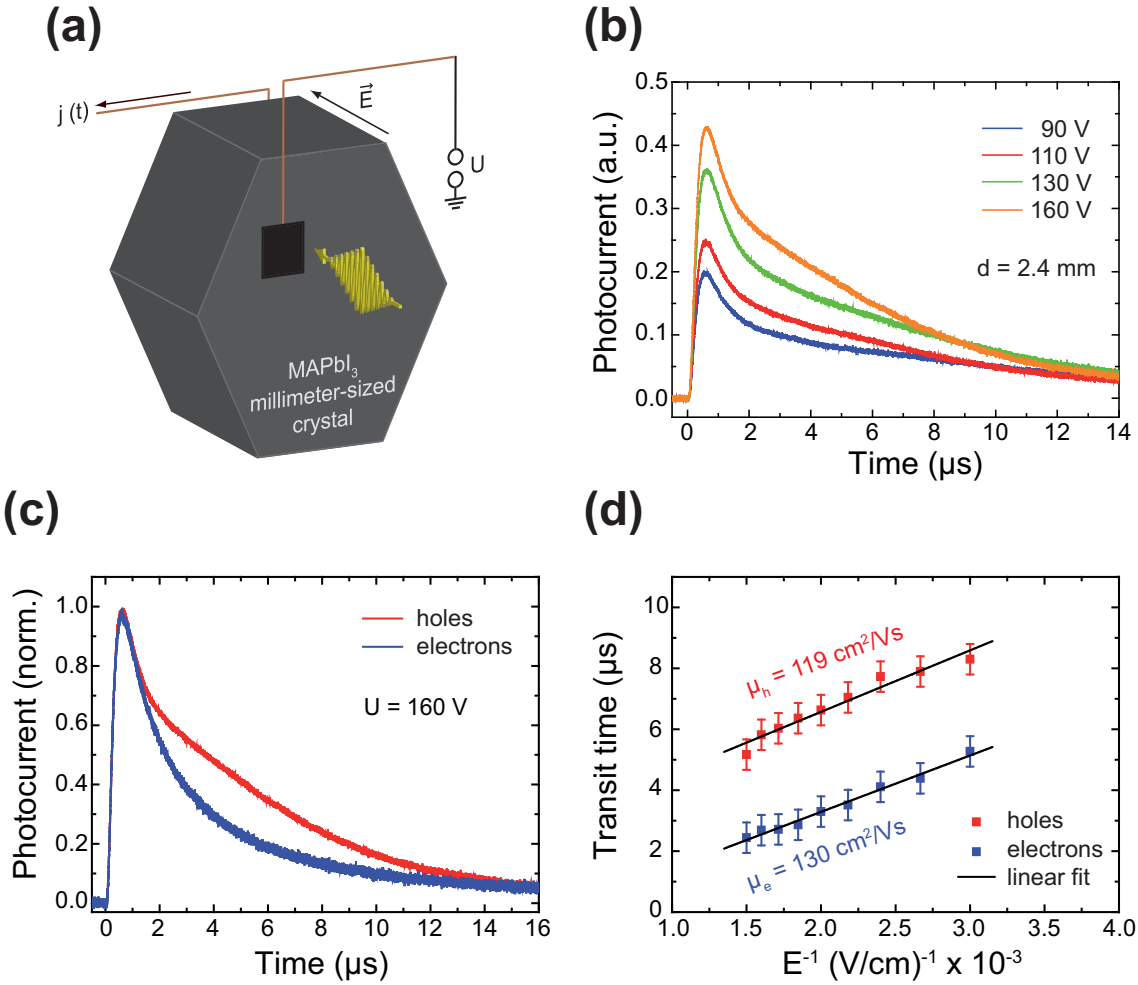

Fig. 6.1 Characterization of the millimeter-sized MAPI crystal via ToF. (a) Schematic of the experimental configuration. The crystal is contacted via metallic wires which are fixed on two parallel facets. (b) Representative current-time profiles for different bias voltages applied to the crystal. The expected kink, typically expected for non-dispersive transport (see Chap. 3), is smeared out indicating dispersive charge transport. (c) Extracted transit times as a function of the reciprocal voltage value. The values correlate linearly, whereas the slope of the fit function is used to calculate the mobilities of holes and electrons.

To gain further information on extrinsic effects affecting the charge carrier mobility in hybrid perovskites and the upper limit of reachable values, their experimental determination may be performed by using the identical technique (ToF) for films with different grain sizes derived from several processing techniques. The respective mobilities extracted

Tab. 6.1 Comparison of mobility values for MAPI films comprising differently sized grains with millimeter-sized MAPI crystal.

Crystal size	Fabrication protocol	Charge carrier mobility
	fast-crystallization deposition	$\mu_h = 6 \pm 1$ cm^2/Vs
$\sim$ 500 nm	with DMF/DMSO & CB	$\mu_e = 6 \pm 1$ cm^2/Vs
	(based on [42])	$\boldsymbol{\mu_{sum} = 12 \pm 2}$ **cm^2/Vs**
	controlled solvent drying	$\mu_h = 8 \pm 1$ cm^2/Vs
$\sim$ 1 µm	with DMF	$\mu_e = 9 \pm 1$ cm^2/Vs
	(adapted from [139])	$\boldsymbol{\mu_{sum} = 17 \pm 2}$ **cm^2/Vs**
	controlled solvent drying	$\mu_h = 12 \pm 1$ cm^2/Vs
$>$ 3 µm	with DMF/DMSO	$\mu_e = 13 \pm 1$ cm^2/Vs
	(adapted from [139])	$\boldsymbol{\mu_{sum} = 25 \pm 2}$ **cm^2/Vs**
	controlled solvent drying	$\mu_h = 15 \pm 1$ cm^2/Vs
$>$ 10 µm	with DMF/THTO	$\mu_e = 17 \pm 1$ cm^2/Vs
	(based on [140])	$\boldsymbol{\mu_{sum} = 32 \pm 2}$ **cm^2/Vs**
	inverse temp. crystallization	$\mu_h = 119 \pm 9$ cm^2/Vs
$\sim$ 2.4 mm	with GBL	$\mu_e = 130 \pm 6$ cm^2/Vs
	(based on [136])	$\boldsymbol{\mu_{sum} = 249 \pm 15}$ **cm^2/Vs**

for a series of laterally contacted films with varying crystallite sizes are listed in Tab. 6.1 together with the values determined for the millimeter-sized MAPI crystal.
Clearly, the grain size correlates to the ToF-mobilities. The larger the crystals become due to a modified and adapted fabrication protocol (see Fig. 6.2 a-d), the higher is the mobility for both holes and electrons probed on a micrometer scale. This can be assigned to a subsequent reduction of grain boundary density and hence to a reduction of sites where charges can potentially recombine. Furthermore, larger crystals tend to be more defect-free which is also beneficial for charge transport [131]. The comparison of thin films with the millimeter-sized crystal reveals that the highest mobilities can be achieved in the latter, but on the other hand the shape of the transients does not indicate non-dispersive transport which leads to the assumption that the herein investigated millimeter-sized crystal might have a reduced number of material defects with respect to solution-processed thin films with the same composition, but is most likely not entirely defect-free to be denominated as single crystalline.
Besides extrinsic effects, intrinsic effects are said to be present as well in perovskites. These effects could be responsible for the large mismatch between experimentally determined and theoretically expected mobilities derived either from charge carrier diffusion lengths

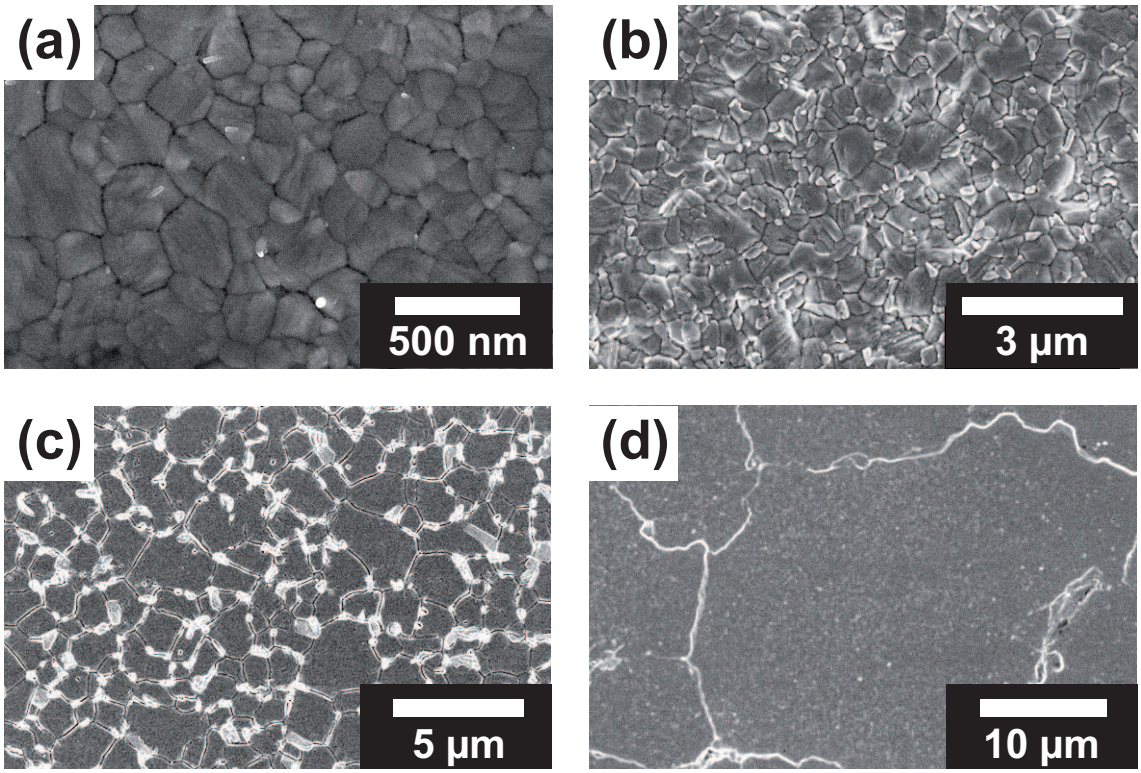

Fig. 6.2 SEM top views of MAPI thin films comprising different crystal sizes and grain boundary densities: (a) crystal size ∼ 500 nm, (b) ∼ 1 µm, (c) > 3 µm and (d) > 10 µm, as indicated in Tab. 6.1.

or from the comparison with the inorganic GaAs which exhibits a similar effective mass of electrons m_e^* and holes m_h^* but a substantially different mobility of more than 1000 cm^2/Vs [141] which can be calculated from

$$\mu = \frac{e\tau}{m^*}. \tag{6.2}$$

where τ is the momentum relaxation time.

Fundamental limitations to charge carrier mobility in MAPI could arise from higher electron-phonon coupling since the momentum scattering times have to be smaller than 10 fs for mobilities below 100 cm^2/Vs. The required momentum scattering time is hence substantially shorter than the one observed in GaAs (several hundreds of fs) [131]. From the Drude model, the temperature dependence of charge carrier mobility (power law $\mu \propto T^{-3/2}$), confirmed by several groups [54, 55, 59, 109], might be described by deformation potential scattering. Due to a large number of atoms per unit cell, many phonon modes and dynamic disorder in MAPI, currently published experimental results suggest rather polar scattering in terms of Fröhlich interactions being the intrinsic limiting factor of mobility [142]. With this model describing long-ranged electric fields generated by out-of-phase atomic displacements as major contributor to electron-phonon coupling, the theoretically predicted charge carrier mobility (μ_e = 133 cm^2/Vs and μ_h= 94 cm^2/Vs, 300 K) and temperature trend fit the experimental results in single crystals quite well [143]. Con-

sidering polar scattering, the discrepancy between the mobility in MAPI and the mobility in GaAs can easily be understood, since the higher ionicity of the Pb-X bond, the low-energy phonon modes and slightly larger effective masses of hole and electron directly translate to a lower charge carrier mobility in hybrid perovskites [131, 144]. A polaronic description in terms of self-trapping of an electron in the ionic lattice generating the electric field for Fröhlich interactions has also been suggested as the origin for the modest mobility values due to the associated increase in effective masses m_e^* and m_h^* [145]. The polaron-related temperature-activated hopping transport at high temperatures hasn't been observed though, so that experimental evidence of this model applied to MAPI is still lacking [131, 144].
Generally, intrinsic limitations arising from whatever scattering processes could most likely also be the reason for the apparent mismatch between limited mobility and high diffusion constant and long carrier lifetime since diffusion is limited by other mechanisms than drift. This might be a possible explanation for the violation of the Einstein relation $D = \mu k_B T/q$ (see Chap. 2) in metal halide perovskites [28, 146].

6.4 Conclusion

In this chapter, the ToF-derived mobility of a millimeter-sized MAPI crystal has been compared to the mobilities of different MAPI thin films, each one consisting of differently sized grains. It could be observed that the large crystal reveals substantially larger electron and hole mobilities as compared to the values in the films, whereas the mobilities in the latter are strongly affected by the grain size. This trend is most likely to a reduction of grain boundaries that charge carriers have to overcome when moving across the material and can be seen as extrinsic factor limiting mobility which could potentially be minimized by adapting the fabrication technique. Intrinsic factors limiting the mobility on the other hand are largely discussed in literature and are seen to be the origin of the mismatch between the experimentally derived modest mobilities and the theoretically expected ones in MAPI systems. Nonetheless, high charge carrier mobilities are not absolutely mandatory for high-performance photovoltaic devices, but rather an adequate mobility that allows extraction of photogenerated charges before losses due to recombination occur [147].

7 Control of perovskite crystal growth by methylammonium lead chloride templating

State-of-the-art solar cells based on methylammonium lead iodide ($MAPbI_3$) now reach efficiencies over 22%. This fast improvement was possible with intensive research in the perovskite processing. In particular, chloride based precursors are known to have a positive influence on the crystallization of the perovskite. In this chapter, which is based on the publication **Control of perovskite crystal growth by methylammonium lead chloride templating** [116], a combination of in-situ X-ray diffraction and charge transport measurements is used to understand the influence of chloride during the perovskite crystallization in planar heterojunction solar cells.[3] $MAPbCl_3$ crystallizes directly after the deposition of the starting solution and acts as a template for the formation of $MAPbI_3$. Additionally, the charge carrier mobility doubles by extending the time frame for the template formation. These results give a deeper understanding of the influence of chloride in the synthesis of $MAPbI_3$ and illustrate the importance of carefully controlling crystallization for reproducible, high efficiency solar cells.

7.1 Motivation

With rising global energy demand and the decline of fossil fuels reserves, there is a great need to develop renewable energy resources. Lately, solar cells based on organic-inorganic trihalide perovskites, e.g. $CH_3NH_3PbI_3$, have emerged as a highly efficient and inexpensive photovoltaic technology [40, 41, 148, 149]. Through optimization of the fabrication processes [42,150,151], the annealing process [152,153] and the interfaces [111], perovskite solar cells have already exceeded 22% power conversion efficiency (PCE) [10]. Recently, several novel crystallization methods have been exploited to fabricate perovskite photovoltaic devices with high and reproducible performance [51, 154]. In particular, previous studies show that control of the macroscopic morphology and the crystalline domain size has a strong influence on the resulting device performance [155–157]. Hence, understanding the crystallization mechanism of the active layer is a crucial factor. In grain boundaries and defects, traps for the photoexcited species are located and recombination can occur [158]. Thus, a good strategy to maximize device efficiency is the reduction of the number of grain boundaries in the perovskite layer by tuning the deposition technique [52]. A common approach to improve the performance of perovskite solar cells is the use of a chloride based precursor in the casting solution. In particular, lead chloride ($PbCl_2$) and

[3] Solar cell fabrication and in-situ XRD analysis done by A. Binek.

methylammonium iodide (MAI) mixtures lead to highly efficient devices when employed in planar heterojunction solar cells [159]. This enhancement is generally attributed to the formation of bigger crystal domains of the perovskite compared to other precursors and the related reduction of grain boundaries and defects in the bulk material [157]. However, the role of chloride during the crystallization process is still unclear, with many groups reporting no or only small amounts of chloride in the final structure [44, 160–162]. Thus, understanding the crystallization mechanism, and therefore gaining additional handles to tune the crystal morphology of these systems can open up new strategies to maximize the device performance. In the following, the crystallization of the perovskite immediately after deposition is investigated in order to understand and control the crystallization kinetics of the system. In-situ X-ray diffraction measurements show that initially $MAPbCl_3$ crystallizes on the substrate, to be fully converted into $MAPbI_3$ after a certain time under heating. Furthermore, the positive influence of the slow evaporation of the solvent on the crystal size, morphology and also on the charge carrier mobility in the perovskite layer is shown. These results help to understand the influence of chloride during the crystallization process of the perovskite and the origin of the improved performance of the system.

7.2 Materials and methods

The MAPbI3 samples were prepared according to the synthesis route of Eperon and coworkers [152]. In short, a mixture of lead chloride ($PbCl_2$) and methylammonium iodide (MAI) is dissolved at a ratio of 1:3, and is then spin-coated on a TiO_2 covered fluorine-doped tin oxide (FTO) substrate. Afterwards, the sample was kept at room temperature (RT) for different times to allow for the slow evaporation of the residual solvent, and then heated up to different temperatures to complete the conversion to the $MAPbI_3$ crystal phase. With this procedure, slow formation of the perovskite was enabled, leading to uniform crystallites. Solar cell fabrication was done following the procedure described in Chap. 3.

7.3 Results and discussion

To examine the influence of different evaporation times of the solvent at RT on the perovskite morphology, cross-sections were prepared (Fig. 7.1). Short exposure times between 1 min and 20 min resulted in crystallites that are not uniform in size and shape, and a large number of grain boundaries are visible. In contrast, the SEM images of samples with a longer crystallization time show bigger and more uniform crystallites, and consequently a reduction of grain boundary density. To substantiate the uniformity of the $MAPbI_3$ crystals, smooth cross sections showing high contrast were also prepared with a focused ion beam (FIB). In the FIB cross-sections (Fig. 7.1 b) the noticeable difference between fast and slow evaporation of the solvent is even more visible. The 5 min sample exhibits

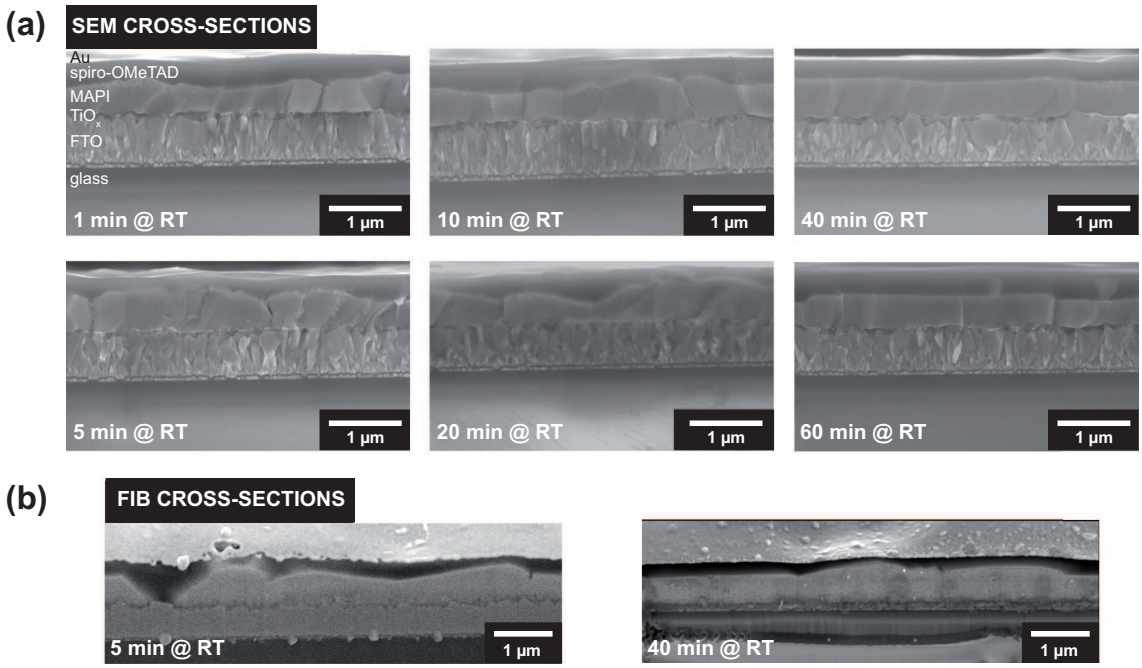

Fig. 7.1 Scanning electron micrographs of MAPI-based solar cells. (a) SEM images of cross-sections of samples with different evaporation times at RT. (b) SEM images of FIB cross-sections of a 5 min and a 40 min sample, respectively.

a rough surface due to non-uniform crystal formation. In comparison, the 40 min sample shows a regular brick-like morphology of the perovskite on the substrate.
In order to further understand the crystallization and the influence of the different temperature treatments during the synthesis, in-situ X-ray diffraction measurements (XRD) were performed under a nitrogen atmosphere with freshly spin-coated samples. Additionally, the effect of heating steps on the perovskite crystal structure was investigated; such steps are often used to achieve highly efficient devices for a range of exposure times (Fig. 7.2). In the first XRD pattern, after 5 min at RT, an intense reflection at around 16° 2θ is observed. Over time, an additional reflection at 14° 2θ appears and slowly increases at RT. The first reflection at higher angles (16° 2θ) is attributed to the (200) plane of the $MAPbCl_3$ perovskite structure, while the second reflection (14° 2θ) is attributed to the (002) plane of $MAPbI_3$ (Fig. 7.2 d); no shift is present in either reflection, therefore ruling out $MAPbI_{3-x}Cl_x$ mixed phases. The broad reflection between 11.2 and 12.6° 2θ is likely the result of the formation of $PbI_{n(2-n)}$ complexes, which arise as a result of employing non-stoichiometric perovskite mixtures with an excess of the organic cation [163]. The difference between both structures is not only the halide, but also the arrangement of the PbX_6 octahedra. Heating to 90°C leads to a reversal of reflection intensity of both perovskite structures, and thus conversion from one structure to the other. Thereby, the intensity of $MAPbCl_3$ is quickly decreased while the reflection of $MAPbI_3$ gains in intensity. Furthermore, the second reflection of the iodide perovskite at around 28° 2θ also increases during the heat treatment. In the following two temperature steps (Fig. 7.2 c), the intensity of $MAPbCl_3$ reflections is further decreased and the orientation of the

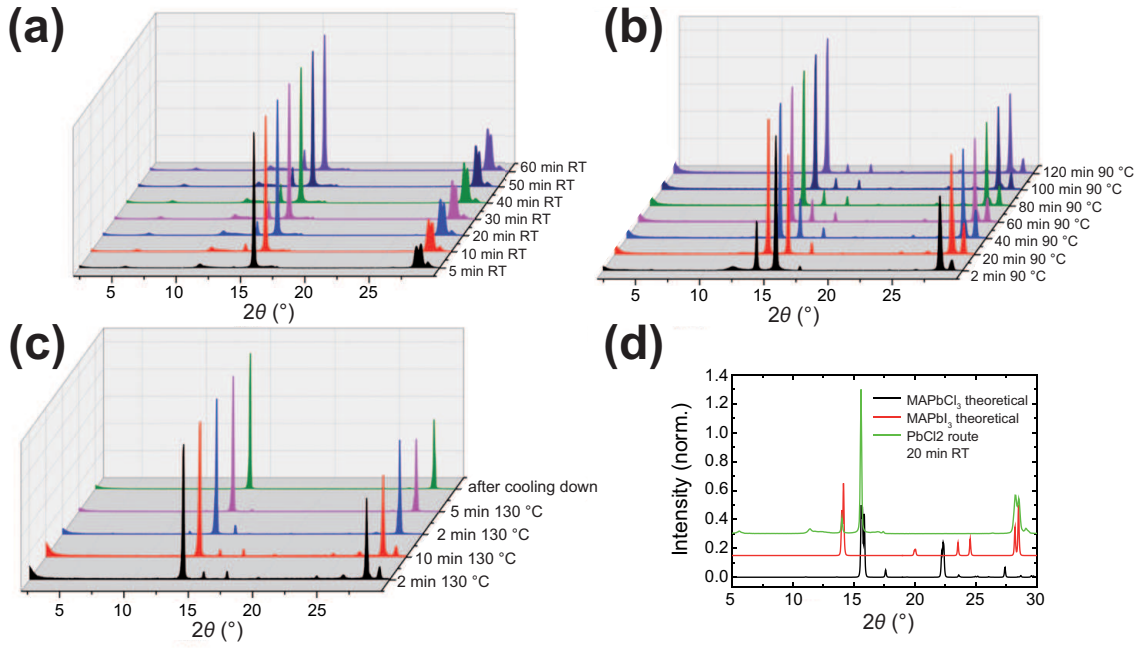

Fig. 7.2 In-situ X-ray diffraction measurements with samples prepared according to the $PbCl_2$ route. (a) shows XRD patterns for the RT step from 5 min to 60 min, (b) 90°C step from 2 min to 120 min and (c) 100°C / 130°C at different times and after cooling down the substrate. (d) Theoretical patterns of $MAPbI_3$ and $MAPbCl_3$ compared with XRD pattern of the sample after 20 min at RT.

$MAPbI_3$ crystals is enhanced as the number of reflections is reduced and only symmetric reflections arising from the c-axis remain. After cooling down to RT, only two reflections are observed, indexed as (001) and (002) from $MAPbI_3$, indicating that the crystals exhibit a preferred orientation along the c-axis and therefore parallel to the substrate. From a crystallographic point of view the samples are very similar, however, the cross-sections show different morphologies. Crystallization of a material from a solution can occur by cooling down the solution or through evaporation of the solvent [164]. In the case of the one-step synthesis route for $MAPbI_3$, supersaturation is induced by evaporating the solvent. This is achieved through spinning of the substrate, which then leads to the formation of the nuclei. Afterwards, the crystallites grow due to the heating of the substrate. The fact that chloride, which improves the crystal quality of the perovskite [103], is not incorporated into the structure of $MAPbI_3$, indicates that its effect must take place during the crystallization process.

The crystallization order of the two perovskite structures can be explained with the Ostwald-Volmer rule, which states that the system with the lower density crystallizes first [165]. Here, the density of $MAPbCl_3$ [166] was estimated as 1.576 g/cm^3, while a value of 4.119 g/cm^3 was obtained for the $MAPbI_3$ [167] compound, and therefore the chloride-containing material is expected to crystallize first, as observed experimentally. A schematic of the proposed mechanism is shown in Fig. 7.3.

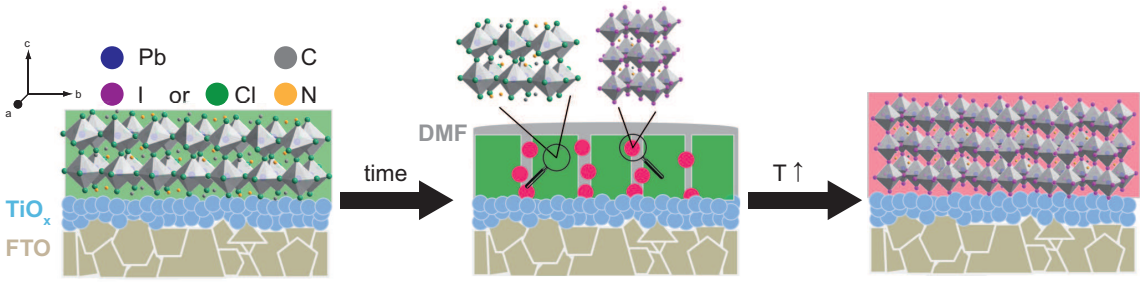

Fig. 7.3 Schematic mechanism of the crystallization of the $MAPbI_3$ perovskite based on the $PbCl_2$ synthesis route in accordance with the Ostwald-Volmer rule.

Here, the sample is left at RT for the slow evaporation of the solvent, where $MAPbCl_3$ forms on the surface and acts as a template for $MAPbI_3$. Additionally, some crystallites of $MAPbI_3$ emerged during the RT treatment as observed in the in-situ XRD. These can then act as seeds for the formation of the $MAPbI_3$ layer while heating up the reaction. Over time, the solvent as well as the excess of MA and chloride are evaporated and highly oriented $MAPbI_3$ crystals are formed on the surface of the substrate with the pre-set orientation from the $MAPbCl_3$ template. With this crystallization mechanism, the morphological differences in the SEM cross-sections can be explained with the time required by the $MAPbCl_3$ template to form on the surface. A short time of 5 min at RT appears to be insufficient to create an oriented and fully formed $MAPbCl_3$ template. Therefore, in this case the deposition of $MAPbI_3$ during the heat treatment leads to less uniform and smaller crystals.

The difference between samples treated for 5 min and 40 min at room temperature was further investigated by incorporating the resulting perovskite layers in a planar heterojunction photovoltaic device architecture with TiO_2 and spiro-OMeTAD serving as the charge extraction contacts [168]. The current-voltage curves and the efficiency distributions of the devices are displayed in Fig. 7.4 a and b, respectively. The film treated for 40 min at RT exhibits enhanced PCE values in comparison to the film treated for 5 min at RT. This difference can be attributed to the higher crystallinity and more uniform size distribution of crystals within the film during the $MAPbCl_3$ template-assisted growth process, as illustrated by the in-situ XRD measurements depicted in Fig. 7.2 a-d. In the SEM top-view of both films it is observed that the domain sizes of the perovskite crystals are increased while the surface density of pinholes is decreased for the film treated for 40 min at RT as compared to the film treated for 5 min, leading to enhanced PCE and reduced hysteresis of the device [157]. Additionally, the greater number of pinholes present in the film treated for 5 min at RT also result in a small open circuit loss due to higher recombination losses, similar to previous results in literature [152].

In order to investigate the relationship between crystal quality and transport dynamics in these solar cells, time-of-flight (ToF) studies were carried out for the devices fabricated from perovskite films treated for 5 and 40 min at room temperature. ToF is a well-established method to extract the mobility of charge carriers in semiconductors and solar

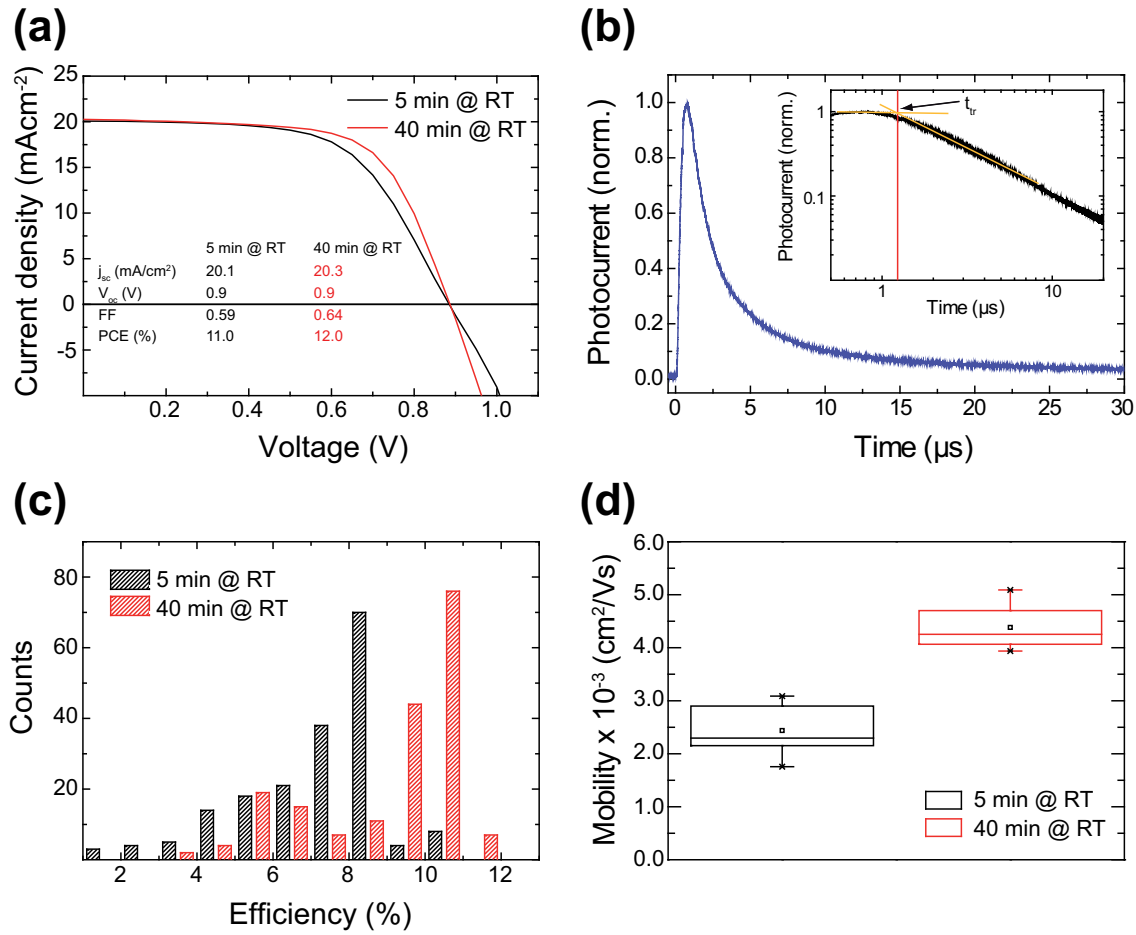

Fig. 7.4 Electrical characterization of MAPI-based solar cells. (a) J-V characteristics of $MAPbI_3$-based solar cell devices prepared with 5 min and 40 min evaporation time at RT. (b) Corresponding distribution of efficiencies from 200 solar cells. (c) Representative ToF transient obtained upon pulsed laser excitation. The inset is a double logarithmic zoom in of the region used to fit the data (see Chap. 3) to obtain the transit time t_{tr} (see text). (d) Respective mobilities obtained by ToF measurements of both sample types. Here it is observed that the incorporation of the material treated for 40 min at RT in the solar cell leads to an increase of charge carrier mobility by a factor of 2.

cells. Based on the generation of charge carriers by short laser pulses and subsequent drifting due to an applied bias, the resulting time-resolved photocurrent is used for the determination of the corresponding mobility (see also Chap. 3) [78]. A representative ToF transient is depicted in Fig. 7.4 c. From this transient, the transit time t_{tr} is obtained. The time resolution of the system is approximately 2 ns, allowing for the extraction of thin film mobilities after weak excitation following the equation:

$$\mu = \frac{d^2}{U_{bias} \cdot t_{tr}}. \tag{7.1}$$

Here, d is the active layer thickness and U the applied bias voltage. In the current device structure, hole transport is predominantly measured, as most charges are generated in close proximity to the electron collection layer (TiO_2), while the holes must travel throughout

the whole length of the film. Note that the resulting ToF transient characteristics in a thin film device fabricated for supporting electron transport, for instance by using PEDOT:PSS and PCBM, would lead to similar results, since electron and hole mobility in MAPI thin films have been shown to be similar [56]. Further, the penetration depth of light in MAPI thin films at 550 nm is 0.66 µm as measured by Park [96]. The resulting experimental observations can be found in Fig. 7.4 d, whereas the experimental error is mainly caused by the determination of the layer thickness. The slow evaporation of the solvent and the associated formation of uniform and big crystals of the perovskite for the 40 min at RT sample can be connected to the enhancement of the mobility of the charge carriers within the photoactive layer as observed in the ToF measurements. The higher mobility in the 40 min at RT sample is also observable in the J/V characteristic since the series resistance of the solar cell is lowered, which leads to a higher fill factor (FF). The series resistance was estimated by fitting the ohmic regime of the J/V curve and yields 12.5 Ωcm^2 for the 5 min and 8.2 Ωcm^2 for the 40 min device. With this increased conductivity of the sample, the charge extraction by the selective contacts is enhanced, resulting in higher device efficiency. The results presented here show mobility values two orders of magnitude higher than previous ToF studies on perovskite solar cells [169]. Note that the morphology of the perovskite plays an important role for the mobility, as demonstrated here, and thus it can be expected that the much smaller crystals and thus higher grain boundary density present in the previous study account for the discrepancy. On the other hand, values obtained from THz (8.1 cm^2/Vs) [16] and microwave (6.2 cm^2/Vs) [109] conductivity measurements on the active perovskite layer only are up to three orders of magnitude higher than the presented results that have been obtained for complete devices. These differences can be attributed to the different transport processes and probing dimensions associated with THz and microwave measurements, in comparison with the complete through-layer transport probed with ToF methods. Moreover, as the ToF measurement probes the entire device, there is as well an influence of the transport layer (spiro-OMeTAD) and the according interfaces on the apparent mobility of the material.

7.4 Conclusion

In summary, the crystallization of $MAPbI_3$ based on a one-step approach with a chloride-based precursor was studied. Based on in-situ XRD measurements, a crystallization mechanism for the synthesis procedure was proposed. Thereby, $MAPbCl_3$ is assembled on the substrate during the slow evaporation of the solvent, and over time some $MAPbI_3$ crystals are also formed. While heating up the substrate, $MAPbI_3$ grows at the expense of $MAPbCl_3$, which leads to crystals oriented parallel to the substrate. Furthermore, a slow evaporation of the solvent during the formation of the $MAPbCl_3$ template influences the morphology, size and uniformity of the resulting $MAPbI_3$ crystals. Advanced electro-optical characterization by time-of-flight studies in this chapter showed that the charge carrier mobility is doubled for devices based on $MAPbI_3$ that were fabricated with

more controlled evaporation of the solvent at RT. This indicates that slow evaporation of the solvent before the heat treatment benefits the solar cell efficiency through enhanced conductivity and a corresponding increased device performance.

8 Charge transport limitations in perovskite solar cells: The effect of charge extraction layers

Understanding the charge transport characteristics and their limiting factors in organo-lead halide perovskites is of great importance for the development of competitive and economically advantageous photovoltaic systems derived from these materials. In this chapter the charge carrier mobilities in $CH_3NH_3PbI_3$ (MAPI) thin films obtained from a one-step synthesis procedure and in planar n-i-p devices based on these films are examined. By performing time-of-flight measurements, mobilities around 6 cm^2/Vs for electrons and holes are found in MAPI thin films, whereas in working solar cells the respective mobility values are reduced by three orders of magnitude. From complementary experiments on devices with varying thicknesses of electron and hole transport layers the charge extraction layers and the associated interfaces rather than the perovskite material itself are identified as the major limiting factors of the charge carrier transport time in working devices. The here presented results are based on the publication **Charge transport limitations in perovskite solar cells: The effect of charge extraction layers** [170].[4]

8.1 Motivation

Hybrid organometal halide perovskites, a class of materials revealing outstanding opto-electronic properties including large absorption coefficients [96] and easily tunable band gaps [97], have undergone a rapid development [11,96] toward particularly promising candidates for integration into photovoltaic devices [74,75]. Facile solution processing at low temperature and the use of cheap and abundant precursor compounds [44,102] combined with power conversion efficiencies surpassing 21% [48] make organic-inorganic perovskites competitive with modern technologies, for example CIGS or silicon [10]. Among a variety of possible material combinations and device architectures [154,171], the state-of-the-art layout for planar n-i-p perovskite solar cells comprises the small organic molecule spiro-OMeTAD as the hole transporter and compact TiO_x as the hole blocking layer [92]. However, these charge extraction materials can introduce some challenging issues to the stacked system. Spiro-OMeTAD for instance is known to be unstable and suffers from degradation processes [172,173] whereas TiO_x has been suggested to contribute to the hysteretic J-V behavior [174,175]. Thus, the examination of the physical processes determining and limiting the charge transport properties is essential to balance material suitability (in terms of stability or production costs) and optoelectronic performance, both being key aspects

[4] Thin film and solar cell preparation done by M. F. Aygüler (group of Dr. Docampo).

on the way toward further development of high-efficiency solar cells.
In this work, a detailed study of the charge carrier mobilities, playing an important role on charge carrier transport properties in devices in general, in both perovskite thin films and stacked solar cells based on methylammonium lead triiodide (MAPI) is presented. From time-of-flight (ToF) photocurrent measurements mobilities of approximately 6 cm^2/Vs are found for electrons and holes in MAPI films derived from a one-step deposition approach, whereas device mobilities are decreased by three orders of magnitude. By tuning the thickness of the hole as well as of the electron transporting material, it could be shown the transport time of photoinduced charge carriers under a constant external bias does not reflect the transport characteristics of the MAPI film but is mainly determined by the charge selective layers.

8.2 Materials and methods

The synthesis procedure for methylammonium lead triiodide thin films is based on a method recently published by Xiao et al. [42]. A solution containing PbI_2 (1.25 M, TCI 98%) and methylammonium iodide (1.25 M, Dyesol) in a 4:1 mixture of DMF and DMSO, respectively, was spin-coated onto the substrate at 1000 rpm for 10 s followed by 5000 rpm for 30 s. After 7 s of the second spinning step, 500 µL of anhydrous chlorobenzene (Sigma) were added on top of the substrate. Finally, the substrate was annealed at 40 °C for 40 min and 100 °C for 10 min. The obtained perovskite films revealed an average thickness of 350 nm, estimated via scanning electron microscopy cross-sections.

In-plane gold electrodes were fabricated using microstencil lithography techniques (see Chap. 3). Prior to all subsequent optical lithography steps, glass sheets were cleaned with a 2% Hellmanex solution and rinsed with deionized water. Afterwards the substrates were sonicated for 5 min in acetone and later with 2-propanol and exposed to oxygen plasma for 10 min to ensure the removal of surface residues and subsequent adhesion of the metallic contacts on glass. The structures were created via microstencil lithography by depositing a 30 nm thick layer of gold through a microscale shadow mask via thermal evaporation under vacuum (10^{-7} mbar). Finally, the coated glass sheets with inter-electrode distances between 36 and 80 µm were cleaned with 2-propanol.
Deposition of the perovskite thin films was done according to the fabrication protocol mentioned above. Additionally, the films were coated with a thin layer of poly(methyl methacrylate) (PMMA) by spincoating 50 mg/mL PMMA in anhydrous chlorobenzene in order to avoid degradation through ambient moisture.

Photovoltaic device preparation (see also Chap. 3) was carried out by successive deposition of electron transport layer (TiO_x), perovskite, hole transport layer (spiro-OMeTAD) and gold front contact on top of FTO (fluorine doped tin oxide) coated glass substrates. Fluorine doped tin oxide (FTO) coated glass substrates (7 Ω, Hartford Glass) were pat-

Tab. 8.1 Preparation parameters for different TiO_x thicknesses in perovskite-based solar cells. The final thicknesses were determined via SEM micrographs.

Spin speed [rpm]	**Number of layers**	**Thickness of TiO_x layer [nm]**
2000	1	70 ± 14
2000	2	120 ± 13
2000	3	150 ± 14
3000	2	105 ± 13
3000	3	130 ± 15

terned using zinc powder and 3 M HCl. Then the sheets were successively cleaned with deionized water, 2% Hellmanex solution, then once again with deionized water, acetone and ethanol. Oxygen plasma treatment for 5 min before applying the blocking layer aided in the removal of organic residues on the surface.

The substrates were then covered with a sol-gel derived TiO_x layer by spincoating the precursor solution, annealing at 150 °C (10 min) and calcining at 500 °C (45 min) in air [92]. For the sol-gel approach a solution of hydrochloric acid in 2-propanol (typically 35 µL of 2 M HCl and 2.5 mL of isopropanol) was added dropwise to a solution of titanium isopropoxide in anhydrous 2-propanol (367.5 µL titanium isopropoxide in 2.5 mL of 2-propanol) under vigorous stirring. Next, the solution was filtered with a 0.25 µm syringe filter and the remaining clear TiO_x solution was spin-coated onto the FTO substrates at 2000 rpm for 45 s.

To obtain different thicknesses of the blocking layer, TiO_x was spin-coated layer by layer. After deposition of the TiO_x solution at 2000 rpm or 3000 rpm for 45 s, the substrates were annealed at 150 °C and the next layer was spin-coated using the same settings. This procedure was repeated several times (see Tab. 8.1) and the resulting thicknesses were determined via SEM cross-sections.

After deposition of the hybrid perovskite film following the aforementioned synthesis procedure and a short cooling period to room temperature, a thin layer of spiro-OMeTAD serving as hole transporting material was spincoated at different speeds to tune the layer thickness (see Tab. 8.2). For this purpose, a 100 mg/mL solution of spiro-OMeTAD in anhydrous chlorobenzene was prepared and filtered. Oxidation of the material was performed by adding 10 µL of 4-tert-butylpyridine (Sigma 96%) and 30 µL of a 170 mg/mL lithium bistrifluoromethanesulfonimidate (Sigma 99.95%) solution in anhydrous acetonitrile (Sigma) to 1 mL of spiro-OMeTAD solution. The doped solution was then spin-coated on the coated substrate, which was stored in a desiccator at approximately 25% relative humidity to allow for oxidation of spiro-OMeTAD. Finally, 40 nm thick top gold electrodes

Tab. 8.2 Preparation parameters for different spiro-OMeTAD thicknesses in perovskite-based solar cells.

Spin speed [rpm]	Duration [s]	Thickness of spiro-OMeTAD layer [nm]
500	40	740 ± 12
2000	5	
1000	40	420 ± 18
2000	5	
1500	40	370 ± 10
2000	5	
2000	45	300 ± 22
3000	45	260 ± 18
5000	45	170 ± 13

were deposited by thermal evaporation of gold under vacuum ($> 5 \cdot 10^{-6}$ mbar).

8.3 Results and discussion

Pristine methylammonium lead triiodide (MAPI) films and thin MAPI absorber layers incorporated in photovoltaic devices were derived from a previously published synthesis protocol describing a fast deposition-crystallization procedure (FDC) [42]. Scanning electron micrographs of FDC-derived MAPI (Fig. 8.1 a) grown on FTO-coated glass substrates confirm a high surface coverage of large crystals with few grain boundaries and without pinholes, resulting in visually smooth films. The respective XRD pattern is shown in Fig. 8.1 b.

To identify the absorber material-related properties affecting the charge transport in perovskite-based solar cell devices, first experiments focusing on charge carrier mobilities in the pure $CH_3NH_3PbI_3$ film were performed. For this purpose, the MAPI thin film was deposited on top of laterally arranged metallic contacts with electrode spacings d in the range of several micrometers as shown in Fig. 8.1 c. To protect the moisture-sensitive perovskite from degradation in air, the samples were top-coated with a thin layer of poly(methyl methacrylate) (PMMA), thus permitting experiments under ambient conditions. This architecture allows for photocurrent measurements at different charge carrier travel distances through the film via the time-of-flight (ToF) measurement technique.

In brief, charge carriers are generated in the perovskite layer upon photoexcitation provided by a pulsed laser. The created charge carriers are separated by an applied DC voltage and

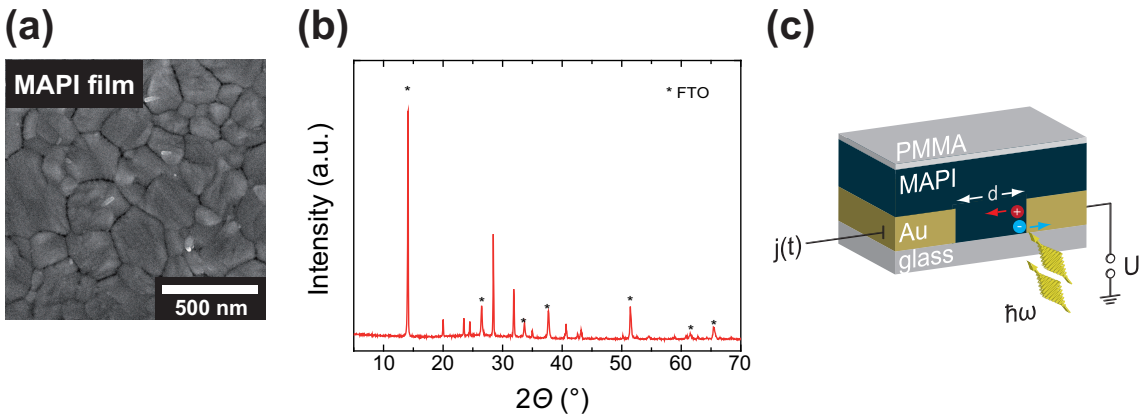

Fig. 8.1 Schematic illustration of the employed sample layout and the experimental setup. (a) SEM micrograph showing a top view of the investigated MAPI thin film. The image shows a high substrate coverage of the perovskite containing large crystals without the presence of pinholes. (b) XRD pattern of a MAPI film derived from the fast-crystallization deposition technique and grown on a TiO_x/FTO layer on glass. (c) Schematic of the laterally contacted perovskite thin film with varying spacings d between the electrodes. To prevent the film from degradation caused by moisture the MAPI layer is capped with PMMA. Upon pulsed laser light, charge carriers are induced in the absorber material and generate a photocurrent which allows for the observation of the charge carrier transit time used to derive the charge carrier mobility.

start moving toward the corresponding electrode, thus creating a current which recorded with an oscilloscope (see also description of the employed setup in Chap. 3). Because the charge carriers are locally created near one electrode, the polarity of the applied voltage determines whether the contribution of electrons or holes to the photocurrent extracted at the opposite electrode is observed. Fig. 8.2 a depicts the obtained time-resolved photocurrent traces for different electrode distances after pulsed excitation at 540 nm and a pulse duration of 7 ns. Because ionic migration within the perovskite film is anticipated and can affect the current flow, the DC field at 5 kV/cm was applied only during the short measurement period of single seconds to mitigate this influence. Because the observable influence of ion migration in electrical measurements, i.e. photocurrent transients, is known to occur in the timeframe of several minutes [66–68], ion migration is not expected to affect the investigated system significantly.

The shapes of the j-t profiles seen in Fig. 8.2 a indicate dispersive transport which could follow from a hopping behaviour of charge carriers (see Chap. 3). For this reason the analysis procedure introduced by Scher and Montroll [79] which has been applied to dispersive transport in a number of different materials including amorphous silicon and organic materials [176], was employed. In general, dispersive transport is understood to result from spatially varying hopping rates due to energetic heterogeneities caused by trapped space charges. For perovskite systems, detailed studies by other groups have shown that transport is based on a hopping mechanism at room temperature whereas it becomes band-like at low temperature [55, 109, 177].

The aforementioned procedure determines two linear fit functions for the plateau and the

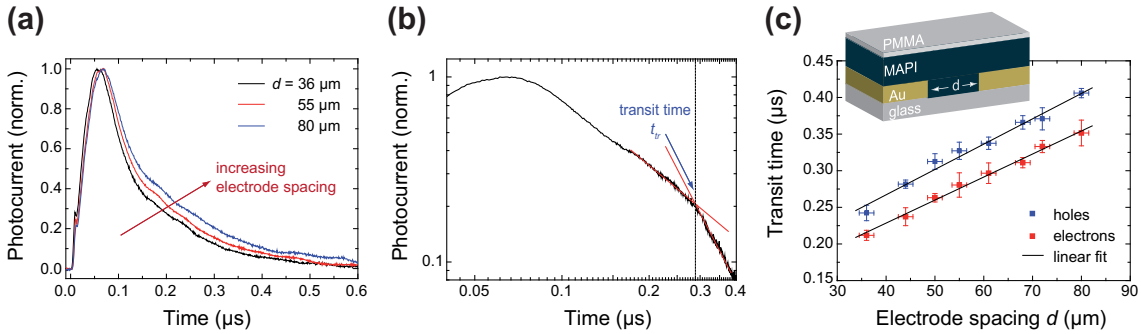

Fig. 8.2 Extraction of the charge carrier mobility in the perovskite layer from photocurrent experiments in lateral configuration. (a) Time-resolved photocurrent transients for three different electrode spacings obtained upon focused illumination close to one contact under DC biasing at 5 kV/cm. The broadening of the ToF traces for increasing gap sizes reflects larger transit times t_{tr} of the charge carriers through the film. (b) Fitting routine employed to extract t_{tr}. The determination of the transit time follows a procedure adapted from literature [79] and was performed via linear fit functions. For a higher reproducibility, an automatic fit routine was programmed based on an iterative fitting of linear function modeling [93]. After plotting the transient in a double logarithmic scale, the used algorithm identifies two linear fit functions for the plateau and the decay. (c) Extracted transit times for holes and electrons as a function of electrode spacing. t_{tr} scales linearly with the corresponding electrode distance, allowing for the determination of the μ and resulting in a value of 5.8 ± 0.3 cm^2/Vs for holes and 6.3 ± 0.2 cm^2/Vs for electrons.

decay of the double logarithmic *j-t* profile whereas the transit time t_{tr} is defined by the point where they intersect (illustrated in Fig. 8.2 b). To enhance the reproducibility of the determination of t_{tr}, a fit routine was programmed based on the iterative modeling of the slopes of pre- and post-transit linear functions close to the point of interest in the transient. According to the expression

$$\mu = \frac{d}{E \cdot t_{tr}} \tag{8.1}$$

with d being the inter-electrode distance and E being the applied electric field, the average charge carrier mobility is obtained by linearly fitting the curve relating the transit time with the electrode spacing (see Fig. 8.2 c). The linear dependence of the transit time t_{tr} on the electrode spacing d is visible in Fig. 8.2 a and Fig. 8.2 c, reflecting the respective distance the carriers need to travel to the distal electrode after being created by focused laser excitation at the other electrode. As described by the model in Eqn. 8.1 the slope of the linear regression allows for the determination of the charge carrier mobility in the MAPI film and results in μ_{MAPI,h^+}= 5.8 ± 0.3 cm^2/Vs and μ_{MAPI,e^-}= 6.3 ± 0.2 cm^2/Vs. The applicability of the mobility equation is confirmed by applying different bias voltages for a fixed gap size.

In the literature different charge carrier mobilities have been reported for MAPI ranging from 3 cm^2/Vs to several tens of cm^2/Vs [16, 57–59] using contact-less measurement techniques including time-resolved microwave conductivity (TRMC) and THz spectroscopy. For contacted MAPI films on the other hand, FET and Hall mobility measurements

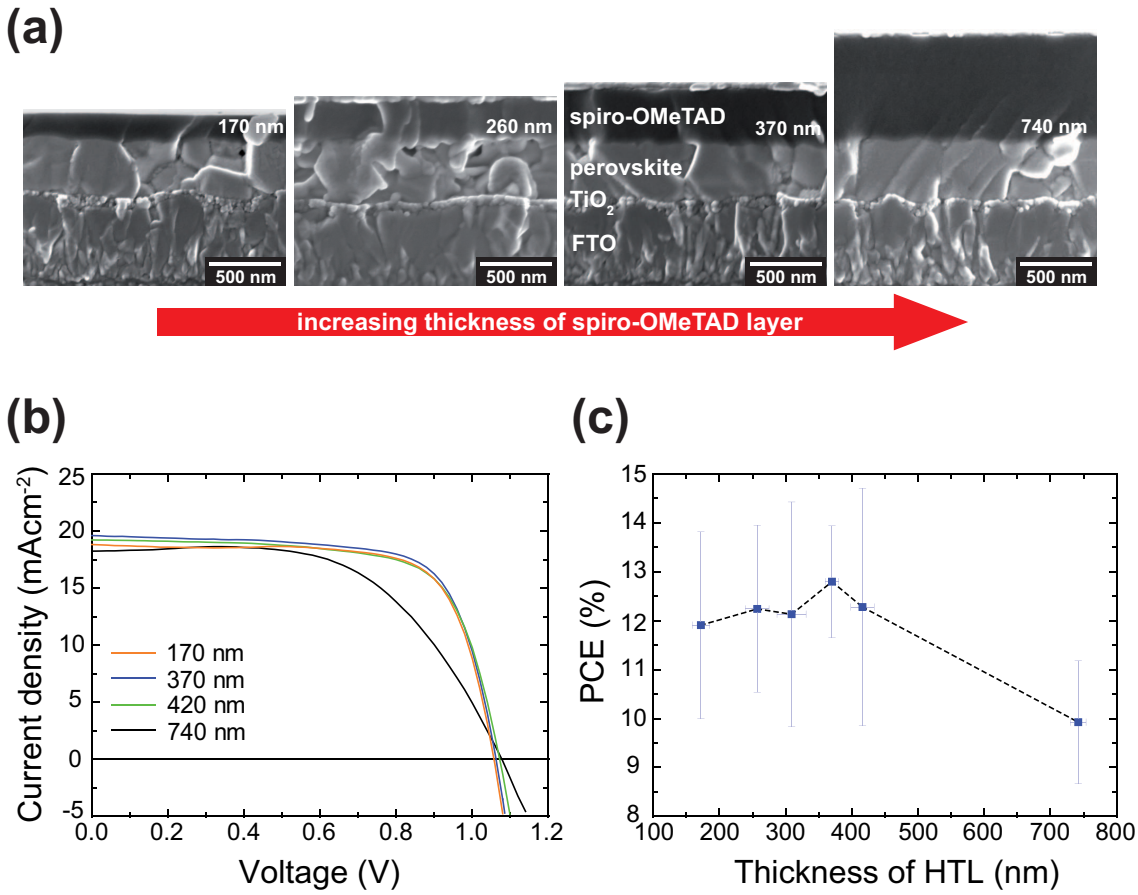

Fig. 8.3 Characterization of the MAPI-based photovoltaic devices. (a) Cross-sectional views of the stacks with varying layer thicknesses of the hole transporter spiro-OMeTAD. The MAPI and TiO_x thicknesses were kept constant at 360 nm and 70 nm, respectively. MAPI residues visible on the spiro-OMeTAD layer are a result of cutting the sample prior to the SEM measurement and are not induced by film growth. (b) *J-V* performance of working devices with different thicknesses of the hole transport layer (HTL) under simulated AM 1.5G illumination. (c) Statistical analysis of corresponding power conversion efficiencies from more than 120 individual photovoltaic devices. Best average performance was observed for a spiro-OMeTAD layer thickness of 370 nm.

provide lower values between 0.5 and 8 cm^2/Vs [60–62]. The charge carrier mobilities obtained here for contacted films are well within the range of these values. In contrast to the contact-less techniques mentioned above, which probe a rather local mobility, the mobilities in lateral direction are probed over several micrometers where the influence of grain boundaries and defects, i.e. potential trapping sites, becomes significant. To date, none of the optimized solution-processing techniques available at present (see for example refs. [42,44,67]) permit film thicknesses exceeding 300-500 nm, thus the thickness dependence of the material cannot be studied in the vertical direction in a significant range.

To gain further insights into the transport processes of photoinduced charge carriers in working solar cell devices, the studies were complemented by investigating thin film stacks incorporating the previously analyzed organolead halide perovskite material. With the MAPI film being sandwiched between spiro-OMeTAD and TiO_x as the hole and the elec-

tron transport layers, respectively, and contact layers (gold and FTO), the illumination of the perovskite occurs from the transparent FTO side.

In the following experiments the effects of the charge extraction layers on the transit time of charge carriers were investigated for constant thickness of the absorber material whereas varying the thickness of the charge extraction layer. Cross-sectional SEM images of photovoltaic devices confirm the successful tuning of the thickness of the hole transport layer (HTL) spiro-OMeTAD (see Fig. 8.3 a) ranging from 170 to 740 nm at constant TiO_x and MAPI thickness (70 and 360 nm, respectively). Note that the MAPI residues visible on the HTM layer (see for example second cross-section in Fig. 8.3 a) result from cutting the solar cell shortly before performing the SEM measurement. These residues attach to the cross-section and are not induced by a non-uniform deposition of the organic spiro-OMeTAD layer on the absorber material which could occur if the MAPI surface would be rough. Moreover, the MAPI film thickness seen in the SEM cross-sections corresponds to the typical values deduced using AFM or profilometers [178, 179].

J-V analysis (Fig. 8.3 b) of this type of cells under simulated AM 1.5G illumination confirms proper operation characteristics with typical deviations of ± 2%. Furthermore, PCE statistics from more than a total of 120 solar cells indicate that the conversion of incident light to current reaches the best average performance value of 12.8 ± 1.14% for a HTL thickness of 370 nm (see Fig. 8.3 c). Comparable results have been obtained in a similar HTM study performed by Marinova et al. [180] where the authors observe the best *J-V* performance for a spiro-OMeTAD thickness between 200 and 400 nm.

Equivalent measurements on photovoltaic devices with varying thicknesses of the electron transport layer (ETL) TiO_x as well as the corresponding cross-sections of the samples and additional EQE data (highlighting that there is no significant contribution of the spiro-OMeTAD layer to the overall photocurrent) can be found elsewhere [170]. Moreover, additional *J-V* performance measurements at different pre-bias conditions and scanning rates (see [170]) were performed to ensure the high quality of the perovskite films studied in this work and to illustrate the influence of the choice of the parameter set on the hysteresis behaviour. However, in the following ToF experiments it is not expected that the observed hysteresis has a significant influence on the mobility because of a very limited time frame of the electric field applied to the devices. Subsequently, photocurrent measurements were conducted on the stacked devices with varying thickness of hole or electron transport layer. For this purpose, the samples were illuminated from the transparent FTO side using an aperture mask with an active area of approximately 3x3 mm^2, identical with the illuminated area in the cell performance experiments. Fig. 8.4 a illustrates the *j-t* profiles for the stacked devices with different spiro-OMeTAD layer thicknesses. The transit time was extracted by employing the same fitting routine which was used for the transients in the lateral configuration. To verify the applicability of Eqn. 8.1 to the obtained data, the transit times at different applied bias voltages were plotted as shown in Fig. 8.4 b. Note that the hole transporter is not expected to substantially screen the electric field. Here, the oxidation of spiro-OMeTAD through the addition of LiTFSI, typically referred

to as "Li-doping", does not generate free carriers. Instead, the increased conductivity and mobility in spiro are attributed to the smoothing of the potential landscape which enhances the probability of inter-molecular charge transfer [181].
From the slope of the linear regression relating t_{tr} and U_{bias} (values corrected for a fixed built-in voltage of 0.022 V as determined in ref. [182]) in Fig. 8.4 b a mobility of $\mu = (6.2 \pm 0.4) \cdot 10^{-3}$ cm^2/Vs (assuming $d = d_{ETL} + d_{MAPI} + d_{HTL}$) is derived.

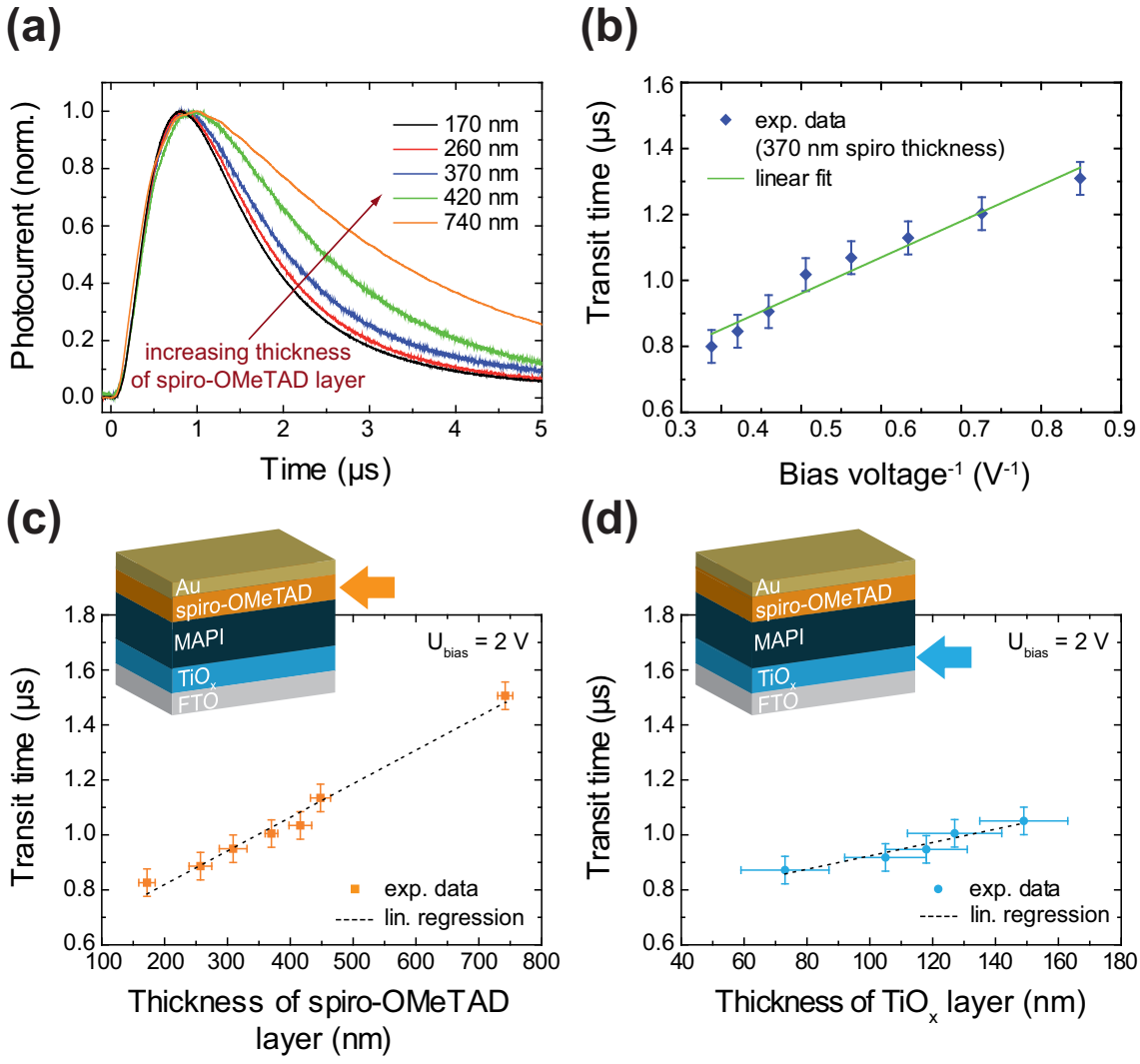

Fig. 8.4 Photocurrent transients obtained for complete perovskite-based solar cell devices. (a) Representative transients of photovoltaic devices (as shown in Fig. 8.3 a) with varying thicknesses of the HTL spiro-OMeTAD on top of the photoactive MAPI layer. (b) Extracted transit times as a function of reciprocal applied DC voltage for a defined thickness of the spiro compound. The transit time follows a linear dependence on U^{-1} (see Eqn. 8.1). (c) Transit times determined from the transients shown in (a) versus corresponding spiro-OMeTAD thickness. When increasing the layer thickness of the HTL the transit time is extended. (d) Effect of ETL (TiO_x thickness on the transit of charge carriers across the stack. Similar to the results shown in (c), the electron extraction layer affects the transport speed of charge carriers. The MAPI layer thicknesses in (c) and (d) were kept constant at 350 nm.

Several time-of-flight experiments on perovskite-based solar cells have already been performed resulting in a variety of obtained values for charge carrier mobilities, ranging from $4.6{\cdot}10^{-5}$ and $5.4{\cdot}10^{-4}$ cm^2/Vs [169, 177] to 0.06 and 1.4 cm^2/Vs [182]. This variety can most probably be assigned to different employed sample architectures as it is the case in refs. [177] and [169] where inverted solar cell devices were investigated with different charge extraction materials (PEDOT:PSS and PCBM) . Furthermore, the fabrication procedure for these absorber layers is based on either a two-step process [169, 177], which results in smaller crystallites and affects the charge transport processes, or a one-step process employing different synthesis conditions such as varying anti-solvent or annealing conditions [182]. The evaporation of differing metallic contacts (Al [169, 177] or Ag [182] compared to Au in this study) may also contribute to these varying mobility values as well as the definition of d. In some reports, d was taken as the thickness of the active absorber layer only whereas in the present analysis transport through all layers up to the contact was considered which consequently results in an increase in the respective charge carrier mobility by about a factor of 4.6.

As seen in Fig. 8.4 the transport of charge carriers is substantially influenced by the thickness of the HTL, which is reflected in larger t_{tr} values starting from 0.82 up to 1.51 µs for increased travel distances, ranging from 170 to 740 nm (Fig. 8.4 c). Additional ToF experiments on devices without a HTL and devices incorporating a very thin layer of MAPI are showing virtually identical transients and underlining that the transit time in devices is almost entirely dominated by the thickness of spiro-OMeTAD, respectively, are depicted in Fig. 8.5.

A similar effect is observed for increasing ETL thickness (Fig. 8.4 d), where the transit time increases from 0.87 to 1.05 µs with thicknesses ranging from 70 to 150 nm. Note that the growth of the ETL on the rather rough FTO surface consequently leads to some variations in the thickness (see reference [170]), resulting in large error bars in the chart. Furthermore, the chemical fabrication process employed for the samples in these specific experiments does not allow the creation of uniform films below a certain thickness of approximately 60-70 nm, thus the present measurements include samples with ETL thickness exclusively above the minimal obtainable thickness. On the other hand, the minimum thickness of the spiro-OMeTAD layer is limited by the formation of pinholes to about 170 nm at which a reduction of the PCE is observed.

For the HTL and the ETL similar slopes of 1.22 ± 0.07 and 2.43 ± 0.36 nm/ns, respectively, were found. Additionally, the calculated mobility values as a function of HTL and ETL thickness are consistent, assuming d as the sum of the thicknesses of all layers, and show only minor variations (as shown in [170]).

Based on the charge carrier mobility values obtained from the experiments on laterally contacted MAPI, the average drift velocity v_d of holes through the absorber layer is calculated according to the expression

$$v_d = \mu_{MAPI,h} \cdot E \tag{8.2}$$

and results in 290 nm/ns. With the thickness of MAPI (approximately 360 nm) in the full solar cell device, the contribution of the perovskite absorber layer to the overall transit time of the device can be estimated to be ∼1 ns. This number represents an upper limit because it can be expected that in the vertical solar cell architecture the charges will have to pass a smaller number of grain boundaries than in the lateral measurements presented in Fig. 8.2. Clearly, the estimated transit time is much smaller than the effective transit times observed for the HTL and the ETL.

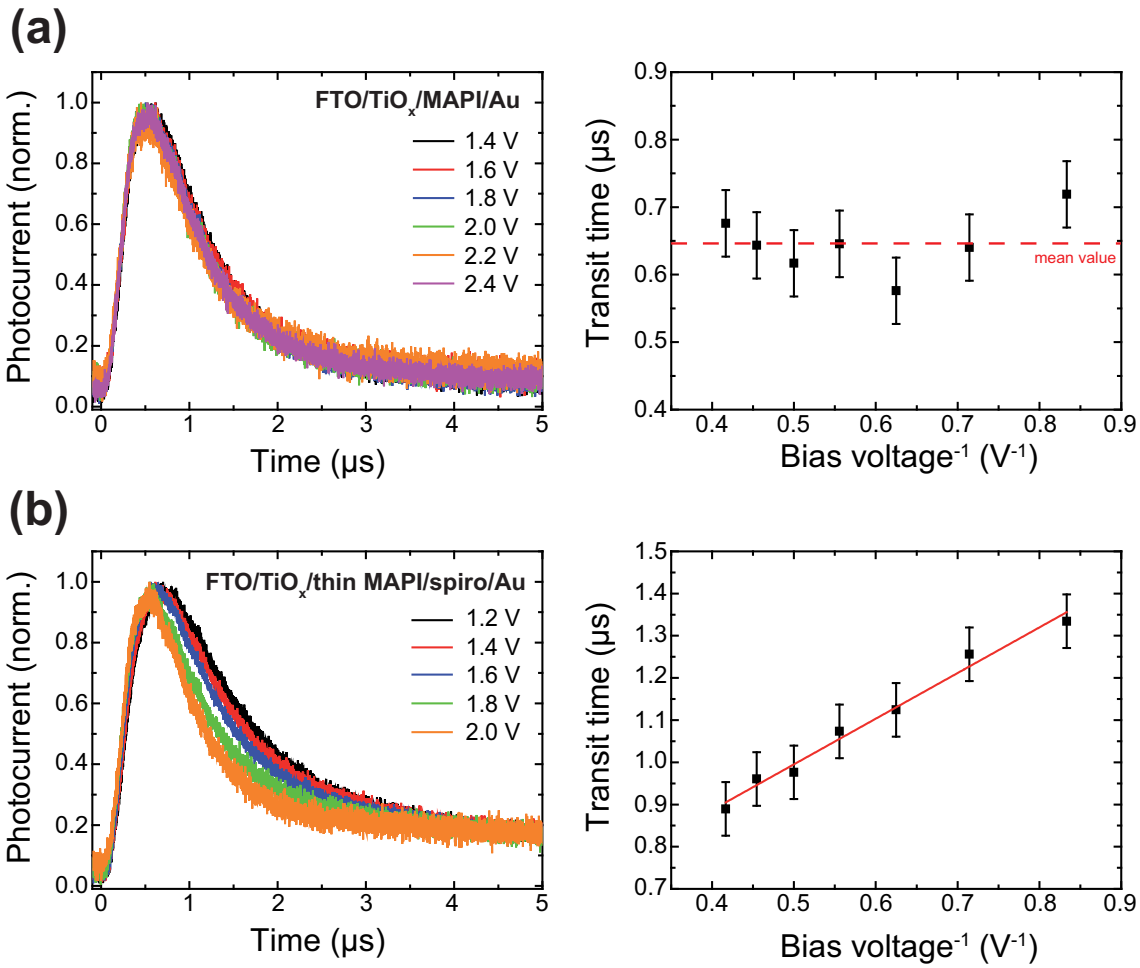

Fig. 8.5 ToF results for two extreme cases of solar cell devices. (a) Photocurrent curves obtained for a device without the HTL spiro-OMeTAD and the respective transit times. The transients are virtually identical since the transport time for a 350 nm thick layer of MAPI is below 1 ns which is below the temporal resolution limit of the employed oscilloscope. (b) *j-t* profiles for a device with a very thin MAPI layer (approx. 100 nm) and 370 nm of spiro-OMeTAD and corresponding transit times, showing nearly the same transit time of about 0.95 µs at 2 V when incorporating a full-sized MAPI layer of 350 nm as shown in Fig. 8.2 c. This underlines that the transit time in a device in almost entirely determined by the thickness of the spiro layer.

From the observations in the ToF experiments performed on the devices, it is suggested that the effective charge carrier transit times in perovskite solar cells are mainly affected by the thickness of spiro-OMeTAD and to a lesser extent by the thinner TiO_x layer. This

also leads to a reduction of the PCE for thicker layers and to pinholes and shunting for thinner spiro-OMeTAD layers, resulting in an optimum thickness of around 370 nm. Furthermore, the derived mobility values in the devices match the hole mobilities in oxidized spiro-OMeTAD thin films well (μ_h = 4.6·10^{-4} - 1.6·10^{-3} cm^2/Vs [181, 183]) and further indicate that the hole transporter determines the transit times in the investigated stacked perovskite-based solar cells. Consequently, the measurements on the contacted film establish that the absorber layer and its properties could be excluded from affecting the transport of photogenerated charges in working devices. This highlights that rather the thickness of the extraction layers, in particular of the HTL, is a major limiting factor for charge transport. Recently published investigations already demonstrate different approaches to replace the commonly employed material spiro-OMeTAD by other organic or inorganic hole transporters such as EDOT-OMeTPA [184] or graphene [185] and TiO_x by tin dioxide [186].

8.4 Conclusion

In this study, the mobilities of light-induced charge carriers in both individually contacted MAPI thin films and photovoltaic stacks based on this type of hybrid perovskite were investigated. Employing the time-of-flight photocurrent technique, charge carrier mobilities of 5.8 ± 0.3 cm^2/Vs for holes and 6.3 ± 0.2 cm^2/Vs for electrons in individual perovskite films in lateral dimensions were observed. Compared to the mobilities determined for the n-i-p architecture consisting of FTO/TiO_x/MAPI/spiro-OMeTAD/Au and resulting in values decreased by three orders of magnitude, the photoactive perovskite layer can clearly be excluded from being a charge transport limiting factor in the device. Complementary ToF experiments on solar cells with varying spiro-OMeTAD thickness demonstrate a significant increase of the transit time of charge carriers through the device stack with increasing extraction layer thicknesses. By tuning the TiO_x thickness, a similar effect on the transit times is observed. From this it is concluded that mainly the thickness of spiro-OMeTAD contributes substantially to the transit time and to the mobility in the stacked system. Hence, the hole transport layer represents a major transport limiting factor in the working device that should be considered in efforts aimed at further device and interface engineering.

9 Summary and Outlook

9.1 Summary

Organic-inorganic metal halide perovskites have developed into promising candidates for next-generation solar cell technologies and other optoelectronic applications within less than a decade of research activities in this field. In this thesis the opto-electronic and optical properties of the archetypical hybrid perovskite compound methylammonium lead triiodide (MAPI), derived from different synthesis protocols, are investigated to provide new insights into their charge transport properties. Detailed knowledge and proper understanding of the charge carrier dynamics in neat perovskite films as well as in stacked thin film devices based on these materials is a key factor for rational design and further improvement of the material for future applications, in particular for photovoltaics, but also for light-emitting devices, transistors or lasers.

In Chap. 4, pure MAPI films following a two-step sequential deposition crystallization technique, in which initially a PbI_2 layer is deposited on the substrate followed by perovskite film formation due to immersion into a methylammonium iodide solution, are compared to films that are additionally treated with a chloride-containing precursor salt during the second step. Although both films are very similar with respect to morphology and composition, showing crystal sizes around 250 nm and indicating that the same crystal structure is formed without incorporation of any chloride anion into the final film structure, substantial differences are observed regarding charge carrier transport and solar cell performance. By combining time-of-flight (ToF) charge carrier mobility measurements with time-resolved photoluminescence measurements, an increase of charge carrier mobilities from 1.6 to 2.2 cm^2/Vs in chloride-treated films is observed, whereas PL intensity averaged lifetimes in steady-state conditions alter from 70 to 100 ns. Furthermore, power conversion efficiencies are boosted from 5.3 to 10.3% on average when incorporated in lab-scale thin film photovoltaic devices. Deduced from in-situ PL measurements monitoring the change of charge carrier lifetimes during film formation upon pulsed laser excitation, this effect can be attributed to a retarded crystallization during film growth triggered by the presence of chloride anions which results in fewer defects and quenching sites in the crystals.

Chap. 5 compares MAPI films derived from the two-step synthesis protocol with films obtained from a one-step fast-crystallization approach. Contrary to the sequential deposition, in the one-step protocol the final perovskite solution is coated onto the substrate while homogeneous film formation is assisted by the addition of an antisolvent such as chlorobenzene and results in larger grain sizes within the film. The implications of both

techniques on the transport properties in lateral dimensions are investigated via spatio-temporal photoluminescence and time-resolved photocurrent experiments. Films that are prepared following the fast-crystallization route reveal shorter intensity averaged photoluminescence lifetimes of 16 ns compared to 38 ns in two-step MAPI and a 3-4 times higher diffusion constant of 30 cm^2/s which is most likely affected by radiative transport. Also, an enhancement of charge carrier mobilities from 1.6 to 2.6 cm^2/Vs and power conversion efficiencies (PCE) from 7.8 to 12.4% on average in solar cell devices when comparing SDC to FDC films is observed. The improved charge carrier mobility and PCE can be attributed to a reduced density of grain boundaries in FDC films.

Chap. 6 describes the experimental analysis of charge carrier mobilities in a millimeter-sized MAPI crystal by using the time-of-flight technique. Photogenerated charges in this particular system show hole mobilities of 119 cm^2/Vs and electron mobilities of 130 cm^2/Vs which is 10 to 100 times larger compared to the values observed for thin MAPI films with differing grain sizes investigated by the same technique in lateral direction on a micrometer scale. MAPI thin film mobilities are strongly affected by the grain size which is accompanied by a corresponding density of boundaries representing potential recombination sites and energy barriers and hence an extrinsic factor limiting charge transport. Extrinsic factors can be minimized by the use of suitable conditions such as temperature or type of solvent during film fabrication as demonstrated within this section where mobilities up to 32 cm^2/Vs (sum of hole and electron mobility) are found.

In Chap. 7 the crystallization of methylammonium lead triiodide derived from a one-step approach with a chloride-based precursor and the effect of controlled solvent evaporation on the optoelectronic properties in the respective devices is studied. By monitoring the crystal growth with in-situ X-ray diffraction measurements, a crystallization mechanism is identified where methylammonium lead chloride is formed on the substrate while heating of the substrate leads to the growth of oriented methylammonium lead triiodide grains at the expense of the template material. Slow evaporation of the solvent is highly beneficial for the morphology of the derived films which directly results in improved charge carrier mobilities by a factor of two (provided that the stacking sequence and the respective layer thicknesses are identical for the compared systems), enhanced conductivity in the solar cell devices and increased power conversion efficiencies.

Chap. 8 sheds light on the impact of charge extraction layers on the transport of photoinduced carriers in perovskite-based solar cells. Time-of-flight experiments on a laterally contacted individual MAPI film highlight balanced charge carrier mobilities around 6 cm^2/Vs for both holes and electrons which represent remarkably high values given the fact that the investigated thin film system is derived from solution processing. When applying the same measurement technique in vertical direction to lab-scale photovoltaic devices based on the same perovskite material being sandwiched between hole and electron extraction layers (spiro-OMeTAD/Au and TiO_x/FTO, respectively), the resulting values decrease by 3-4 orders of magnitude, indicating that the absorber material is unlikely to limit charge transport in the device. By varying the thickness of the hole transport layer,

the experimentally determined transit times of charge carriers through the stack increase with increasing thickness, suggesting the hole transport layer as a major transport limiting factor in the device and demonstrating the need of further engineering of the device and the respective interfaces to ensure efficient charge transport in the working solar cell.

9.2 Outlook

Based on the insights gained in this thesis, further experiments should be carried out focusing on the examination of the composition and the size of the grain boundaries in perovskite thin films. The results could potentially shed light on the charge transfer processes between individual perovskite crystals in the film. This knowledge might be beneficial for an improved understanding of charge transport mechanisms in lateral dimensions and could potentially contribute to an overall model describing the charge carrier dynamics in perovskite thin film systems. Furthermore, temperature-dependent lateral ToF studies on perovskite thin films are expected to provide additional information on the nature of the charge transport and the trap densities as well as the effect of the transition from the tetragonal to the orthorhombic phase on these parameters. Also, low-temperature experiments could reveal more details on the origin of the modest charge carrier mobility values observed at room temperature which are speculated to arise from intrinsic effects.

Bibliography

[1] A. W. D. Larkum, "Limitations and Prospects of Natural Photosynthesis for Bioenergy Production," Curr. Opin. Biotechnol. **21**, 271–276 (2010).

[2] P. Moriarty and D. Honnery, "What Energy Levels can the Earth Sustain?" Energy Pol. **37**, 2469–2474 (2009).

[3] V. V. Tyagi, N. A. A. Rahim, N. A. Rahim, and J. A. L. Selvaraj, "Progress in Solar PV Technology: Research and Achievement," Renew. Sustainable Energy Rev. **20**, 443–461 (2013).

[4] L. El Chaar, L. A. Iamont, and N. El Zein, "Review of Photovoltaic Technologies," Renew. Sustainable Energy Rev. **15**, 2165–2175 (2011).

[5] A. E. Becquerel, "Untersuchung über die Hervorrufung der Phosphorescenz und über verschiedene Eigenschaften des elektrischen Funkens," Ann. Phys. **124**, 540–549 (1839).

[6] A. Einstein, "Über einen die Erzeugung und Verwandlung des Lichtes betreffenden heuristischen Gesichtspunkt," Ann. Phys. **322**, 132–148 (1905).

[7] D. M. Bagnall and M. Boreland, "Photovoltaic Technologies," Energy Pol. **36**, 4390–4396 (2008).

[8] T. M. Razykov, C. S. Ferekides, D. Morel, E. Stefanakos, H. S. Ullal, and H. M. Upadhyaya, "Solar Photovoltaic Electricity: Current Status and Future Prospects," Sol. Energy **85**, 1580–1608 (2011).

[9] E. Płaczek-Popko, "Top PV Market Solar Cells 2016," Opto-electron. Rev. **25**, 55–64 (2017).

[10] M. A. Green, Y. Hishikawa, W. Warta, E. D. Dunlop, D. H. Levi, J. Hohl-Ebinger, and A. W. Y. Ho-Baillie, "Solar Cell Efficiency Tables (version 50)," Prog. Photovolt.: Res. Appl. **25**, 668–676 (2017).

[11] A. Kojima, K. Teshima, Y. Shirai, and T. Miyasaka, "Organometal Halide Perovskites as Visible-Light Sensitizers for Photovoltaic Cells," J. Am. Chem. Soc. **131**, 6050–6051 (2009).

[12] W. S. Yang, B.-W. Park, E. H. Jung, N. J. Jeon, Y. C. Kim, D. U. Lee, S. S. Shin, J. Seo, E. K. Kim, J. H. Noh, and S. I. Seok, "Iodide Management in Formamidinium-Lead-Halide-Based Perovskite Layers for Efficient Solar Cells," Science **356**, 1376–1379 (2017).

[13] S. De Wolf, J. Holovsky, S.-J. Moon, P. Löper, B. Niesen, M. Ledinsky, F.-J. Haug, J.-H. Yum, and C. Ballif, "Organometallic Halide Perovskites: Sharp Optical Absorption Edge and Its Relation to Photovoltaic Performance," J. Phys. Chem. Lett. **5**, 1035–1039 (2014).

[14] J. H. Noh, S. H. Im, J. H. Heo, T. N. Mandal, and S. I. Seok, "Chemical Management for Colorful, Efficient, and Stable Inorganic-Organic Hybrid Nanostructured Solar Cells," Nano Lett. **13**, 1764–1769 (2013).

[15] S. D. Stranks, G. E. Eperon, G. Grancini, C. Menelaou, M. J. P. Alcocer, T. Leijtens, L. M. Herz, A. Petrozza, and H. J. Snaith, "Electron-Hole Diffusion Lengths Exceeding 1 Micrometer in an Organometal Trihalide Perovskite Absorber," Science **342**, 341–344 (2013).

[16] C. Wehrenfennig, G. E. Eperon, M. B. Johnston, H. J. Snaith, and L. M. Herz, "High Charge Carrier Mobilities and Lifetimes in Organolead Trihalide Perovskites," Adv. Mater. **26**, 1584–1589 (2014).

[17] D. M. Chapin, C. S. Fuller, and G. L. Pearson, "A New Silicon p-n Junction Photocell for Converting Solar Radiation into Electrical Power," J. Appl. Phys. **25**, 676–677 (1954).

[18] P. Würfel, *Physics of Solar Cells. From Principles to New Concepts* (Wiley-VCH Verlag, Weinheim, 2005).

[19] H. Häberlin, *Photovoltaics. System Design and Practice* (Wiley, Chichester, 2012).

[20] P. A. Lynn, *Electricity from Sunlight. An Introduction to Photovoltaics* (Wiley, Chichester, 2010).

[21] M. A. Green, "Improved Value for the Silicon Free Exciton Binding Energy," AIP Adv. **3**, 112 104 (2013).

[22] L. Schmidt-Mende and J. Weickert, *Organic and Hybrid Solar Cells* (de Gruyter, Berlin, 2016).

[23] A. J. Heeger, "Bulk Heterojunction Solar Cells: Understanding the Mechanism of Operation," Adv. Mater. **26**, 10–28 (2014).

[24] L. Herz, "Charge-Carrier Dynamics in Organic-Inorganic Metal Halide Perovskites," Annu. Rev. Phys. Chem. **67**, 65–89 (2016).

[25] X. Wang and Z. M. Wang, *High-Efficiency Solar Cells: Physics, Materials and Devices* (Springer, Heidelberg, 2009).

[26] R. Murri, *Silicon Based Thin Film Solar Cells* (Bentham Science Publishers, Oak Park, 2013).

[27] C. Jacobini, *Theory of Electron Transport in Semiconductors* (Springer, Heidelberg, 2010).

[28] G. Hodes and P. V. Kamat, "Understanding the Implication of Carrier Diffusion Length in Photovoltaic Cells," J. Phys.Chem. Lett. **6**, 4090–4092 (2015).

[29] W. Brütting, *Physics of Organic Semiconductors* (Wiley-VCH, Weinheim, 2005).

[30] S. Bandyopadhyay, *Physics of Nanostructured Solid State Devices* (Springer, New York, 2012).

[31] W. Shockley and H. J. Queisser, "Detailed Balance Limit of Efficiency of p-n Junction Solar Cells," J. Appl. Phys. **32**, 510–519 (1961).

[32] S. Rühle, "Tabulated Values of the Shockley-Queisser Limit for Single Junction Solar Cells," Sol. Energy **130**, 139–147 (2016).

[33] B. O'Regan and M. Grätzel, "A Low-Cost, High-Efficiency Solar Cell Based on Dye-Sensitized Colloidal TiO_2 Films," Nature **353**, 737–740 (1991).

[34] U. Bach, D. Lupo, P. Comte, J. E. Moser, F. Weissörtel, J. Salbeck, H. Spreitzer, and M. Grätzel, "Solid-State Dye-Sensitized Mesoporous TiO_2 Solar Cells with High Photon-To-Electron Conversion Efficiencies," Nature **395**, 583–585 (1998).

[35] M. Peplow, "Henry Snaith: Sun Worshipper," Nature **504**, 364–365 (2013).

[36] R. E. Cohen, "Origin of Ferroelectricity in Perovskite Oxides," Nature **358**, 136–138 (1992).

[37] J. G. Bednorz and K. A. Müller, "Possible High T_c Superconductivity in the Ba-La-Cu-O System," Z. Phys. B - Condensed Matter **64**, 189–193 (1986).

[38] D. B. Mitzi, C. A. Feild, W. T. A. Harrison, and A. M. Guloy, "Conducting Tin Halides with a Layered Organic-Based Perovskite Structure," Nature **369**, 467–469 (1994).

[39] M. M. Lee, J. Teuscher, T. Miyasaka, T. N. Murakami, and H. J. Snaith, "Efficient Hybrid Solar Cells Based on Meso-Superstructured Organometal Halide Perovskites," Science **338**, 643–646 (2012).

[40] J. Burschka, N. Pellet, S.-J. Moon, R. Humphry-Baker, P. Gao, M. K. Nazeeruddin, and M. Grätzel, "Sequential Deposition as a Route to High-Performance Perovskite-Sensitized Solar Cells," Nature **499**, 316–319 (2013).

[41] M. Liu, M. B. Johnston, and H. J. Snaith, "Efficient Planar Heterojunction Perovskite Solar Cells by Vapour Deposition," Nature **501**, 395–398 (2013).

[42] M. Xiao, F. Huang, W. Huang, Y. Dkhissi, Y. Zhu, J. Etheridge, A. Gray-Weale, U. Bach, Y.-B. Cheng, and L. Spiccia, "A Fast Deposition-Crystallization Procedure for Highly Efficient Lead Iodide Perovskite Thin-Film Solar Cells," Angew. Chem. Int. Ed. **53**, 9898–9903 (2014).

[43] D. Bi, W. Tress, M. I. Dar, P. Gao, J. Luo, C. Renevier, K. Schenk, A. Abate, F. Giordano, J.-P. Correa Baena, J.-D. Decoppet, S. M. Zakeeruddin, M. K. Nazeeruddin, M. Grätzel, and A. Hagfeldt, "Efficient Luminescent Solar Cells Based on Tailored Mixed-Cation Perovskites," Sci. Adv. **2**, 1501 170 (2016).

[44] P. Docampo, F. C. Hanusch, S. D. Stranks, M. Döblinger, J. M. Feckl, M. Ehrensperger, N. K. Minar, M. B. Johnston, H. J. Snaith, and T. Bein, "Solution Deposition-Conversion for Planar Heterojunction Mixed Halide Perovskite Solar Cells," Adv. Energy Mater. **4**, 1400 355 (2014).

[45] G. Grancini, C. Roldán-Carmona, I. Zimmermann, E. Mosconi, X. Lee, D. Martineau, S. Narbey, F. Oswald, F. De Angelis, M. Grätzel, and M. K. Nazeeruddin, "One-Year Stable Perovskite Solar Cells by 2D/3D Interface Engineering," Nat. Mater. **13**, 838–842 (2014).

[46] D. Nanova, A. K. Kast, M. Pfannmöller, C. Müller, L. Veith, I. Wacker, M. Agari, W. Hermes, P. Erk, W. Kowalsky, R. S. Schröder, and R. Lovrinčić, "Unraveling the Nanoscale Morphologies of Mesoporous Perovskite Solar Cells and Their Correlation to Device Performance," Nano Lett. **14**, 2735–2740 (2014).

[47] G. E. Eperon, S. D. Stranks, C. Menelaou, M. B. Johnston, L. M. Herz, and H. J. Snaith, "Formamidinium Lead Trihalide: A Broadly Tunable Perovskite for Efficient Planar Heterojunction Solar Cells," Energy Environ. Sci. **7**, 982–988 (2014).

[48] M. Saliba, T. Matsui, J.-Y. Seo, K. Domanski, J.-P. Correa-Baena, M. K. Nazeeruddin, S. M. Zakeeruddin, W. Tress, A. Abate, A. Hagfeldt, and M. Grätzel, "Cesium-Containing Triple Cation Perovskite Solar Cells: Improved Stability, Reproducibility and High Efficiency," Energy. Environ. Sci. **9**, 1989–1997 (2016).

[49] M. Saliba, T. Matsui, K. Domanski, J.-Y. Seo, A. Ummadisingu, S. M. Zakeeruddin, J. P. Correa-Baena, W. Tress, A. Abate, A. Hagfeldt, and M. Grätzel, "Incorporation of Rubidium Cations into Perovskite Solar Cells Improves Photovoltaic Performance," Science **354**, 206–209 (2016).

[50] N. K. Noel, S. D. Stranks, A. Abate, C. Wehrenfennig, S. Guarnera, A.-A. Haghighirad, A. Sadhanala, G. E. Eperon, S. K. Pathak, M. B. Johnston, A. Petrozza, L. M. Herz, and H. J. Snaith, "Lead-Free Organic-Inorganic Tin Halide Perovskites for Photovoltaic Applications," Energy Environ. Sci. **7**, 3061–3068 (2014).

[51] N. J. Jeon, J. H. Noh, Y. C. Kim, W. S. Yang, S. Ryu, and S. I. Seok, "Solvent Engineering for High-Performance Inorganic-Organic Hybrid Perovskite Solar Cells," Nat. Mater. **13**, 897–903 (2014).

[52] N. K. Noel, A. Abate, S. D. Stranks, E. Parrott, V. Burlakov, A. Goriely, and H. J. Snaith, "Enhanced Photoluminescence and Solar Cell Performance via Lewis Base Passivation of Organic-Inorganic Lead Halide Perovskites," ACS Nano **8**, 9815–9821 (2014).

[53] G. Xing, N. Mathews, S. Sun, S. S. Lim, Y. M. Lam, M. Grätzel, S. Mhaisalkar, and T. C. Sum, "Long-Ranged Balanced Electron- and Hole-Transport Lengths in Organic-Inorganic $CH_3NH_3PbI_3$," Science **342**, 344–347 (2013).

[54] H. Oga, A. Saeki, Y. Ogomi, S. Hayase, and S. Seki, "Improved Understanding of the Electronic and Energetic Landscapes of Perovskite Solar Cells: High Local Charge Carrier Mobility, Reduced Recombination, and Extremely Shallow Traps," J. Am. Chem. Soc. **136**, 13 818–13 825 (2014).

[55] R. L. Milot, G. E. Eperon, H. J. Snaith, M. B. Johnston, and L. M. Herz, "Temperature-Dependent Charge-Carrier Dynamics in $CH_3NH_3PbI_3$ Perovskite Thin Films," Adv. Funct. Mater. **25**, 6218–6227 (2015).

[56] D. Shi, V. Adinolfi, R. Comin, M. Yuan, E. Alarousu, A. Buin, Y. Chen, S. Hoogland, A. Rothenberger, K. Katsiev, Y. Losovyj, X. Zhang, P. A. Dowben, E. H. Mohammed, O. F.and Sargent, and O. M. Bakr, "Low Trap-State Density and Long Carrier Diffusion in Organolead Trihalide Perovskite Single Crystals," Science **347**, 519–522 (2015).

[57] C. S. Ponseca, T. J. Savenije, M. Abdellah, K. Zheng, A. Yartsev, T. Pascher, T. Harlang, P. Chabera, T. Pullerits, A. Stepanov, J.-P. Wolf, and V. Sundström, "Organometal Halide Perovskite Solar Cell Materials Rationalized: Ultrafast Charge Generation, High and Microsecond-Long Balanced Mobilities, and Slow Recombination," J. Am. Chem. Soc. **136**, 5189–5192 (2014).

[58] E. M. Hutter, G. E. Eperon, S. D. Stranks, and T. J. Savenije, "Charge Carriers in Planar and Meso-Structured Organic-Inorganic Perovskites: Mobilities, Lifetimes, and Concentrations of Trap States," J. Phys. Chem. Lett. **6**, 3082–3090 (2015).

[59] M. Karakus, S. A. Jense, F. D'Angelo, D. Turchinovich, M. Bonn, and E. Cánovas, "Phonon-Electron Scattering Limits Free Charge Mobility in Methylammonium Lead Iodide Perovskites," J. Phys. Chem. Lett. **6**, 4991–4996 (2015).

[60] Y. Mei, C. Zhang, Z. V. Vardeny, and O. D. Jurchescu, "Electrostatic Gating of Hybrid Halide Perovskite Field-Effect Transistors: Balanced Ambipolar Transport at Room-Temperature," MRS Communications **5**, 297–301 (2015).

[61] Y. Chen, H. Yi, X. Wu, R. Haroldson, Y. N. Gartstein, Y. I. Rodionov, K. S. Tikhonov, A. Zakhidov, X.-Y. Zhu, and V. Podzorov, "Extended Carrier Lifetimes and Diffusion in Hybrid Perovskites Revealed by Hall Effect and Photoconductivity Measurements," Nat. Commun. **7**, 12 253 (2016).

[62] S. P. Senanayak, B. Yang, T. H. Thomas, N. Giesbrecht, W. Huang, E. Gann, B. Nair, K. Goedel, S. Guha, X. Moya, C. R. McNeill, P. Docampo, A. Sadhanala, R. H. Friend, and H. Sirringhaus, "Understanding Charge Transport in Lead Iodide Perovskite Thin-Film Field-Effect Transistors," Sci. Adv. **3**, e1601 935 (2017).

[63] Y. Zhao and K. Zhu, "Organic-Inorganic Hybrid Lead Halide Perovskites for Optoelectronic and Electronic Applications," Chem. Soc. Rev. **45**, 655–689 (2016).

[64] E. L. Unger, E. T. Hoke, C. D. Bailie, W. H. Nguyen, A. R. Bowring, T. Heumüller, M. G. Christoforo, and M. D. McGehee, "Hysteresis and Transient Behavior in Current-Voltage Measurements of Hybrid-Perovskite Absorber Solar Cells," Energy. Environ. Sci. **7**, 3690–3698 (2014).

[65] Z. Xiao, Y. Yuan, Y. Shao, Q. Wang, Q. Dong, C. Bi, P. Sharma, A. Gruverman, and J. Huang, "Giant Switchable Photovoltaic Effect in Organometal Trihalide Perovskite Devices," Nat. Mater. **14**, 193–198 (2015).

[66] C. Eames, J. M. Frost, P. R. F. Barnes, B. C. O'Regan, A. Walsh, and M. S. Islam, "Ionic Transport in Hybrid Lead Iodide Perovskite Solar Cells," Nat. Commun. **6**, 7497 (2015).

[67] Y. Zhang, M. Liu, G. E. Eperon, T. C. Leijtens, D. McMeekin, M. Saliba, W. Zhang, M. de Bastiani, A. Petrozza, L. M. Herz, M. B. Johnston, H. Lin, and H. J. Snaith, "Charge Selective Contacts, Mobile Ions and Anomalous Hysteresis in Organic-Inorganic Perovskite Solar Cells," Mater. Horiz. **2**, 315–322 (2015).

[68] W. Tress, N. Marinova, T. Moehl, S. M. Zakeeruddin, M. K. Nazeeruddin, and M. Grätzel, "Understanding the Rate Dependent J-V Hysteresis, Slow Time Component, and Aging in $CH_3NH_3PbI_3$ Perovskite Solar Cells: The Role of a Compensated Electric Field," Energy Environ. Sci. **8**, 995–1004 (2015).

[69] H. J. Snaith, A. Abate, J. M. Ball, G. E. Eperon, T. Leijtens, N. K. Noel, S. D. Stranks, J. T.-W. Wang, K. Wojciechowski, and W. Zhang, "Anomalous Hysteresis in Perovskite Solar Cells," J. Phys. Chem. Lett. **5**, 1511–1515 (2014).

[70] T. M. Schmidt, T. T. Larsen-Olsen, J. E. Carlé, D. Angmo, and F. C. Krebs, "Upscaling of Perovskite Solar Cells: Fully Ambient Roll Processing of Flexible Perovskite Solar Cells with Printed Back Electrodes," Adv. Energy Mater. **5**, 1500 569 (2015).

[71] Y. Wu, X. Yang, W. Chen, Y. Youfeng, M. Cai, F. Xie, E. Bi, A. Islam, and L. Han, "Perovskite Solar Cells with 18.2% efficiency and area over 1 cm^2 Fabricated by Heterojunction Engineering," Nat. Energy **1**, 16 148 (2016).

[72] M. Grätzel, "The Light and Shade of Perovskite Solar Cells," Nat. Commun. **8**, 15 684 (2017).

[73] Y.-H. Heo, J.-E. Kim, H. Weerasinghe, D. Angmo, T. Qin, K. Sears, K. Hwang, Y.-S. Jung, J. Subbiah, D. J. Jones, M. Gao, D.-Y. Kim, and D. Vak, "Printing-Friendly Sequential Deposition via Intra-Additive Approach for Roll-To-Roll Process of Perovskite Solar Cells," Nano Energy **41**, 443–451 (2017).

[74] P. Löper, S.-J. Moon, S. Martín de Nicolas, B. Niesen, M. Ledinsky, S. Nicolay, J. Bailat, J.-H. Yum, S. De Wolf, and C. Ballif, "Organic-Inorganic Halide Perovskite/Crystalline Silicon Four-Terminal Tandem Solar Cells," Phys. Chem. Chem. Phys. **17**, 1619–1629 (2015).

[75] J. Werner, C.-H. Weng, A. Walter, L. Fesquet, J. P. Seif, S. De Wolf, B. Niesen, and C. Ballif, "Efficient Monolithic Perovskite/Silicon Tandem Solar Cell with Cell Area >1 cm^2," J. Phys. Chem. Lett. **7**, 161–166 (2016).

[76] T. Todorov, T. Gershon, O. Gunawan, Y. S. Lee, C. Sturdevant, L.-Y. Chang, and S. Guha, "Monolithic Perovskite-CIGS Tandem Solar Cells via In Situ Band Gap Engineering," Adv. Energy Mater. **5**, 1500 799 (2015).

[77] P. Mantilla-Perez, T. Feurer, J.-P. Correa-Baena, Q. Liu, S. Colodrero, J. Toudert, M. Saliba, S. Buecheler, A. Hagfeldt, A. N. Tiwari, and J. Martorell, "Monolithic CIGS-Perovskite Tandem Cell for Optimal Light Harvesting without Current Matching," ACS Photonics **4**, 861–867 (2017).

[78] S. Tiwari and N. C. Greenham, "Charge Mobility Measurement Techniques in Organic Semiconductors," Opt. Quantum Electron. **41**, 69–89 (2009).

[79] H. Scher and E. W. Montroll, "Anomalous Transit-Time Dispersion in Amorphous Solids," Phys. Rev. B **12**, 2455–2477 (1975).

[80] C. Canali, C. Jacoboni, F. Nava, G. Ottaviani, and A. Alberigi-Quaranta, "Electron Drift Velocity in Silicon," Phys. Rev. B **12**, 2265–2284 (2016).

[81] C. Jacoboni, C. Canali, G. Ottaviani, and A. Alberigi-Quaranta, "A Review of Some Charge Transport Properties of Silicon," Solid State Electronics **20**, 77–89 (1977).

[82] M. Morohashi, N. Sawaki, and I. Akasaki, "Electron Mobility and Drag Effect in p-Type Silicon," Jpn. J. Appl. Phys. **24**, 732–736 (1985).

[83] M. Morohashi, N. Sawaki, and I. Akasaki, "Measurement of Electron Mobility in p-Si by Time-of-Flight technique," Jpn. J. Appl. Phys. **24**, 661–665 (1985).

[84] D. D. Tang, F. F. Fang, M. Scheuermann, and T. C. Chen, "Time-of-Flight Measurements of Minority-Carrier Transport in p-Silicon," Appl. Phys. Lett. **49**, 1540–1541 (1986).

[85] M. Handloser, *Optical Investigation of Charge Carrier Dynamics in Organic Semiconductors and Graphene for Photovoltaic Applications*, Ph.D. thesis, LMU München (2014).

[86] W. Becker, *The bh TCSPC Handbook* (Becker & Hickl GmbH, Berlin, 2008).

[87] M. Kitamura, T. Imada, S. Kako, and Y. Arakawa, "Time-of-Flight Measurement of Lateral Carrier Mobility in Organic Thin Films," Jpn. J. Appl. Phys. **43**, 2326–2329 (2004).

[88] J. Isberg, S. Majdi, M. Gabrysch, I. Friel, and R. S. Balmer, "A Lateral Time-of-Flight System for Charge Transport Studies," Diam. Relat. Mater. **18**, 1163–1166 (2009).

[89] E. Pavlica and G. Bratina, "Time-of-Flight Mobility of Charge Carriers in Position-Dependent Electric Field Between Coplanar Electrodes," Appl. Phys. Lett. **101**, 093 304 (2012).

[90] L. Yu, X. Li, E. Pavlica, F. P. V. Koch, G. Portale, I. da Silva, M. A. Loth, J. E. Anthony, P. Smith, G. Bratina, B. K. C. Kjellander, C. W. M. Bastiaansen, D. J. Broer, G. H. Gelinck, and N. Stingelin, "Influence of Solid-State Microstructure on the Electronic Performance of 5,11-Bis(Triethylsilylethynyl) Anthradithiophene," Chem. Mater. **25**, 1823–1828 (2013).

[91] E. Pavlica, R. B. Penumala, and G. Bratina, "The Role of Local Potential Minima on Charge Transport in Thin Organic Semiconductor Layers," Org. Electron. **42**, 221–227 (2017).

[92] J. M. Ball, M. M. Lee, A. Hey, and H. J. Snaith, "Low-Temperature Processed Meso-Superstructured to Thin-Film Perovskite Solar Cells," Energy Environ. Sci. **6**, 1739–1743 (2013).

[93] I. Grill, K. Handloser, F. C. Hanusch, N. Giesbrecht, T. Bein, P. Docampo, M. Handloser, and A. Hartschuh, "Controlling Crystal Growth by Chloride-Assisted Synthesis: Towards Optimized Charge Transport in Hybrid Halide Perovskites," Sol. Energy Mater. Sol. Cells **166**, 269–275 (2017).

[94] G. Peng, X. Xu, and G. Xu, "Hybrid Organic-Inorganic Perovskites Open a New Era for Low-Cost, High Efficiency Solar Cells," J. Nanomater. **2015**, 241 853 (2015).

[95] T. Miyasaka, "Perovskite Photovoltaics: Rare Functions of Organo Lead Halide in Solar Cells and Optoelectronic Devices," Chem. Lett. **44**, 720–729 (2015).

[96] N.-G. Park, "Perovskite Solar Cells: An Emerging Photovoltaic Technology," Mater. Today **18**, 65–72 (2015).

[97] A. Sadhanala, F. Deschler, T. H. Thomas, S. Dutton, K. C. Goedel, F. C. Hanusch, M. L. Lai, U. Steiner, T. Bein, P. Docampo, D. Cahen, and R. H. Friend, "Preparation of Single-Phase Films of $CH_3NH_3Pb(I_{3-x}Br_x)_3$ with Sharp Optical Band Edges," J. Phys. Chem. Lett. **2014**, 2501–2505 (2014).

[98] T. Saga, "Advances in Crystalline Silicon Solar Cell Technology for Industrial Mass Production," NPG Asia Mater. **2**, 96–102 (2010).

[99] P. Jackson, D. Hariskos, R. Wuerz, O. Kiowski, A. Bauer, T. Magorian Friedlmeier, and M. Powalla, "Properties of Cu(In,Ga)Se_2 Solar Cells with New Record Efficiencies up to 21.7%," Phys. Status Solidi RRL **9**, 28–31 (2015).

[100] Z. Zang, A. Nakamura, and J. Temmyo, "Single Cuprous Oxide Films Synthesized by Radical Oxidation at Low Temperature for PV Application," Opt. Express **21**, 11 448–11 456 (2013).

[101] C. Sun, Y. Guo, H. Duan, Y. Chen, Y. Guo, H. Li, and H. Liu, "Solvent-Assisted Growth of Organic-Inorganic Hybrid Perovskites with Enhanced Photovoltaic Performances," Sol. Energy Mater. Sol. Cells **143**, 360–368 (2015).

[102] L. Huang, Z. Hu, J. Xu, K. Zhang, J. Zhang, and Y. Zhu, "Multi-Step Slow Annealing Perovskite Films for High Performance Planar Perovskite Solar Cells," Sol. Energy Mater. Sol. Cells **141**, 377–382 (2015).

[103] C. Huang, N. Fu, F. Liu, L. Jiang, X. Hao, and H. Huang, "Highly Efficient Perovskite Solar Cells with Precursor Composition-Dependent Morphology," Sol. Energy Mater. Sol. Cells **145**, 231–237 (2016).

[104] A. Rapsomanikis, D. Karageorgopoulos, P. Lianos, and E. Stathatos, "High Performance Perovskite Solar Cells with Functional Highly Porous TiO_2 Thin Films Constructed in Ambient Air," Sol. Energy Mater. Sol. Cells **151**, 36–43 (2016).

[105] J.-H. Im, C.-R. Lee, J.-W. Lee, S.-W. Park, and N.-G. Park, "6.5% Efficient Perovskite Quantum-Dot-Sensitized Solar Cell," Nanoscale **3**, 4088–4093 (2011).

[106] E. L. Unger, A. R. Bowring, C. J. Tassone, V. L. Pool, A. Gold-Parker, R. Cheacharoen, K. H. Stone, E. T. Hoke, M. F. Toney, and M. D. McGehee, "Chloride in Lead Chloride-Derived Organo-Metal Halides for Perovskite-Absorber Solar Cells," Chem. Mater. **26**, 7158–7165 (2014).

[107] M. Stumpp, R. Ruess, J. Horn, J. Tinz, C. Richter, and D. Schlettwein, "*I*-*V* Hysteresis of Methylammonium Lead Halide Perovskite Films on Microstructured Electrode Arrays: Dependence on Preparation Route and Voltage Scale," Phys. Status Solidi A **213**, 38–45 (2016).

[108] T. Leijtens, S. D. Stranks, G. E. Eperon, R. Lindblad, E. M. J. Johansson, I. J. McPherson, H. Rensmo, J. M. Ball, M. M. Lee, and H. J. Snaith, "Electronic Properties of Meso-Superstructured and Planar Organometal Halide Perovskite Films: Charge Trapping, Photodoping, and Carrier Mobility," ACS Nano **8**, 7147–7155 (2014).

[109] T. J. Savenije, C. S. Ponseca Jr., L. Kunneman, M. Abdellah, K. Zheng, Y. Tian, Q. Zhu, S. E. Canton, I. G. Scheblykin, T. Pullerits, A. Yartsev, and V. Sundström, "Thermally Activated Exciton Dissociation and Recombination Control the Carrier Dynamics in Organometal Halide Perovskite," J. Phys. Chem. Lett. **5**, 2189–2194 (2014).

[110] C. Zhao, B. Chen, X. Qiao, L. Luan, K. Lu, and B. Hu, "Perovskite Solar Cells: Revealing Underlying Processes Involved in Light Soaking Effects and Hysteresis Phenomena in Perovskite Solar Cells," Adv. Energy Mater. **5**, 1500 279 (2015).

[111] P. Docampo, J. M. Ball, M. Darwich, G. E. Eperon, and H. J. Snaith, "Efficient Organometal Trihalide Perovskite Planar-Heterojunction Solar Cells on Flexible Polymer Substrates," Nat. Commun. **4**, 2761 (2013).

[112] A. T. Barrows, A. J. Pearson, C. K. Kwak, A. D. F. Dunbar, A. R. Buckley, and D. G. Lidzey, "Efficient Planar Heterojunction Mixed-Halide Perovskite Solar Cells Deposited Via Spray-Deposition," Energy Environ. Sci. **7**, 2944–2950 (2014).

[113] A. Mei, X. Li, L. Liu, Z. Ku, T. Liu, Y. Rong, M. Xu, M. Hu, J. Chen, Y. Yang, M. Grätzel, and H. Han, "A Hole-Conductor-Free, Fully Printable Mesoscopic Perovskite Solar Cell with High Stability," Science **345**, 295–298 (2014).

[114] K. Handloser, N. Giesbrecht, T. Bein, P. Docampo, M. Handloser, and A. Hartschuh, "Contactless Visualization of Fast Charge Carrier Diffusion in Hybrid Halide Perovskite Thin Films," ACS Photonics **3**, 255–261 (2016).

[115] E. Huitema and J. P. van der Erden, "Defect Formation During Crystal Growth," J. Cryst. Growth **166**, 141–145 (1995).

[116] A. Binek, I. Grill, N. Huber, K. Peters, A. G. Hufnagel, M. Handloser, P. Docampo, A. Hartschuh, and T. Bein, "Control of Perovskite Crystal Growth by Methylammonium Lead Chloride Templating," Chem. Asian. J. **11**, 1199–1204 (2016).

[117] C. G. Wu, C.-H. Chiang, Z.-L. Tseng, M. K. Nazeeruddin, A. Hagfeldt, and M. Grätzel, "High Efficiency Stable Inverted Perovskite Solar Cells without Current Hysteresis," Energy Environ. Sci. **8**, 2725–2733 (2015).

[118] K. Liang, D. B. Mitzi, and M. T. Prikas, "Synthesis and Characterization of Organic-Inorganic Perovskite Thin Films Prepared Using a Versatile Two-Step Dipping Technique," Chem. Mater. **10**, 403–411 (1998).

[119] J. Schlipf, P. Docampo, C. J. Schaffer, V. Körstgens, L. Bießmann, F. C. Hanusch, N. Giesbrecht, S. Bernstorff, T. Bein, and P. Müller-Buschbaum, "A Closer Look into Two-Step Perovskite Conversion with X-ray Scattering," J. Phys. Chem. Lett. **6**, 1265–1269 (2015).

[120] W. Tian, C. Zhao, J. Leng, R. Cui, and S. Jin, "Visualizing Carrier Diffusion in Individual Single-Crystal Organolead Halide Perovskite Nanowires and Nanoplates," J. Am. Chem. Soc. **137**, 12 458–12 461 (2015).

[121] X. Ziang, L. Shifeng, Q. Laixiang, P. Shuping, W. Wei, Y. Yu, Y. Li, C. Zhijian, W. Shufeng, D. Honglin, Y. Minghui, and G. G. Qin, "Refractive Index and Extinction Coefficient of $CH_3NH_3PbI_3$ Studied by Spectroscopic Ellipsometry," Opt. Mater. Express **5**, 29–43 (2014).

[122] P. Löper, M. Stuckelberger, B. Niesen, J. Werner, M. Filipič, S.-J. Moon, J.-H. Yum, M. Topič, S. De Wolf, and C. Ballif, "Complex Refractive Index Spevtra of $CH_3NH_3PbI_3$ Perovskite Thin Films Determined by Spectroscopic Ellipsometry and Spetrophotometry," J. Phys. Chem. Lett. **6**, 66–71 (2015).

[123] M. S. Alias, I. Dursun, M. I. Saidaminov, E. M. Diallo, P. Mishra, T. K. . Ng, O. M. Bakr, and B. S. Ooi, "Optical Constants of $CH_3NH_3PbI_3$ Perovskite Thin Films Measured by Spectroscopic Ellipsometry," Opt. Express **24**, 16 586–16 594 (2016).

[124] L. J. Philips, A. M. Rashed, R. E. Treharne, J. Kay, P. Yates, I. Z. Mitrovic, A. Weerakkody, S. Hall, and K. Durose, "Maximizing the Optical Performance of Planar $CH_3NH_3PbI_3$ Hybrid Perovskite Heterojunction Stacks," Sol. Energy Mater. Sol. Cells **147**, 327–333 (2016).

[125] M. Brinza and G. J. Adriaenssens, "The Time-of-Flight Photocurrent Analysis Revisited," J. Optoelectron. Adv. Mater. **8**, 2028–2034 (2006).

[126] K. Tajima, Y. Suzuki, and K. Hashimoto, "Polymer Photovoltaic Devices Using Fully Regioregular Poly[(2-methoxy-5-(3',7'-dimethyloctyloxy))-1,4-phenylenevinylene]," J. Phys. Chem. C **112**, 8507–8510 (2008).

[127] A. M. Ballantyne, L. Chen, J. Dane, T. Hammant, F. M. Braun, M. Heeney, W. Duffy, I. McCulloch, D. D. C. Bradley, and J. Nelson, "The Effect of Poly(3-hexylthiophene) Molecular Weight on Charge Transport and the Performance of Polymer:Fullerene Solar Cells," Adv. Funct. Mater. **18**, 2373–2380 (2008).

[128] D. Gupta, M. Bag, and K. S. Narayan, "Correlating Reduced Fill Factor in Polymer Solar Cells to Contact Effects," Appl. Phys. Lett. **92**, 093 301 (2008).

[129] M. Schubert, C. Yin, M. Castellani, S. Bange, T. L. Tam, A. Sellinger, H.-H. Hörhold, T. Kietzke, and D. Neher, "Heterojunction Topology Versus Fill Factor Correlations in Novel Hybrid Small-Molecular/Polymeric Solar Cells," J. Chem. Phys. **130**, 094 703 (2009).

[130] L. M. Andersson, C. Müller, B. H. Badada, F. Zhang, U. Würfel, and O. Inganäs, "Mobility and Fill Factor Correlation in Geminate Recombination Limited Solar Cells," J. Appl. Phys. **110**, 024 509 (2011).

[131] L. Herz, "Charge-Carrier Mobilities in Metal Halide Perovskites: Fundamental Mechanisms and Limits," ACS Energy Lett. **2**, 1539–1548 (2017).

[132] G. Giorgi and K. Yamashita, "Organic-Inorganic Halide Perovskites: An Ambipolar Class of Materials with Enhanced Photovoltaic Performances," J. Mater. Chem. A **3**, 8981–8991 (2015).

[133] K. Miyano, N. Tripathi, M. Yanagida, and Y. Shirai, "Lead Halide Perovskite Photovoltaic as a Model p-i-n Diode," Acc. Chem. Res. **49**, 303–310 (2016).

[134] M. Sheik-Bahae and R. I. Epstein, "Can Laser Light Cool Semiconductors?" Phys. Rev. Lett. **92**, 247 403 (2004).

[135] G. A. Acket, W. Nijman, and H. 't Lam, "Electron Lifetime and Diffusion Constant in Germanium-Doped Gallium Arsenide," J. Appl. Phys. **45**, 3033–3040 (1974).

[136] M. I. Saidaminov, A. L. Abdelhady, B. Murali, E. Alarousu, V. M. Burlakov, W. Peng, I. Dursun, L. Wang, Y. He, G. Maculan, A. Goriely, T. Wu, O. F. Mohammed, and O. M. Bakr, "High-Quality Bulk Hybrid Perovskite Single Crystals within Minutes by Inverse Temperature Crystallization," Nat. Commun. **6**, 7586 (2015).

[137] Q. Dong, Y. Fang, Y. Shao, P. Mulligan, J. Qiu, L. Cao, and J. Huang, "Electron-hole Diffusion Lengths >175 μm in Solution-Grown $CH_3NH_3PbI_3$ Single Crystals," Science **347**, 967–970 (2015).

[138] O. E. Semonin, G. A. Elbaz, T. D. Straus, D. B. Hull, A. M. Paley, D. W. van der Zande, J. C. Hone, I. Kymissis, C. R. Kagan, X. Roy, and J. S. Owen, "Limits of Carrier Diffusion in n-Type and p-Type $CH_3NH_3PbI_3$ Perovskite Single Crystals," J. Phys. Chem. Lett. **7**, 3510–3518 (2016).

[139] N. Giesbrecht, J. Schlipf, L. Oesinghaus, A. Binek, T. Bein, P. Müller-Buschbaum, and P. Docampo, "Synthesis of Perfectly Oriented and Micrometer-Sized $MAPbBr_3$ Perovskite Crystals for Thin-Film Photovoltaic Applications," ACS Energy Lett. **1**, 150–154 (2016).

[140] N. Giesbrecht, J. Schlipf, I. Grill, P. Rieder, V. Dyakonov, T. Bein, A. Hartschuh, P. Müller-Buschbaum, and P. Docampo, "Single-Crystal-Like Optoelectronic Properties of $MAPbI_3$ Perovskite Polycrystalline Films," J. Mater. Chem. A **6**, 4822–4828 (2018).

[141] M. I. Nathan, W. P. Dumke, K. Wrenner, S. Tiwari, S. L. Wright, and K. A. Jenkins, "Electron Mobility in p-Type GaAs," Appl. Phys. Lett. **52**, 654–656 (1988).

[142] A. D. Wright, C. Verdi, R. L. Milot, G. E. Eperon, M. A. Pérez-Osorio, H. J. Snaith, F. Giustino, M. B. Johnston, and L. M. Herz, "Electron-Phonon Coupling in Hybrid Lead Halide Perovskites," Nat. Commun. **7**, 11 755 (2016).

[143] J. M. Frost, "Calculating Polaron Mobility in Halide Perovskites," Phys. Rev. B **96**, 195 202 (2017).

[144] T. M. Brenner, D. A. Egger, L. Kronik, G. Hodes, and D. Cahen, "Hybrid Organic-Inorganic Perovskites: Low-Cost Semiconductors with Intriguing Charge-Transport Properties," Nat. Rev. Mater. **1**, 15 007 (2016).

[145] M. Sendner, P. K. Nayak, S. Egger, D. A. Beck, C. Müller, B. Epding, W. Kowalsky, L. Kronik, H. J. Snaith, A. Pucci, and R. Lovrinčić, "Optical Phonons in Methylammonium Lead Halide Perovskites and Implications for Charge Transport," Mater. Horiz. **3**, 613–620 (2016).

[146] T. M. Brenner, D. A. Egger, A. M. Rappe, L. Kronik, G. Hodes, and D. Cahen, "Are Mobilities in Hybrid Organic-Inorganic Halide Perovskites Actually "High"?" J. Phys. Chem. Lett. **6**, 4754–4757 (2015).

[147] J. M. Frost and A. Walsh, "What is Moving in Hybrid Halide Perovskite Solar Cells?" Acc. Chem. Res. **49**, 528–535 (2016).

[148] H. J. Snaith, "Perovskites: The Emergence of a New Era for Low-Cost, High-Efficiency Solar Cells," J. Phys. Chem. Lett. **4**, 3623–3630 (2013).

[149] S. Kazim, M. K. Nazeeruddin, M. Grätzel, and S. Ahmad, "Perovskite as Light Harvester: A Game Changer in Photovoltaics," Angew. Chem. Int. Ed. **53**, 2812–2824 (2014).

[150] Z. Xiao, C. Bi, Y. Shao, Q. Dong, Q. Wang, Y. Yuan, C. Wang, Y. Gao, and J. Huang, "Efficient, High Yield Perovskite Photovoltaic Devices Grown by Interdiffusion of Solution-Processed Precursor Stacking Layers," Energy Environ. Sci. **7**, 2619–2623 (2014).

[151] W. Nie, G. Gupta, B. K. Crone, F. Liu, D. L. Smith, P. P. Ruden, C.-Y. Kuo, H. Tsai, H.-L. Wang, H. Li, S. Tretiak, and A. D. Mohite, "Interface Design Principles for High-Performance Organic Semiconductor Devices," Adv. Sci. **2**, 1500 024 (2015).

[152] G. E. Eperon, V. M. Burlakov, P. Docampo, A. Goriely, and H. J. Snaith, "Morphological Control for High Performance, Solution-Processed Planar Heterojunction Perovskite Solar Cells," Adv. Funct. Mater. **24**, 151–157 (2014).

[153] F. X. Xie, D. Zhang, H. Su, X. Ren, K. S. Wong, M. Grätzel, and W. C. H. Choy, "Vacuum-Assisted Thermal Annealing of $CH_3NH_3PbI_3$ for Highly Stable and Efficient Perovskite Solar Cells," ACS Nano **9**, 639–646 (2015).

[154] H. Zhou, Q. Chen, G. Li, S. Luo, T.-b. Song, H.-S. Duan, Z. Hong, J. You, Y. Liu, and Y. Yang, "Interface Engineering of Highly Efficient Perovskite Solar Cells," Science **345**, 542–546 (2014).

[155] M. Saliba, K. W. Tan, H. Sai, D. T. Moore, T. Scott, W. Zhang, L. A. Estroff, U. Wiesner, and H. J. Snaith, "Influence of Thermal Processing Protocol upon the Crystallization and Photovoltaic Performance of Organic-Inorganic Lead Trihalide Perovskites," J. Phys. Chem. C **118**, 17 171–17 177 (2014).

[156] K. W. Tan, D. T. Moore, M. Saliba, H. Sai, L. A. Estroff, T. Hanrath, H. J. Snaith, and U. Wiesner, "Thermally Induced Structural Evolution and Performance of Mesoporous Block Copolymer-Directed Alumina Perovskite Solar Cells," ACS Nano **8**, 4730–4739 (2014).

[157] W. Nie, H. Tsai, R. Asadpour, J.-C. Blancon, A. J. Neukirch, G. Gupta, J. J. Crochet, M. Chhowalla, S. Tretiak, M. A. Alam, H.-L. Wang, and A. D. Mohite, "High-efficiency solution-processed perovskite solar cells with millimeter-scale grains," Science **347**, 522–525 (2015).

[158] X. Wu, M. T. Trinh, D. Niesner, H. Zhu, Z. Norman, J. S. Owen, O. Yaffe, B. J. Kudisch, and X. Zhu, "Trap States in Lead Iodide Perovskites," J. Am. Chem. Soc. **137**, 2089–2096 (2015).

[159] F. K. Aldibaja, L. Badia, E. Mas-Marza, R. S. Sanchez, E. M. Barea, and I. Mora-Sero, "Effect of Different Lead Precursors on Perovskite Solar Cell Performance and Stability," J. Mater. Chem. A **3**, 9194–9200 (2015).

[160] Y. Li, W. Sun, W. Yan, S. Ye, H. Peng, Z. Liu, Z. Bian, and C. Huang, "High-Performance Planar Solar Cells Based on $CH_3NH_3PbI_{3-x}Cl_x$ Perovskites with Determined Chlorine Mole Fraction," Adv. Funct. Mater. **25**, 4867–4873 (2015).

[161] V. L. Pool, A. Gold-Parker, M. D. McGehee, and M. F. Toney, "Chlorine in $PbCl_2$-Derived Hybrid-Perovskite Solar Absorbers," Chem. Mater. **27**, 7240–7243 (2015).

[162] A. E. Williams, P. J. Holliman, M. J. Carnie, M. L. Davies, D. A. Worsley, and T. M. Watson, "Perovskite processing for photovoltaics: a spectro-thermal evaluation," J. Mater. Chem. A. **2**, 19 338–19 346 (2014).

[163] J. S. Manser, B. Reis, and P. V. Kamat, "Evolution of Organic-Inorganic Lead Halide Perovskite from Solid-State Iodoplumbate Complexes," J. Phys. Chem. C **119**, 17 065–17 073 (2015).

[164] H. P. Wirges, "Crystallization Technology Handbook. A. MERSMANN (HRSG.) MARCEL DEKKER Inc., New York, 1995. 691 S., zahlr. Abb. und Tab., geb." Chem. Ing. Tech. **67**, 1513–1514 (1995).

[165] W. Ostwald, "Studien über die Bildung und Umwandlung fester Körper. 1. Abhandlung: Übersättigung und Überkaltung," Z. Phys. Chem. **22**, 289–330 (1897).

[166] L. Chi, I. Swainson, L. Cranswick, J.-H. Her, P. Stephens, and O. Knop, "The Ordered Phase of Methylammonium Lead Chloride $CH_3ND_3PbCl_3$," J. Solid State Chem. **178**, 1376–1385 (2005).

[167] C. C. Stoumpos, C. D. Malliakas, and M. G. Kanatzidis, "Semiconducting Tin and Lead Iodide Perovskites with Organic Cations: Phase Transitions, High Mobilities, and Near-Infrared Photoluminescent Properties," Inorg. Chem. **52**, 9019–9038 (2013).

[168] D. Liu and T. L. Kelly, "Perovskite Solar Cells with a Planar Heterojunction Structure Prepared Using Room-Temperature Solution Processing Techniques," Nat. Photonics **8**, 133–138 (2014).

[169] Y. Chen, J. Peng, D. Su, X. Chen, and Z. Liang, "Efficient and Balanced Charge Transport Revealed in Planar Perovskite Solar Cells," ACS App. Mater. Interfaces **7**, 4471–4475 (2015).

[170] I. Grill, M. F. Aygüler, T. Bein, P. Docampo, N. F. Hartmann, M. Handloser, and A. Hartschuh, "Charge Transport Limitations in Perovskite Solar Cells: The Effect of Charge Extraction Layers," ACS Appl. Mater. Interfaces **9**, 37 655–37 661 (2017).

[171] S. S. Mali and C. K. Hong, "p-i-n/n-i-p Type Planar Hybrid Structure of Highly Efficient Perovskite Solar Cells Towards Improved Air Stability: Synthetic Strategies and the Role of p-Type Hole Transport Layer (HTL) and n-Type Electron Transport Layer (ETL) Metal Oxides," Nanoscale **8**, 10 528–10 540 (2016).

[172] R. S. Sanchez and E. Mas-Marza, "Light-Induced Effects on Spiro-OMeTAD Films and Hybrid Lead Halide Perovskite Solar Cells," Sol. Energy Mater. Sol. Cells **158**, 189–194 (2015).

[173] S. Cacovich, G. Divitini, C. Ireland, F. Matteocci, A. Di Carlo, and C. Ducati, "Elemental Mapping of Perovskite Solar Cells by Using Multivariate Analysis: An Insight into Degradation Processes," ChemSusChem **9**, 2673–2678 (2016).

[174] H.-S. Kim and N.-G. Park, "Parameters Affecting *I-V* Hysteresis of $CH_3NH_3PbI_3$ Perovskite Solar Cells: Effects of Perovskite Crystal Size and Mesoporous TiO_2 Layer," J. Phys. Chem. Lett. **5**, 2927–2934 (2014).

[175] A. K. Jena, H.-W. Chen, A. Kogo, Y. Sanehira, M. Ikegami, and T. Miyasaka, "The Interface between FTO and the TiO_2 Compact Layer Can Be One of the Origins to Hysteresis in Planar Heterojunction Perovskite Solar Cells," ACS Appl. Mater. Interfaces **7**, 9817–9823 (2015).

[176] W. Fuhs, M. Milleville, and J. Stuke, "Drift Mobility and Photoconductivity in Amorphous Silicon," Phys. Stat. Sol. (b) **89**, 495–502 (1978).

[177] J. Peng, Y. Sun, Y. Chen, Y. Yao, and Z. Liang, "Light and Thermally Induced Evolutional Charge Transport in $CH_3NH_3PbI_3$ Perovskite Solar Cells," ACS Energy Lett. **1**, 1000–1006 (2016).

[178] D. Liu, M. K. Gangishetty, and T. L. Kelly, "Effect of $CH_3NH_3PbI_3$ Thickness on Device Efficiency in Planar Heterojunction Perovskite Solar Cells," J. Mater. Chem. A. **2**, 19 873–19 881 (2014).

[179] K. Wang, C. Liu, P. Du, L. Chen, J. Zhu, A. Karim, and X. Gong, "Efficiencies of Perovskite Hybrid Solar Cells Influenced by Film Thickness and Morphology of $CH_3NH_3PbI_{3-x}Cl_x$ Layer," Org. Electron. **21**, 19–26 (2015).

[180] W. Marinova, N.and Tress, R. Humphry-Baker, M. I. Dar, V. Bojinov, S. M. Zakeeruddin, M. K. Nazeeruddin, and M. Grätzel, "Light Harvesting and Charge Recombination in $CH_3NH_3PbI_3$ Perovskite Solar Cells Studied by Hole Transport Layer Thickness Variation," ACS Nano **9**, 4200–4209 (2015).

[181] A. Abate, T. Leijtens, S. Pathak, J. Teuscher, R. Avolio, M. E. Errico, J. Kirkpatrik, J. M. Ball, P. Docampo, I. McPherson, and H. J. Snaith, "Lithium Salts as "Redox Active" p-Type Dopants for Organic Semiconductors and their Impact in Solid-State Dye-Sensitized Solar Cells," Phys. Chem. Chem. Phys. **15**, 2572–2579 (2013).

[182] B. Maynard, Q. Long, E. A. Schiff, M. Yang, K. Zhu, R. Kottokkaran, H. Abbas, and V. L. Dalal, "Electron and Hole Drift Mobility Measurements on Methylammonium Lead Iodide Perovskite Solar Cells," Appl. Phys. Lett. **108**, 173 505 (2016).

[183] H. J. Snaith and M. Grätzel, "Enhanced Charge Mobility in a Molecular Hole Transporter via Addition of Redox Inactive Ionic Dopant: Implication to Dye-Sensitized Solar Cells," Appl. Phys. Lett. **89**, 262 114 (2006).

[184] M. L. Petrus, T. Bein, T. J. Dingemans, and P. Docampo, "A Low Cost Azomethine-Based Hole Transporting Material for Perovskite Photovoltaics," J. Mater. Chem. A **3**, 12 159–12 162 (2015).

[185] A. Agresti, S. Pescetelli, B. Taheri, A. E. Del Rio Castillo, L. Cinà, F. Bonaccorso, and A. Di Carlo, "Graphene-Perovskite Solar Cells Exceed 18% Efficiency: A Stability Study," ChemSusChem **9**, 2609–2619 (2016).

[186] G. Murugadoss, H. Kanda, S. Tanaka, H. Nishino, S. Ito, H. Imahori, and T. Umeyama, "An Efficient Electron Transport Material of Tin Oxide for Planar Structure Perovskite Solar Cells," J. Power Sources **307**, 891–897 (2016).

List of Abbreviations

APD	avalanche photodiode
CB	chlorobenzene
CELIV	charge extraction at linearly increasing voltage
CIGS	Copper indium gallium selenide
DC	direct current
DMF	*N*,*N*-Dimethylformamide
DMSO	Dimethyl sulfoxide
EDX	energy dispersive x-ray spectroscopy
EELS	electron energy loss spectroscopy
EQE	external quantum efficiency
ETL	electron transport layer
FDC	fast crystallization deposition
FET	field-effect transistor
FIB	focused ion beam
FTO	Fluorine-doped tin oxide
GBL	γ-Butyrolactone
HTL	hole transport layer
IPA	Propan-2-ol, Isopropyl alcohol
IRF	instrument response function
ITO	Indium tin oxide
MAI	Methylammonium iodide
MAPI	Methylammonium lead triiodide ($CH_3NH_3PbI_3$)
Nd:YAG	Neodymium-doped yttrium aluminum garnet (Nd:$Y_3Al_5O_{12}$)
OPO	optical parametric oscillator
PCBM	Phenyl-C61-butyric acid methyl ester
PCE	power conversion efficiency
PEDOT:PSS	Poly(3,4-ethylenedioxythiophene) polystyrene sulfonate
PL	photoluminescence
PMMA	Poly(methyl methacrylate)
PV	photovoltaic
RT	room temperature
SCLC	space-charge limited current
SDC	solution deposition conversion
SEM	scanning electron microscopy
TCO	transparent conducting oxide

TCSPC ..... time-correlated single photon counting
THTO ..... Tetrahydrothiophene 1-oxide
ToF ..... time-of-flight
TRMC ..... time-resolved microwave conductivity
XRD ..... X-ray diffration

List of Figures

2.1 Illustration of processes at a p-n junction without applying a voltage. . . . 6
2.2 Current-voltage characterization of solar cell devices. 8
2.3 Recombination mechanisms of photoinduced charge carriers. 9
2.4 Schematic energy diagram of a heterojunction solar cell. 11
2.5 Illustration of different device architectures from three solar cell generations. 13
2.6 Perovskite crystal structure and perovskite-based solar cell architectures. . . 15

3.1 Schematic of the time-of-flight setup used for mobility experiments. 20
3.2 Detailed representation of the circuit for ToF experiments. 21
3.3 Transients recorded for a p-doped (100) silicon wafer. 22
3.4 Schematic of the microscope and signal detection path used for PL experiments. 23
3.5 Layout of the optical beam path and electronics employed for TCSPC measurements. 24
3.6 Images of the lateral contact pattern and analysis of the gap sizes. 25

4.1 Characterization of perovskite thin films fabricated via a two-step synthesis protocol. 32
4.2 Photovoltaic performance of planar solar cells derived from a two-step fabrication procedure. 33
4.3 Time-of-flight transients for pure and chloride-treated MAPI thin films. . . 34
4.4 Optical response in the perovskite films investigated via PL microscopy. . . 36
4.5 In-situ photoluminescence studies of perovskite film formation at room temperature. 37

5.1 Schematic representation of the fabrication protocols used for the synthesis of the two investigated films. 42
5.2 Spatio-temporal investigation of transport in FDC and SDC MAPI via PL microscopy. 43
5.3 ToF measurements of laterally contacted FDC and SDC MAPI thin films with varying distances between the metal electrodes. 44
5.4 SEM cross section and efficiency statistics for working photovoltaic devices incorporating FDC and SDC MAPI thin films. 46

6.1 Characterization of the millimeter-sized MAPI crystal via time-of-flight. . . 51
6.2 SEM top views of MAPI thin films with different crystal sizes. 53

7.1 Scanning electron micrographs of cross-sections of MAPI-based solar cells with different evaporation times during perovskite synthesis. 57
7.2 XRD analysis of $PbCl_2$-derived MAPI films at different temperatures and evaporation times. 58
7.3 Schematic mechanism of the crystallization of the MAPI perovskite based on the $PbCl_2$ synthesis route in accordance with the Ostwald-Volmer rule. . 59
7.4 Comparison of SEM cross sections and schematic illustration of MAPI films derived from a one-step and a sequential deposition procedure. 60

8.1 Schematic illustration of the employed sample layout and the experimental setup. 67
8.2 Extraction of the charge carrier mobility in the perovskite layer from photocurrent experiments in lateral configuration. 68
8.3 Characterization of the MAPI-based photovoltaic devices. 69
8.4 Photocurrent transients obtained for complete perovskite-based solar cell devices using the described experimental setup. 71
8.5 ToF results for two extreme cases of solar cell devices. 73

List of Tables

3.1 Analysis of the electrode spacings. 26

6.1 Comparison of mobility values for MAPI films comprising differently sized grains with millimeter-sized MAPI crystal. 52

8.1 Preparation parameters for different TiO_x thicknesses in perovskite-based solar cells. 65

8.2 Preparation parameters for different spiro-OMeTAD thicknesses in perovskite-based solar cells. 66

List of peer-reviewed publications

Nadja Giesbrecht, Johannes Schlipf, Irene Grill, Philipp Rieder, Vladimir Dyakonov, Thomas Bein, Achim Hartschuh, Peter Müller-Buschbaum, and Pablo Docampo,
"Single-Crystal-Like Optoelectronic Properties of $MAPbI_3$ Perovskite Polycrystalline Films",
J. Mater. Chem. A **6**, 4822–4828 (2018).

Yinghong Hu, Eline M. Hutter, Philipp Rieder, Irene Grill, Jonas Hanisch, Meltem F. Aygüler, Alexander G. Hufnagel, Matthias Handloser, Thomas Bein, Achim Hartschuh, Kristofer Tvingstedt, Vladimir Dyakonov, Andreas Baumann, Tom J. Savenije, Michiel L. Petrus, and Pablo Docampo,
"Understanding the Role of Cesium and Rubidium Additives in Perovskite Solar Cells: Trap States, Charge Transport and Recombination", *Adv. Energy Mater.*, 1703057 (2018).

Irene Grill, Meltem F. Aygüler, Thomas Bein, Pablo Docampo, Nicolai F. Hartmann, Matthias Handloser, and Achim Hartschuh,
"Charge Transport Limitaions in Perovskite Solar Cells: The Effect of Charge Extraction Layers", *ACS Appl. Mater. Interfaces* **9**, 37655–37661 (2017).

Irene Grill, Kathrin Handloser, Fabian C. Hanusch, Nadja Giesbrecht, Thomas Bein, Pablo Docampo, Matthias Handloser, and Achim Hartschuh,
"Controlling Crystal Growth by Chloride-Assisted Synthesis: Towards Optimized Charge Transport in Hybrid Halide Perovskites", *Sol. Energ. Mat. Sol. Cells* **166**, 269–275 (2017).

Andreas Binek, Irene Grill, Niklas Huber, Kristina Peters, Alexander G. Hufnagel, Matthias Handloser, Pablo Docampo, Achim Hartschuh, and Thomas Bein,
"Control of Perovskite Crystal Growth by Methylammonium Lead Chloride Templating", *Chem. Asian J.* **11**, 1199–1204 (2016).

Mona Calik, Florian Auras, Laura M. Salonen, Kathrin Bader, Irene Grill, Matthias Handloser, Dana D. Medina, Mirjam Dogru, Florian Löbermann, Dirk Trauner, Achim Hartschuh, and Thomas Bein,
"Extraction of Photogenerated Electrons and Holes from a Covalent Organic Framework Integrated Heterojunction", *J. Am .Chem. Soc.* **136**, 17802–17807 (2014).

Conference contributions

Materials Research Society (MRS) Fall Meeting 2017
Boston (United States of America), November 26-December 1, 2017
Poster presentation: *"Charge transport properties and their limiting factors in hybrid perovskite photovoltaic devices studied via Time-of-Flight experiments"*

6th International SolTech Conference 2017
Munich (Germany), October 4-5, 2017
Poster presentation: *"The impact of crystal size and material composition on charge transport in hybrid perovskite thin films and transport limitations in solar cells"*

33rd European Photovoltaic Solar Energy Conference (EUPVSEC) 2017
Amsterdam (The Netherlands), September 25-29, 2017
Oral presentation: *"Determination of Charge Transport Properties and Their Limiting Factors in Hybrid Perovskite Photovoltaic Devices via Time-Resolved Photocurrent Studies"*

DPG Spring Meeting 2017 of the Condensed Matter Section
Dresden (Germany), March 19-24, 2017
Oral presentation: *"Identification of charge transport limiting factors in novel perovskite solar cells by Time-of-flight measurements"*

2nd International Conference on Perovskite Solar Cells and Optoelectronics (PSCO) 2016
Genova (Italy), September 26-28, 2016
Poster presentation: *"Identification of charge transport limiting factors in novel perovskite solar cells by Time-of-Flight measurements"*

European Materials Research Society (E-MRS) Fall Meeting 2016
Warsaw (Poland), September 19-22, 2016
Oral presentation: *"Identification of charge transport limiting factors in novel perovskite solar cells by Time-of-Flight measurements"*

Photovoltaic Technical Conference (PVTC) 2016
Marseille (France), May 9-11, 2016
Oral presentation: *"Correlating charge carrier mobility, morphology and efficiency in hy-*

brid halide perovskite photovoltaic devices"

5th International SolTech Conference 2016
Munich (Germany), April 5-8, 2016
Poster presentation: *"Optoelectronic studies on hybrid perovskites: Linking mobility to efficiency and morphology"*

DPG Spring Meeting 2016 of the Condensed Matter Section
Regensburg (Germany), March 6-11, 2016
Oral presentation: *"Correlating charge carrier mobility, morphology and efficiency in hybrid halide perovskite photovoltaic devices"*

1st International Conference on Perovskite Solar Cells and Optoelectronics (PSCO) 2015
Lausanne (Switzerland), September 27-29, 2015
Oral presentation: *"Extraction of charge carrier mobility by energy dependent time-of-flight studies in mixed halide perovskite thin films"*

CeNS Workshop "Channels and Bridges to the Nanoworld" 2015
Venice (Italy), September 21-25, 2015
Poster presentation: *"Determination of charge carrier mobility by energy dependent time-of-flight studies in mixed halide perovskite thin films"*

Acknowledgments

Thinking back about the past years as a PhD student in Physical Chemistry, I must say that I enjoyed this time a lot and I don't want to miss it because it shaped me from a scientific as well as from a personal point of view. I had the great opportunity to meet and work with many people who contributed significantly to this thesis and made it to an amazing experience in my life. Now it's time to say THANK YOU to everyone who guided me:

First of all, I would like to thank **Prof. Achim Hartschuh** for giving me the chance to be a member of the Nanooptics Group and to learn all the tiny details needed for the opto-electronic characterization of thin film materials. He was always willing to support my work in terms of discussing about experimental results, understanding fundamental physics and helping to find solutions to problems related to the experimental setup. He guided me through each single step of the work while leaving me the freedom to decide in which direction to go with my research. At this point I also want to thank him for making the participation in numerous conferences possible where I could present experimental results and discuss them with a broader audience (while traveling to some really beautiful places...).

I also want to thank **Dr. Pablo Docampo** for many scientific discussions and highly beneficial suggestions regarding the in-house collaboration on organolead halide perovskites. Thank you for opening many many doors to new ideas and scientific approaches. And thank you for being the second reviewer of this thesis.

Special thanks to **Dr. Matthias Handloser** who accompanied me right from the start of this work when introducing and setting up a new measurement technique in the research group. Furthermore, I want to express my deep gratitude for all scientific as well as non-scientific discussions (the most important ones!), for his remarkable willingness to help in any situation and for teaching me "how science works".

Thanks to **Prof. Thomas Bein** for the nice and very fruitful collaboration and for all your useful feedback.

Many thanks to all former and current group members for the great working atmosphere: **Dr. Nicolai Hartmann, Dr. Julia Janik, Kathrin Handloser, Dr. Nina Mauser, Veit Giegold, Alexander Biewald, Nicolas Coca Lopez, Dr. Xian Shi, Dr. Har-**

ald Budde, Dr. Richard Ciesielski and **Dr. Alberto Comin**. It was a pleasure to share Christmas parties, hiking trips, dinners and numerous other (mainly food-related...) events with you.

Furthermore, big thanks to my collaborators **Nadja Giesbrecht, Meltem Aygüler, Yinghong Hu, Dr. Andreas Binek** and **Dr. Michiel Petrus** for the steady and exceptionally quick supply of great sample material. And for always making me feel so welcome in your offices!

Moreover, I want to thank my F-student **Niklas Huber** who did a great job during his time in the group.

Thanks to **Rita Römling** for her help in many administrative issues.

Philipp Altpeter from the Department of Physics (LMU) I want to thank for his support concerning sample preparation under cleanroom conditions.

Last but not least, I want to express my deepest gratitude to **my parents** for their unconditional and never ending support which encouraged me to follow my own path. Thank you so much for believing in me and giving me the strength to master even the toughest situations. I would have never got this far without you!